UNIVERSITY OF OXFORD

Quantum Dot Lasers

by

Robin Patel

Corpus Christi College

A thesis submitted for the
degree of Doctor of Philosophy

Department of Materials

February 2017

Abstract

Here we present direct investigation of the lasing behaviour by performing gain spectroscopy of solution-based CQDs enabled via in-situ tuning of the feedback wavelength of an open-access hemispherical microcavity. The investigation is performed on two different types of CQDs, namely spherical CdSe/CdS core-shell CQDs and nanopletelets (NPs). The lasing threshold and the differential gain/slope efficiency of the fundamental cavity mode are measured as a function of their spectral position over a spectral range of $\sim$ 32 nm and of $\sim$ 42 nm for the spherical CQDs and NPs, respectively. The results of the gain spectroscopy are described using theoretical models, providing insights into the mechanism governing the observed lasing behaviour. Furthermore, the open-access cavity architecture provides a very convenient way of producing in-situ tunable lasing, and single-mode lasing of the fundamental cavity mode over a spectral range of $\sim$ 25 nm and $\sim$ 37 nm is demonstrated using spherical CQDs and NPs, respectively. In addition, the stability of laser emission is investigated, with the lasing intensity of the fundamental cavity mode remaining constant over a time period of almost 6 mins. It is hoped that the results will provide a detailed understanding of the lasing behaviour of CQDs. This information can be fed back into the design of CQDs in which the lasing threshold can be reduced to the point where useful devices can be constructed, and in the design of resonant optical feedback structures for which the appropriate wavelength must be carefully selected.

Acknowledgements

This thesis was only made possible through the support of various people both within the Photonic Nanomaterials Group and outside. I would like to thank all the group members for their supports and over the course of my PhD. Special thanks is given to Aurelien Trichet who has was involved extensively in my initial training in the lab, and also David Coles for his support and guidance at key stages of my PhD. I would also like to thank Simon Fairclough for his assistance on the sample preparation work and Prof Edman Tsang for providing access to his lab for this purpose, which was crucial step in making this project as success. Furthermore, a very big thanks must be given to our collaborators at the Samsung Advanced Institute of Technology, in particular Dr Eunjoo Jang and Dr Hyosook Jang, and also to our collaborators at the Istituto Italiano di Tecnologia (IIT), Dr Iwan Moreels and Sotiris Christodoulou, for providing very high quality quantum dots, without which the project would not have been possible. Dr David Binks and Dr Marina Leontiadou, our collaborators at the University of Manchester, are also gratefully acknowledged for their work on the characterisation of the quantum dots using pump-probe spectroscopy.

I would like to give a very special thanks to my supervisor Prof. Jason smith, who has been a fantastic mentor and has provided with me excellent scientific guidance and encouragement through my time at Oxford. In addition, I would also like to give special thanks to Prof. Robert Taylor in the Department of Physics for very generously accommodating me in this lab, where the majority of my experiments were conducted.

Finally, I would like to acknowledge my parents, Kirit and Rekha for their inspiration, love and support for which I will always be grateful.

Contents

List of Figures

List of Tables

Abbreviations

CQED	**C**avity **Q**uantum **E**lectrodynamics
CQD	**C**olloidal **Q**uantum **D**ot
CW	**C**ontinuous **W**ave
DBR	**D**istributed **B**ragg **R**eflector
DOS	**D**ensity **O**f **S**states
FWHM	**F**ull **W**idth **H**alf **M**aximum
ML	**M**onolayer **L**ayer
NC	**N**ano**C**rystal
NP	**N**ano**P**latelet
PL	**P**hoto**L**uminescence
QY	**Q**uantum **Y**ield
RoC	**R**adius **o**f **C**urvature
SPAD	**S**ingle **P**hoton **A**valanche **D**etector
TEM	**T**ransverse **E**lectric and **M**agnetic

Physical Constants

Speed of Light	c	=	$2.997\ 924\ 58 \times 10^{8}\ \mathrm{ms}^{-1}$
Planck's constant	h	=	$6.626 \times 10^{-34}\ \mathrm{Js}^{-1}$
Reduced Planck's constant	$\hbar$	=	$1.054 \times 10^{-34}\ \mathrm{Js}^{-1}$
Permittivity of free space	ϵ_0	=	$8.85 \times 10^{-12}\ \mathrm{Fm}^{-1}$
Boltzmann constant	k_B	=	$1.38 \times 10^{-23}\ \mathrm{JK}^{-1}$

Symbols

v_g	Group velocity	ms^{-1}
σ_{stm}	Stimulated emission cross-section	m^2
σ_{abs}	Absorption cross-section	m^2
$\tau_{Aug,bi}$	Biexciton Auger lifetime	ps
Γ	Confinement factor	
L	Cavity length	μm
V	Mode volume	m^3
τ_{rad}	Radiative lifetime	ns
F_p	Purcell factor	
R_{cav}	Emission rate	Hz
P_{th}	Lasing threshold	pJ
N_{conc}	Concentration	m^{-3}
η	Differential gain	
ς	Quantum yield	
g	Optical gain	m^{-1}
$\mathcal{L}$	Total cavity losses	m^{-1}
κ	Cavity decay rate	Hz
q	Mode number	
F	Finesse	
τ_{cav}	Cavity lifetime	ps
n	Refractive index	
T	Transmission	
Q	Quality factor	
ρ	Optical density of states	
ω_0	Mode waist	μm

β	Coupling factor	
$\Delta\lambda$	Free spectral range	nm
z_R	Rayleigh range	μm
$\mathcal{E}$	Electric field	Vm^{-1}
$\delta\lambda$	Spectral linewidth	nm
ϕ	Photon number	

Dedicated to my parents Kirit & Rekha...

Chapter 1

Introduction

1.1 Project Motivation

Colloidal quantum dots (CQDs) are nanometer sized semiconductor crystals consisting of roughly of 100-10000 atoms. These possess unique physical properties that arise from individual CQDs to packed CQD films providing a platform for exploring a rich variety of new physical phenomena as well as for the development of new class optoelectronic devices such as solar cells[1], photodetectors[2] and various light-emitting devices such as LEDs[3]. Their sub-10 nm size corresponds to the quantum confined regime, giving rise to a narrow emission band that can be tuned spectrally by controlling the size[4]. In addition, overcoating the CQDs with a shell of another inorganic semiconductor material (so-called heterostructures or core-shell structures) can increase their thermal stability as well as improve their quantum yield (QY), making them an attractive prospect for use as optical gain media[5]. Furthermore, in such CQDs the spacing between the electronic energy levels can far exceed the thermal energy at room temperature preventing depopulation of the lowest electronic states and providing temperature insensitive lasing thresholds. Organic passivating ligands that typically cover their surface also make them solution processable, offering the prospect of inexpensive lasing devices that can be made by printing CQDs onto large area or flexible substrates[6–8].

The optical gain lifetime in CQDs, however, is severely hindered due to strong competition non-radiative Auger recombination[9], which results from their small size and sharp confinement potentials. For this reason, high packing densities and high intensity pulsed excitation are required to obtain lasing, obstacles that need to be overcome if lasers utilizing CQDs as gain media are to be made commercially viable. The rapidly developing field of inorganic particle synthesis has enabled precise control on the size[4], shape[10–12] and composition[13] of CQDs, which can be used to curtail the effects

of Auger recombination by tailoring the interactions energies and spatial distribution carriers within CQDs.

The major objective of this project is to provide a detailed insight into relationship between the exciton and multiexciton binding energies, the Auger process as well as the competition between stimulated emission and absorption and the lasing behaviour of the CQDs. This will be done by performing gain spectroscopy enabled via in-situ tuning of the cavity feedback wavelength of open-access microcavities developed within our group. The cavities take the form of highly reflective Fabry-Pérot type mirrors with a planar-hemispherical geometry. In addition, by using this type of cavity architecture it is possible develop a platform for miniaturized and tunable, low threshold lasing devices, for example, for on-chip integration. These experiments will be performed using two different types of CQDs: spherical CdSe/CdS (Cadmium Selenide/Cadminum Sulfide) CQDs (referred to from hereon as nanocrystals, NCs)[14] and colloidal quantum wells (QWs) or nanoplatetes (NPs)[12, 15]. The latter have shown superior electronic and optical properties compared to NCs, including suppressed non-radiative Auger recombination of carriers[16], giant oscillatory strengths[17], large exciton binding energies[18] as well as higher absorption cross-sections[19]. Finally, it is hoped that the information obtained by performing gain spectroscopy on these structures can then be fed back into the fabrication of CQDs and films in which the lasing thresholds can be reduced to the point where useful devices can be manufactured and also in the design of resonant optical feedback structures for which the appropriate wavelength must be carefully selected.

1.2 Outline of Thesis

The chapters in this thesis will be organised in the following manner:

Chapter 2: Literature Review

This chapter will begin with the classification of CQDs in terms of their core and shell structure, which determine their electronic and optical properties. CQDs are almost always excited by photon energies well above their band gap, and ultrafast intraband relaxation is usually required to populate the emitting (band-edge) states, which also has important consequences for optical gain. The chapter will briefly mention how this occurs in CQDs, focusing mainly on NCs and NPs. The various non-radiative carrier relaxation processes that compete directly with the stimulated emission at these emitting states is then detailed. These processes including photocharging, photo-induced absorption and Auger recombination, and the various ways these processes can be overcome to achieve stimulated emission will also be highlighted. Finally, the chapter will end with

the discussion on the lasing achieved by incorporating CQDs into feedback structures of different shapes and sizes.

Chapter 3: Theoretical Background

This chapter will initially introduce the concept of quantum confinement in nanocrystals, which will lead to the discussion on their energy level structure, focusing specifically on NCs and NPs. A theoretical description of the condition necessary to achieve optical gain in CQDs will then be introduced, which will lead nicely to a theory of lasing using optical cavities. The open-access hemispherical cavity will then be introduced, including the concept of Hermite-Gaussian beam which fully describe the modes of the hemispherical cavity. Moreover, a consideration of the basic of cavity quantum electrodynamics will be needed to understand the interaction between the CQDs and optical modes of the cavity, specifically in the weak-coupling regime. Lastly, a rate equation model will be presented, which will be used in later chapters to describe the results of gain spectroscopy experiments.

Chapter 4: Experimental Methods

This chapter will introduced the methods used to characterise the CQDs, including photoluminescence, lifetime, absorption and pump-probe spectroscopy, that are crucial to the interpretation of the experimental results later on. The sample preparation will be mentioned, which is an important step in achieving low scattering rates and a high-packing densities, both of which are required to achieve lasing. A detailed description of the experimental set-up for the lasing experiments will then be given, along with cavity alignment procedure, again an important step in order to produce stable modes inside the cavity. The chapter will end with a short description on the methods to measure the spot-size and the concentration, which will be useful in theoretical analysis of the gain spectroscopy results.

Chapter 5: Gain Spectroscopy of CdSe/CdS Nanocrystals

The results of the gain spectroscopy of CdSe/CdS NCs are presented in this chapter. More specifically, the variation of the lasing threshold as a function of the spectral position is measured by tuning the length of the hemispherical cavity. Furthermore, the capability of such cavity architecture to produce in-situ tunable, single mode lasing is also demonstrated. The results are accurately described using an analytical theory, which represents an approximation to a dynamic system. The latter will provide an insight into the governing mechanism that determines the lasing behaviours of the CQDs, namely the interplay between the stimulated emission and the self-absorption of the lasing photons.

Chapter 6: Gain Spectroscopy of CdSe/CdS Nanoplatelets

This chapter will present the results of gain spectroscopy for the NPs. Like in the case of NCs, the lasing threshold as function of the cavity length will be measured and in-situ, single mode tunable lasing will be demonstrated. In addition, the stability of the laser is investigated by monitoring the length of time the intensity of the fundamental cavity mode is sustained, an important consideration for the practical realisation of the device. Finally, the gain spectroscopy results will be described using a rate equation model, giving an insight into the processes that govern the lasing behaviour.

Chapter 7: Conclusion and Future Work

In this chapter the results of the thesis will be summarised and some future work will also be discussed.

Chapter 2

Literature Review

2.1 Introduction

This chapter begins with a brief discussion on the different core-shell CQDs structures, which are the most commonly used types today. These can be classified in terms of their relative core and shell electronic energy levels as this governs the distribution of the electron and hole wavefunctions inside the CQDs, and these levels ultimately determine their electronic and optical properties of the CQDs. The intraband relaxation of carriers from the high energy states to the band-edge state is then discussed. This relaxation rate plays a central role in the applications of these CQDs in optoelectronics. This is because to achieve lasing CQDs are typically excited with high energy laser pulses at wavelength well above the band-gap. Ultrafast relaxation of the carriers within the conduction and valence bands is then required in order to efficiently populate the band-edge state involved in lasing.

The chapter then highlights the major difficulties that were encountered in some of the earlier efforts to achieve optical gain in core only CQDs. These were mainly attributed to trapping of carriers at the surface which is a direct result of the large surface area-to-volume ratio in strongly confined CQDs (with diameter less than 10 nm) and also the multiexcitonic non-radiative Auger recombination. The two main consequences of carrier trapping, namely photo-charging and photo-induced absorption and their implications for optical gain performance will be discussed as well as the methods used to overcome them. The condition to overcome Auger recombination in terms of the optical gain cross-section and the packing density of the CQDs will be stated. This will then lead to the discussion of the numerous others ways to overcome the Auger process through physical and chemical modification of the CQDs. Finally, the chapter will end with the

discussion of CQDs in resonators of various shapes and sizes to produce low threshold tunable, single and multimode lasing.

2.2 Core-Shell System Classification

The most commonly used CQDs now have an inorganic passivating layer encapsulating the core, known as the shell. The shell physically passivates the core by occupying trap sites on the surface of the core which could otherwise act as non-radiative recombination centres for the electron and holes. The shell provides additional protection from the environment such as preventing the effects of photo-oxidation. The shell is further terminated with organic ligands, which as well as providing additional passivation, also allows the CQDs to be dispersed in a wide variety of solvents and help prevent agglomeration.

The inorganic passivating shell consists of a semiconducting material different to that of the core. These core-shell systems can be classified as binary (core-shell) or ternary (core-shell-shell) architectures. The relative position of the electronic energy levels of the core and the shell material together with their crystal structure and lattice parameters govern their electronic and optical properties. Figure 2.1a compares the bulk conduction band minima and the valence band maxima of some of the common type II-VI and III-V semiconductor materials used to synthesize the binary and ternary architectures. It should be noted that the list of materials shown in Figure 2.1a is by no mean exhaustive and the reader is referred to other text for a more comprehensive list of materials used in the synthesis of CQDs[20]. The most extensively used CQDs have a binary structure and these can be classified as type I, reverse type-I and type II heterojunctions depending on the relative band offsets between the core and the shell material, as shown in figure 2.1b. A schematic of such a binary CQD is shown in figure 2.1c in the case of spherical CQDs and in figure 2.1d in the case of NPs, both of which are the subject of investigation in this thesis. Both are also shown to be encapsulated with organic ligands. The band offsets are determined by the choice of the semiconductor material as well as the confinement energy (i.e. the size of the core and shell), the effective mass of the carriers as well as lattice strain determined by their lattice mismatch[21].

Of the binary structures the most extensively studied are the type-I heterojunctions where the semiconductor core is surrounded by a shell of a higher band gap material[22–30]. Deposition of a multilayer shell on top of the core redshifts the emission and the absorption peak wavelengths due to the partial extension of the excitonic wavefunction into the shell which reduces the quantum confinement and lowers the effective bandgap[31]. Since the lowest energy configuration confines the electron and hole primarily to the core it produces a significant overlap between their respective wavefunctions, as shown

in figure 2.2a. The opposite is true for the reverse type I arrangement, where the shell has a lower band gap than the core and therefore electron and the hole are localised primarily within the shell[32–35], as shown in figure 2.2b.

Type II systems have staggered band alignment allowing one charge carrier to be localised primarily in the core and other in the shell [36, 37], as shown in figure 2.2c. The growth of the outer shell causes a significant redshift of the emission wavelength due to due smaller effective bandgap (smaller than each of the constituent core/shell materials) produced as a result of the staggered band alignment. The effective band gap can be controlled by changing the thickness of the core and the shell material through the quantum confinement effect. This allows their emission to be easily tuned over a wide wavelength range. For example, Kim *et al*[36] showed a emission tunable in the near infra-red from 700 nm to over 1000 nm for CdTe core overcoated with CdSe shell by changing the size of the core and the shell. Furthermore, in contrast to type I systems, the photoluminescence (PL) decay times are strongly increased due to the reduced overlap between and electron and hole wavefunctions [21]. Moreover, the spatial separation of charge carriers can create an internal electric field which can induce a Stark effect leading to significant shifts in the energies of multiexcitons[38]. This effect can be utilized to create ultralow threshold lasers operating in the single exciton regime, as will be discussed later in this chapter.

Interestingly, several of the type-I systems can be tuned to type-II by changing their shell thickness. For example, the core-shell system ZnSe/CdSe can behave as either inverted type-I or type-II depending on the shell thickness[32, 39]. In this system the bulk conduction band offset between ZnSe and CdSe is six times higher than the valence band offset[32]. This means for a certain shell thickness range ($\sim$ 1.1-1.6 nm) the energy level of the shell can be tuned such as to localise the electron into the shell whereas the hole can be delocalised across the entire CQD (core and the shell) allowing some degree of spatial separation of the carriers. Strictly speaking this is called the quasi-type-II regime due to delocalisation of the hole across the entire NC differentiating it from proper type-II structures where the hole would be localised primarily to the core. Similarly, another such structure is CdSe/CdS (which are used in this thesis). Here the CdSe core is coated with a CdS shell which has a higher bulk band gap. However, with increasing shell thickness the electron wave function becomes increasingly delocalised across the entire CQD while the hole is primarily localised to the core due to the small bulk conduction band offset[14], as shown in figure 2.2d.

One of the problems encountered when encapsulating the core with a shell of the another material is the lattice mismatch between the two materials, which can induce strain and introduce dislocations which are a source of non-radiative recombination and thus

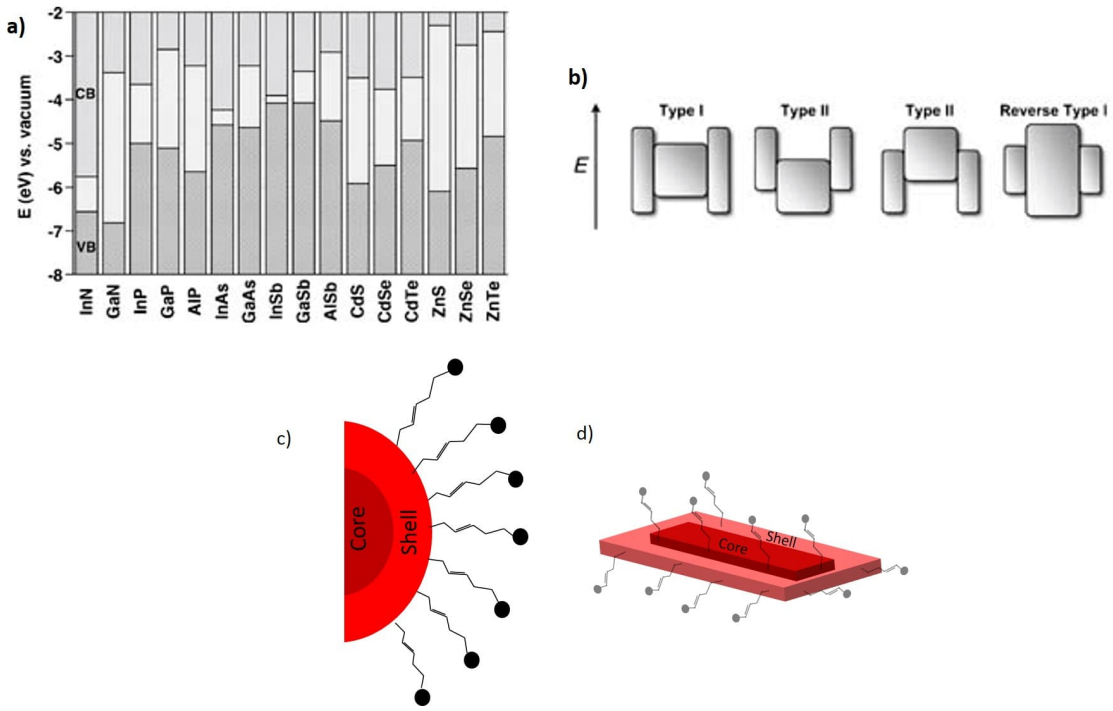

FIGURE 2.1: Relative band gap energies of bulk semiconductors and CQD classification. a) The relative bulk ionisation energies, electron affinities and band gaps (light grey) for the II-VI and III-V semiconductors (VB: valence band, CB: conduction band). b) The energy alignment of binary core-shell systems. The height of the boxes represent the band gaps and the lower and upper edges are the edges of the valance and conduction bands, respectively. Reproduced from reference [40] with permission. c) Schematic of a spherical core-shell CQD with encapsulating ligands. d) Schematic of a core-shell NP with encapsulating ligands.

reducing the quantum yield (QY)[41]. Therefore, this puts a limitation on the thickness of the shell which can be grown on top of the core. To address this issue a strain mitigating layer can be grown between the core and the shell with a lattice parameter and band gap in between that of the core and the shell material [42–44]. Thus, these ternary systems have improved QY due to the reduction in the number of defects compared to the core-shell structures and are more stable against the effects of photo-oxidation than compared to binary systems.

2.3 Collodial Quantum Dot Synthesis and Shelling

The synthesis of the CQDs in organic solutions can be achieved by a variety of different methods, the two most common being hot-injection[46] and heat-up techniques[47]. Both of these techniques require three main ingredients: the precursors, which provide the materials for the CQD synthesis, a coordinating organic solvent, and ligands, which as well as providing passivation mediate the growth of the CQDs. The formation of CQDs is described by the concept of "burst nucleation" which can be summarised by

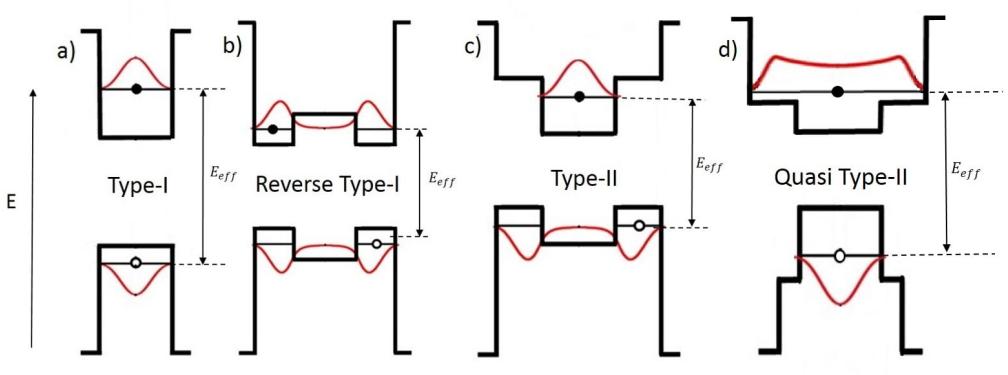

FIGURE 2.2: Spatial probability wavefunctions distribution of a) type-I b) reverse type-I c) type-II and d) quasi type-II core-shell structure. Here E_{eff} is the effective bandgap. The closed (open) circles represent electrons (holes). Modified from reference [45] with permission.

a three stage process[48–50]. The initial stage involves the pyrolysis (breakdown) of a precursors within an organic such that the ion (cation and anion derived from the precursor) concentration increases with time to reach supersaturation. When the degree of supersaturation is high enough, nucleation begins occur resulting in the formation of stable nuclei (stage two), which in turn depletes the concentration of the ions in the solution. Eventually, after ion concentration has dropped below a certain level, no new nuclei are formed and instead the nuclei begin to grow in size as long as the solution remains supersaturated (stage three).

Both the spherical CQDs and NPs used in this thesis were manufactured using the heat-up technique. In this technique the precursors (e.g. Cadmium myristate and Selenium for CdSe), ligands (e.g. oleic acid) and the solvents (trioctylamine in the case of spherical CQDs and octadecane in the case of NPs) are initially mixed at a low temperature (i.e. $\sim$ 30 min at 100 °C) and subsequently heated up to a higher temperature (210-260 °C for $\sim$ 10-20 mins) to promote nucleation and the subsequent growth. The advantage of using this technique is that it can be used to produce a large amount of highly monodisperse CQDs. In the case of NPs, an acetate salt such as Cd-acetate ($Cd(Ac)_2.4H_2O$) is swiftly added at an intermediate stage (after being heated to 210°C and the nucleation of the CdSe seed) and then re-heated again at 240 °C for $\sim$ 10 mins. The addition of an acetate salt promotes the lateral extension of the CdSe to form the NPs.

The addition of a inorganic shell around the core can be done by either by dropwise addition[45, 51] or by using the Successive Ion Layer Adsorption and Reaction (SILAR) technique[52]. In the dropwise addition technique the a mixture of the anion and cation precursors are slowly (i.e. $\sim 10^{-3}$ mol per hour) added to a heated solution of core-only CQDs inside a flask to for the core-shell structures. However, due to the high

temperature of the core-only solution of CQDs this method can lead to the nucleation of the shell precursors as well as defects during the growth of the shell, leading to drops in the QY. For this reason, the SILAR method was introduced whereby the shell is allowed to grow one monolayer at a time by alternating the injection of the shell precursors to a solution of core-only CQDs at high temperature. This technique was used to manufacture both the spherical CQDs and NPs used in this thesis. Since the precursors are not simultaneously present in the solution the probability of nucleation of the shell precursors is very low. Since the size of the shell can be controlled precisely this method be used to produce high quality "giant" CQDs with suppressed Auger rates[53](see section 2.6). After allowing the reaction mixture to cool, the final product is isolated from the reaction solvent (.e.g trioctylamine or octadecane) by the addition of ethanol and then precipitation by centrifugation, and eventually re-dispersed in the desired final solvent (e.g. hexane).

2.4 Intraband Relaxation In Colloidal Quantum Dots

As is often the case for semiconductor gain media, electrical and optical pumping creates electrons and holes which have energies well in excess of the band gap energy of the material (higher energy continuum states). The excited carriers relax back down to the band-edge state on an ultrafast (sub-ps) timescale. This intraband relaxation process must happen faster than the carrier recombination due to radiative and non-radiative processes in order to ensure an efficient build-up of the band-edge (or the emitting state) population since it is the band-edge state that is responsible for producing PL, and ultimately, lasing. These relaxation processes are strongly dependent on the dimensionality on the material. The intraband relaxation in the case of bulk II-IV semiconductors occurs predominantly via Fröhlich interactions with longitudinal optical (LO) phonons[54, 55].

However, whereas in the bulk semiconductor there is a continuum of energy states available which facilitates the intraband relaxation process the separation between the energy levels is much larger in CQDs due to the quantum confinement experienced by the carriers. When the energy level separation reaches even a small fraction of the typical phonon energies, carrier relaxation via phonon interactions becomes increasingly prohibitive as a result of restrictions imposed by energy and momentum conservation. This phenomena is known as the "phonon bottleneck" and has been theoretically predicted to occur in 0-D systems [56–58]. For example, in the case of CdSe NCs, whereas the hole energies in the valence band are closely spaced[59], the spacing between the low lying electron energy levels in the conduction band is much greater due to the lower effective mass of

the electron. This is especially true in strongly confined NCs (where size of the NCs becomes comparable to or smaller than the exciton Bohr radius, which is the natural length scale for the excitons in the system) where the electron energy level spacing can exceed many times that of the typical LO phonon energies. Despite theoretical evidence, however, ultrafast electron intraband relaxation from a higher lying energy state (1P) to the band-edge state (1S) in CdSe NCs (see section 3.3.1 for more detailed information on the electronic structure) has been experimentally observed[60–64], with lifetimes below 1 ps.

Several mechanisms have been proposed which can overcome the phonon bottleneck to explain such ultrafast carrier relaxation in CQDs. For example, Efrosa *et al*[65] suggested a process where the electron energy from the 1P electron state can be rapidly transferred ($\sim$ 2 ps) to the hole allowing the electron to relax to the lowest 1S state. Due the smaller inter-level spacing of the hole states the excess hole energy is then rapidly (sub-picosecond) dissipated via phonon interaction allowing the hole to relax back down to the band-edge state. This Coulomb mediated process is often referred to as the Auger process (as distinguished from the multiexciton Auger process discussed in section 2.5.3) and can remove the phonon bottleneck in strongly confined NCs. Guyot-Sionnest *et al*[66] suggested two alternative mechanisms which can provide efficient intraband relaxation pathways. One is a vibrational mechanism where energy is transferred to the vibrational modes of the ligands used to passivate the NCs allowing the electron to relax to the 1S state. Another is the electronic or "defect-assisted" mechanism, first proposed in the context of epitaxial quantum dots[67], where the electron is able to relax to the 1S state via an intermediate electronic defect state created by the covalent bond between the Cd^{2+} ions on the surface of CdSe NCs and the ligands. By capping the NCs with the appropriate ligand this defect state can be shifted above the 1P state, thus suppressing the electron transfer from this state and extending the 1P-1S relaxation lifetime.

The nature of intraband relaxation, however, is very much dependent on the dimensionality of the CQDs. For example, in extended quantum systems such as NPs and quantum rods a transition from discrete to quasi-continuous density of states (DOS) occurs. It has been observed experimentally that high energy carriers (both electron and holes) in these systems will rapidly ($\sim$ 300 fs) cool efficiently via phonon emission [68, 69] just like in the case of bulk semiconductors.

2.5 Competition Between Optical Gain and Non-radiative Carrier Relaxation

As discussed in the previous section, efficient intraband relaxation within the conduction and valance bands leads to the occupation of the lowest electron and hole energy levels in CQDs. Depopulation of the these states occurs via both radiative and non-radiative relaxation, the latter being highly detrimental to optical properties of CQDs. This section will discuss the implications of the two primary non-radiative relaxation processes that can occur in CQDs, namely trapping at surface states and the multiexcitonic non-radiative Auger recombination, on the optical gain properties of CQDs.

2.5.1 Photocharging

Photocharging is a the direct result of two non-radiative processes that can depopulate the charge carriers from their band-edge state: charge carrier trapping and Auger recombination. Charge trapping refers to the localisation of either the electron and or hole at a trap site on the surface of the CQD inducing spatial separation between the two carriers. In single CQDs this process is thought to be responsible for producing pronounced fluctuations in the emission intensities over time under continuous illumination. This phenomenon is known as fluorescence intermittency or "blinking" and was initially observed by the pioneering works of Nirmal *et al* [70].

Two distinct mechanisms have been proposed to explain CQD blinking, which can be classified as A-type and B-type blinking[71]. In type-A the CQD core is left charged resulting from an ejection of one of the carriers from the core due to the Auger process (see section 2.5.3). Subsequent absorption of a photon results in the creation of a trion (exciton with an excess charge). The trion can recombine non-radiatively by the Auger process outcompeting the much slower radiative recombination. This is when the CQD is in the "off" state as the emission intensity during this process is greatly reduced. Alternatively, in poorly passivated CQDs a carrier residing in the band-edge state can become trapped in a long-lived surface state leaving behind a charged core allowing the formation of a trion, which then combines non-radiatively. This cycle repeats until the CQD is neutralised with the injection of the carrier back into the core allowing radiative recombination to occur again, returning the NC to the "on" state as radiative recombination dominates again. Thus, the blinking refers to the periodic switching between "on" and "off" states over time. In type-B blinking occurs when a "hot" carrier, created by pump photon with energy well above the band gap, is occasionally intercepted by a higher energy long-lived trap site before getting the chance to relax to

the band-edge state. The trapped carrier can then recombine non-radiatively with the carrier inside the core before the next excitation event leaving behind a neutral NC[72]. In an ensemble of CQDs, build of such charges over time can lead to reduced QYs[73] and can ultimately degrade their lasing performance, however, its effects can be mitigated by overcoating the cores with a passivating shell of adequate thickness[74].

2.5.2 Photo-induced Absorption

Another consequence of carrier trapping at surface states for CQDs dissolved in organic solvents is the phenomena known as photo-induced absorption (PA). Solvent related PA was mostly likely responsible for some of the previous unsuccessful attempts to achieve optical gain in NCs dissolved in organic solvents[75, 76]. Malko *et el*[77] examined the effect of PA on the optical gain properties of core-only CdSe NCs for radii ranging from 1.2 nm - 3.5 nm, using a technique known as pump-probe or transient absorption (TA) spectroscopy (see section 4.2.3). The NCs were dissolved in various commonly used solvents such as toluene, chloroform and heptamethylnonane. For small NCs (radius = 1.2 nm) no optical gain was detected for the entire spectral range under examination for NCs immersed in any of these solvents, even for excitation as high as six electron and hole pairs per NC on average.

However, optical gain was detected at the position of the emitting transition for NC with a radius larger than 2.3 nm. In fact, the absence of optical gain for smaller NCs was attributed to trapping of the carriers at the NC surface which subsequently leads to induced absorption (PA) due to carriers excited into the unoccupied states in the surrounding solvent. The probability of trapping can therefore be reduced by either coating the NCs with a shell to provide passivation or by increasing the size of the NCs to lower the surface area-to-volume ratio, reducing the number of trap sites. In this case, Malko *et el*[77] showed that PA was almost completely eliminated in closed-packed matrix free films of NCs formed by drop casting of hexane solution containing the NCs, allowing optical gain to be observed even in the smallest of the NCs with radius 1.3 nm. The above is consistent with other studies where almost complete suppression of PA and optical gain is demonstrated for NCs incorporated in sol-gel titania matrix [78, 79] and in matrix free closed-packed NC films [80–83].

2.5.3 Auger Recombination

The band-edge state in CdSe is two-fold degenerate due to the carrier spin and, thus, population inversion and lasing requires the existence of a biexciton (see section 3.4.1). A fundamental complication that arises in CQDs containing multiple excitons is the

Coulomb mediated non-radiative Auger recombination [84]. This is when an electron and a hole recombine by transferring their energy to a third carrier instead of emitting a photon[84]. This process is relatively slow in bulk semiconductors due to the thermal activation barrier which needs to be overcome in order to satisfy momentum conservation [85]. However, the Auger process become more efficient in CQDs as a result of their abrupt heterointerfaces (between semiconductor/solvent or semiconductor/ligands or the core-shell), which relaxes the momentum conservation rule and thus removes the thermal activation barrier[86, 87]. Consequently, the decay of multiexcitons is dominated not by radiative emission (where lifetimes range in several tens of nanoseconds) but by the ultrafast non-radiative Auger recombination[9, 88, 89]. This puts in intrinsic limitation on the lifetime of optical gain in CQDs.

For this reason, the presence of optical gain does not guarantee the development of stimulated emission and lasing. In order overcome Auger process the stimulated emission build-up time must be faster than the Auger-dictated gain lifetime. In the case of NCs, the stimulated emission build-up time, τ_s, is governed by the following equation [82]:

$$\tau_s = \frac{4\pi R^3 n_r}{3\zeta\sigma_g c} \tag{2.1}$$

where R is the NC radius, n_r is the sample refractive index, ζ is the NC packing density (volume fraction), σ_g is the NC gain cross-section and c is the speed of light.

In the case where the gain decay is governed by the biexciton lifetime (τ_2) stimulated emission can only occur of if $\tau_s < \tau_2$. Since $\tau_2 \sim \beta R^3$[9, 76], where β is a scaling factor this gives a condition on the minimum packing density required to achieve stimulated emission:

$$\zeta > \frac{4\pi n_r}{3\sigma_g \beta c} \tag{2.2}$$

Taking the lower estimate of the gain cross section of $\sigma_g \sim 2 \times 10^{-17}$ cm^2[82] and a upper estimate of the refractive index of $n = 2$ and $\beta \sim 5$ ps nm^{-3} [82], equation 2.2 indicates that the critical packing density required to achieve stimulated emission is $\zeta \sim 0.003$ (0.3%). Volume fractions as high as 12% and 20% have been achieved in sol-gel titania matrices containing NCs[78] and in closed-packed NC films[82], respectively. For example, Mikhailovsky *et al*[83] demonstrated tunable amplified spontaneous emission (ASE) with the wavelength ranging from 540-640 nm using CdSe NCs of radius $R =$ 1.3 -2.5 nm from closed-packed films fabricated by drop casting solutions of CdSe NCs onto glass slides. ASE is spontaneous emission that is amplified by stimulated emission

producing a laser-like beam that can be intense and of relatively narrow divergence and is seen as a the appearance of a spectrally narrow peak on top of the inhomogeneously broadened PL spectrum, as shown in figure 2.3a (dashed line). Figure 2.3a also shows a TA curve indicating the development of optical gain (α <0, where α is the excited state absorbance) which spectrally coincides with the ASE peak (black solid line).

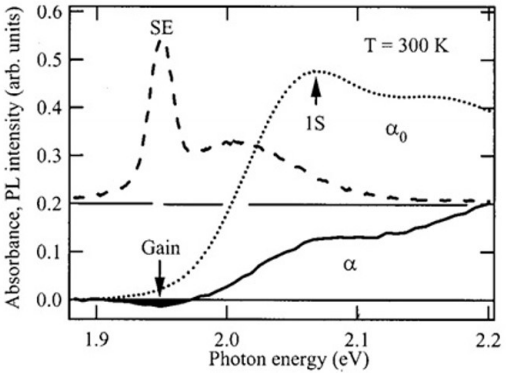

FIGURE 2.3: Optical gain and ASE. Stimulated emission (SE) spectrum of CdSe NCs is seen as a spectrally narrow peak red-shifted with respect to the PL maximum. Optical gain (α <0) is measured in TA at the same spectral position as ASE peak. The ground state absorption (α_0) is also shown for comparison. Reproduced from reference [83] with permission.

It is important to note that for all of the above experiments optical gain has been achieved using a pulsed excitation and not with continuous wave (CW) excitation. The reason for this is as follows. The average exciton number per NC is given by $\langle N \rangle = \sigma_{abs} J$[9], where σ_{abs} is the absorption cross-section at the excitation wavelength and J is the fluence (number of photons per unit area per pulse). Assuming at threshold we need $\langle N \rangle = 1$ (see section 3.4.1) the threshold pump fluence (J_{pul}) is then given by:

$$J_{pul} = \frac{1}{\sigma_{abs}} \tag{2.3}$$

The threshold pump intensity for CW excitation (J_{CW}) can then be estimated by the ratio of J_{pul} and the biexciton Auger lifetime ($\tau_{Aug,bi}$)[83]:

$$J_{CW} = \frac{1}{\sigma_{abs}\tau_{Aug,bi}} \tag{2.4}$$

Since both the absorption cross-section (for energies well above the band gap) and the biexciton Auger lifetime are proportional to R^3[9, 76] (R is the NC radius) the threshold fluence for CW is then proportional to R^{-6}. On the other hand the threshold fluence for pulsed excitation scales as R^{-3}. Thus, pumping with CW becomes progressively less

efficient with decreasing NC size indicating that the pulsed excitation is more efficient, so long as the pulse duration is smaller than the biexciton Auger lifetime.

2.6 Methods of Auger Suppression to Improve Optical Gain Performance

As mentioned in the previous section population inversion in CdSe NCs can only be achieved in the multiexciton regime. This puts an upper limit in the optical gain lifetime due to the intrinsic ultrafast non-radiative Auger process, which seriously diminishes technological potential for their use as optical gain media. The following section will discuss the several attempts people have made to reduce the Auger rate by physically and chemically modifying the structure of the CQDs and their implications on optical gain performance.

One these approaches is to use the so-called "giant" core-shell structures. Since the Auger process is mediated by Coulomb interactions it has been shown that this rate can be reduced by increasing the volume of the CQDs[9, 90]. Htoon *et al*[91] used CdSe NCs coated with up to 16 ML CdS shell ("giant NCs) to demonstrate emission from multiexcitons of order as high as six (six electron- hole pairs). Since the conduction band offset is much lower in these core-shell structures adding a thick shell allows the electron wavefunction to spread across the core and the shell increasing its occupation volume. In addition such band alignment also induces spatial separation of the electron and hole wavefunctions, which helps in lowering the Auger rate further. In fact, such electron and hole separation can also create significant non-zero local charge density associated with NCs containing single excitons, leading to strongly repulsive exciton-exciton interactions and shifting the biexciton energy above twice the single exciton energy[92]. If this interaction energy greatly exceeds the transition linewidth (inhomogeneous) the reabsorption of the photon in a NC containing a single exciton is completely suppressed, thus enabling stimulated emission to occur in the single exciton regime where the Auger process is inactive. As such, Klimov et al[38] used type-II CdS/ZnSe core-shell NCs to demonstrate ASE in the single exciton regime with gain lifetime as long as 1700 ps, fifty times longer than for core-only CdSe NCs ($\sim$ 30 ps) measured in the same study.

Another strategy involves the use of a smooth confining potential across the core-shell heterointerface, which has been shown to markedly suppress blinking indicating a significant reduction in the Auger rate[93]. Garcia-Santamaria *et al*[94] used this property to demonstrated optical gain from CdSe/CdS NCs with a much broader gain bandwidth ($\sim$ 500 meV) than can be achieved from biexciton emission alone by using emission from

higher order excitons. Here the long reaction times involved in the growth of the NCs results in the inter-diffusion of Se and S atoms across core-shell interface producing a smooth alloyed layer and a graded confinement potential. Furthermore, Guzelturk *et al*[95] demonstrated ASE threshold of $\sim$ 30 μJ cm^{-2} from films of CdSe/CdS (120 fs pump pulse width), one of the lowest reported thresholds for CQDs. The low threshold was attributed to the smooth confinement barrier formed between the CdSe and CdS materials resulting from the extremely high temperature (310 °C) and a very slow rate of growth rate of the CdS shell.

Relatively recently, methods have been developed to synthesize a new class of flat semiconductor nanoparticles known as colloidal QWs or nanoplatelets (NPs)[12, 15]. In these structures, carriers are confined only in one direction exhibiting an electronic structure similar to epitaxially grown QWs. Quantization in only one direction in these structures imposes stricter momentum conservation rules compared to the zero dimensional NCs, strongly suppressing their Auger recombination rates. Such suppression of the Auger rates has allowed the demonstration of ASE with thresholds[96] that are approximately four times smaller than the best reported threshold values in literature in the case of NCs[94]. In addition, Grim and co-workers[97] were able to demonstrate lasing from biexcitons using CW excitation for the first time using CQDs in closed-packed films of core-only CdSe NPs. However, although the strong Auger suppression plays a major role in obtaining low stimulated emission thresholds for NPs, several other factors also need to be considered. The large size of the NPs increase their absorption cross-section at the excitation wavelength, thus lowering the ASE threshold further. The exciton binding is also expected to increase with decreasing width of the NPs, as predicted theoretically for QWs structures [98] and further increase is expected resulting from the lower dielectric environment of the NPs (e.g. of the ligands)[18]. Moreover, QWs exhibit a phenomena known as giant oscillator strength transition (GOST) connected with the in-plane extension of the exciton centre of mass motion[99] and which has been observed experimentally in NPs[17]. The increase in the binding energy for NPs and the GOST effect results in a high oscillator strength and thus high optical gain cross-sections for the NPs, which helps to lower the gain threshold even further.

2.7 Colloidal Quantum Dot Lasing

True lasing action can be achieved by placing a high density gain medium inside an optical cavity. The purpose of the cavity to provide efficient feedback allowing stimulated emission to build by repeated reflections of the photons through the gain medium, as well as provide a higher degree of monochromaticity, directionality and brightness. The

need for a tunable, more compact and efficient sources of lasers has fuelled a large body of research using microcavities of various shapes and sizes in the solid state. With the conditions to achieve stimulated emission (ASE) in CQDs established the chemistry needed to incorporate them into various feedback structures was subsequently developed. This section will focus on the use of some (but by no means all) of these feedback structures in the realisation of low threshold, tunable lasing utilizing CDQs as gain media.

One such structure is the Distributed FeedBack (DFB) laser, consisting of a slab waveguide which is patterned with a grating structure like the one shown in figure 2.4. Lasing is achieved by photons traversing the grating which provides feedback through the periodic modulation of the local refractive index as result of the grating structure. The advantage of such structures is that laser emission can be tuned by simply changing the size of the NCs and the effective refractive index (determined by the loading fraction of the NCs in the film) whilst keeping the grating periodicity constant. For example, Guilhabert *et al* [100] showed DFB lasers that can be made to operate over a spectral range of 11 nm (604-616 nm) using a CdSe/ZnS composite by fine-tuning the either the gain material thickness or the grating periodicity. Furthermore, by optimising the design of the DFB laser to ensure a good overlap between the lasing mode and the CQD gain material, lasing was obtain using an excitation source with a pulse duration of 5 ns, with a threshold of 0.5 mJ/cm^2, the first ever demonstration of a DFB laser operating in the nanosecond regime. This work was extended by McLellan *et al*[101] where lasing threshold as low as 13.5 μJ/cm^2 was reported from CdSe/ZnS CQDs, pumped with 5 ns pulses, as well as producing an output of 40 nJ at 600 nm emission wavelength. The performance was made possible by using alloyed core-shell CdSe/ZnS to mitigate the effects of multiexcitonic Auger recombination (see section 2.6) and also by integrating a layer on top of the CQD film made from polyvinyl alcohol (PVA) for better mode confinement. The realisation of lasing in the nanosecond regime using CQDs as gain media makes them compatible to be used with compact solid-state pump lasers[102] also operating in the nanosecond regime, making them a step closer to the practical realisation of such CQD lasing devices.

Moreover, Eisler *et al*[103] was able to extend the tuning range to $\sim$ 56 nm (565-621 nm) by using CdSe/ZnS CQDs of different sizes, but using a grating with the same periodicity. Finally, Foucher *et al*[104] demonstrated another method of tuning the cavity wavelength by using a mechanically flexible thin glass substrate onto which sits the polymer grating coated with a CdSe/ZnS CQD film. The advantage of such a system is that the wavelength can be tuned in-situ by bending the glass substrate to produce either a positive RoC (inducing a red-shit of the emission wavelength) or a negative RoC

(inducing a blue-shift) of the structure. In this manner, Foucher *et al*[104] demonstrated lasing over a spectral range of 18 nm (600-618 nm).

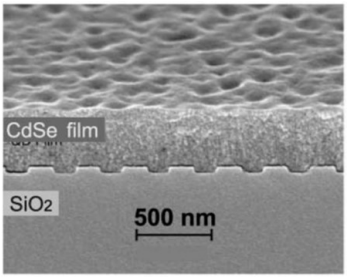

FIGURE 2.4: Distributed feed-back lasing. a) A scanning electron micrograph (SEM) image of the distributed feed-back grating coated with a thin layer of CdSe NCs. Reproduced from reference [105] with permission.

Another class of structures are microresonators that can support whispering gallery modes (WGMs) by confining light by total internal reflection on their inner surface. The strong photon confinement within the mode volume can result in quality factors as high as 100 million[106, 107] helping to reduce the lasing thresholds. Snee *et al*[108] developed a simple method to produce stable and reproducible lasing by incorporating CdSe/CdZnS NCs onto the surface of dielectric microspheres (made from commercially available silica or polystyrene templates), such as the one in figure 2.5a. Laser emission in multimode regime ($\sim$ 620-680 nm) can be observed from the many WGM supported by the microspheres and in the single mode regime by changing the size of the microspheres (such as to include only one mode within the stop-band) and tuning the NC emission into resonance by changing their size. By changing the size of the microspheres and using the appropriate NCs the laser emission can also be tuned, as demonstrated by Chan *et al*[109] where laser emission in the blue region (central wavelength $\sim$ 480 nm) was produced using CdS/ZnS NCs. Min *et al*[110] demonstrated ultralow lasing threshold ($\sim$ 9.9 fJ per pulse with femosecond excitation at 388 nm) using toroidal microcavity by spin-coating CdSe/ZnS NCs on its surface, such as the one shown in figure 2.5d. Such low threshold lasing was possible due to the high Q-factors compared to microsphere resonators of comparable diameter[107] due to their lower mode volumes, but also due to the efficient evanescent coupling of the pump beam to the toroidal microcavity through a tapered-fibre geometry. Additionally, these structures can provide another advantage over microspheres in that they can be manufactured lithographically at predefined locations on a silicon chip. In-situ tuning of the laser emission can also be made possible by electrically tuning the cavity resonances of such a cavity structures as demonstrated in the work by Armani and co-workers[111].

Finally, another class of microcavity structures worth mentioning here are the vertical cavity surface emitting lasers (VCSELs), formed by sandwiching an active gain medium

in between two high reflectivity mirrors typically made from alternating layers of materials with different refractive indices (i.e. DBRs, see section 3.5.2)[112, 113]. Here, the laser emission occurs perpendicular to the surface of the cavity, and due to the small cavity length that can be attained (1-2 μm i.e. small gain medium length), they can be made very compact and the scattering and absorption losses are minimised, enabling low threshold laser operation. As such, Dang *et al*[113] demonstrated an optically pumped VCSEL laser made from alloyed CdSe/ZnCdS CQD film integrated between two DBRs made from alternating layers of SiO_2/TiO_2. Similarly, Menon *et al*[112] created a VCSEL laser using InGaP CQDs as gain material placed between alternating layers of polyN(vinylcarbazole)(PVK), and cellulose acetate (CA), all of which was supported on top of a glass substrate. At advantage of using materials to make the DBRs is that the entire cavity structure can be subsequently peeled off from the glass substrate to create a free standing mechanically flexible cavity which can confirm to any desired shape.

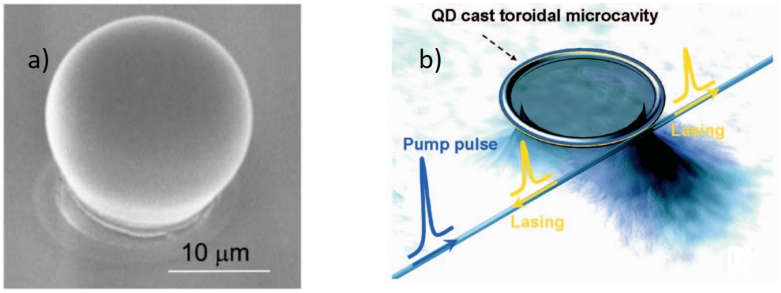

FIGURE 2.5: Microresonator geometry. a) A SEM image of a microsphere coated with CdSe/CdZnS NCs. Reproduced from reference [114] with permission. b) Schematic representation of a tapered-fibre coupled toroidal microcavity. Laser emission occurs bi-directionally via the tapered fibre. Reproduced from reference [110] with permission.

2.8 Conclusion

In this chapter the classification of the CQDs in terms of their core-shell structure was introduced. Efficient intraband relaxation of the carrier in the conduction and the valence bands was found to exist in all CQDs (NCs, rods and NPs). For spherical CQDs an Auger type process was shown to overcome the problem of the phonon-bottle neck resulting from the well-spaced energy levels in the conduction band. It was highlighted that intraband relaxation becomes more efficient in higher dimensional CQD s (rods and NPs) where a transition to a quasi-continuous DOS occurs.

Then, some of the major challenges encountered in the early attempts to produce optical gain were highlighted. These were mainly as a result of the carrier trapping at the surface states and due to the multiexcitonic non-radiative Auger recombination. The trapping can lead to charging of the CQDs and to a phenomena known as photo-induced

absorption, both of which strongly compete with the optical gain. It was shown that the effects of charging can be reduced by overcoating the CQD cores with a thick shell and also by utilizing closed-packed films to eliminate the solvent responsible for producing photo-induced absorption.

Furthermore, the use of closed-packed films with high CQD density was shown to overcome Auger recombination to enable stimulated emission in spherical CQDs. Several other methods of overcoming Auger recombination to improve the optical gain performance were then highlighted, which involved the physical and chemical modification of the CQDs. Furthermore, by tailoring the interactions energies (type-II CQDs) of the excitons lasing the single exciton regime can be obtained, eliminating the problem of Auger recombination completely.

Finally, lasing from CQDs produced by using feedback structure of various shapes and sizes was demonstrated by using resonators of different sizes and the CQD to match their emission to the resonator stop-band.

In-situ tunable cavities and laser emission have been demonstrated using various methods. For example, the shape of the cavity can be tuned by external heating achieved through either modulating the pump power[115] or by directly heating the cavity using an electrical heater[116]. Other methods have utilised strain[117], electric-field[111, 118], or pressure[119]. However, these methods tend to either have too limited a tuning range for useful spectroscopy, which is the primary purpose of using cavities in this project, or involve changes to the CQD environment that may themselves modify the gain characteristics. This makes the interpretation of the observed changes in lasing performance difficult. By directly tuning the cavity length of a Fabry-Pérot style open resonator, such cavities can achieve both a wide tuning range and fine control limited only by the resolution of the actuator. The CQDs in solution within the cavity experience no change in temperature or stress during tuning and so the changes in lasing performance can be attributed unambiguously to the change in feedback wavelength.

Chapter 3

Theoretical Background

3.1 Introduction

In this chapter the concept of quantum confinement is introduced, which leads to significant modification of the electronic DOS in CQDs as a result of the quantisation of the energy levels. This concept is extended to core-shell systems allowing the classification of the CQDs in terms of their different localisation regimes. The energy level structure of spherical CQDs and NPs is then introduced, which are the two systems used in this thesis. The condition for optical gain in these structures is then detailed, including the role played by the exciton-exciton interactions energies. This will lead to the basic theory of lasing (gain vs loss), and where some of other important parameters that can be quantified in lasing will be introduced, namely the slope efficiency (or differential gain) and the linewidth.

The basic principles of the Fabry-Pérot cavity is then outlined and some key cavity parameters, namely the Q-factor and the finesse, are introduced. The purpose of using a cavity is to provide efficient feedback allowing stimulated emission to build by repeated reflections of the photons through the gain medium, but which also assists in producing highly directional emission. Furthermore, due to interference effects the cavity selects out certain frequencies of radiation with a linewidth much smaller than the spontaneous emission linewidth involved in the transition, thus providing a higher degree of monochromaticity.

Moreover, the method of photon confinement for the cavities used in this experiment, the distributed Bragg reflectors, is then highlighted. This then leads nicely into the description of the plano-concave or hemispherical cavities used in this project. Initially, the concept of the Gaussian (and the Hermite-Gaussian) beams, which perfectly describes

the optical modes of the hemispherical cavities used in this project will be introduced. The quantum mechanical description of the coupling of CQDs to these cavities (cavity quantum electrodynamics) is then outlined. It will be seen that the presence of the cavity strongly modifies the optical DOS from the free-space which leads to the modification of the emission characteristics of the CQDs, such as their emission lifetime, which is known as the Purcell effect. A remark on the consequences of homogenous broadening on the CQD-cavity coupling is made, which results from electron-phonon interactions in CQDs at room temperature. The chapter ends with an introduction to a rate equation model that describes the lasing behaviour. By using an arbitrary set of parameters the rate equations are solved to produce a power dependence curve from which the lasing threshold can be extracted.

3.2 Quantum Confinement in Colloidal Quantum Dots

Many of the absorption and emission features in CQDs can be understood in terms of the quantum confinement. The CQD imposes a confining potential on the electron, hole or the exciton in one, two or all three dimensions depending on the shape, and which therefore strongly modify the electron and hole wavefunctions. Such spatial confinement of carriers also strongly modifies the optical DOS of CQDs. For example, using such approach Ivanov et al[45] theoretically calculated the distribution of electron and hole wavefunctions for spherical CdS/ZnSe core-shell NCs for a range of different core and shell thicknesses. The degree of electron and hole overlap can be evaluated using the overlap integral[45]:

$$\Theta_{eh} = |\langle \psi_e | \psi_h \rangle|^2 \tag{3.1}$$

where ψ_e and ψ_h are the electron and the hole wavefunctions, respectively. Similarly, the radiative decay rate τ_{rad} is also proportional to the electron and hole wavefunction overlap[120]:

$$\frac{1}{\tau_{rad}} \propto |\langle \psi_e | \mathbf{V} | \psi_h \rangle|^2 \tag{3.2}$$

where $\boldsymbol{V} = \mathrm{e}.\boldsymbol{r}$ is the dipole moment. However, the measured radiative lifetime (τ) is a mixture of the radiative (τ_{rad}) and the non-radiative (τ_{nr}) components[121]:

$$\frac{1}{\tau} = \frac{1}{\tau_{rad}} + \frac{1}{\tau_{nr}} \tag{3.3}$$

This then also helps to define the quantum yield (QY) as[121]:

$$QY = \frac{\tau}{\tau_{rad}} \tag{3.4}$$

3.3 Energy Level Structure of Colloidal Quantum Dots

As mentioned in the previous section quantum confinement strongly modifies the energy level structure in CQDs from the continuous energy bands of a bulk semiconductor. This is further complicated by additional effects that need to be taken into account in order to accurately describe the absorption and emission spectra of the CQDs. For example, the absorption properties of the CQDs can only be explained by taking into account the effects of the spin-orbit interaction and the confinement induced-mixing of the valence bands. Furthermore, the presence of strong electron and hole exchange interactions, shape asymmetry and the crystal field gives rise to band-edge exciton fine structure, the description of which is needed to explain the emission properties of the CQDs.

3.3.1 Nanocrystals

A bulk semiconductor is characterised by a continuous conduction and valence band structure with an energy gap E_{bulk} (figure 3.1a). In the case of NCs the spherical confinement potential gives rise to an independent series of atomic-like states with an energy gap E_{NC} (figure 3.1b). These states can be classified by two quantum numbers. The first one, L, denotes the angular momentum of the envelope wavefunction describing the motion of the carriers in the confinement potential. The other is n, which denotes the number of the energy level in the series of energy levels of a given angular momentum. The conventional notation for labelling the quantum states of the NCs is the number n followed by the L (S for $L = 0$, P for $L = 1$, D for $L = 2$ etc..), as seen in figure 3.1b.

In CdSe NCs the conduction bands are formed from the Cd 5s atomic orbitals and the valence bands from the Se 4p orbitals. For this reason the energy level structure of the valence bands is modified by the spin-orbit interaction. This interaction splits each of the individual hole states into three sub-bands, namely the heavy-hole (hh), light-hole (lh) and the split-off (so) band, as shown in 3.1c. The hh and lh sub-bands have a unit cell angular momentum (contribution from the carrier spin and the atomic orbital) $J = \frac{3}{2}$ and the split-off band has $J = \frac{1}{2}$. Away from $k = 0$, where k is the magnitude of the wavevector, the hh and hl sub-bands are further split according the projection of the unit cell angular momentum component onto the z-axis (i.e. $J_z = \pm\frac{3}{2}$ for the hh and

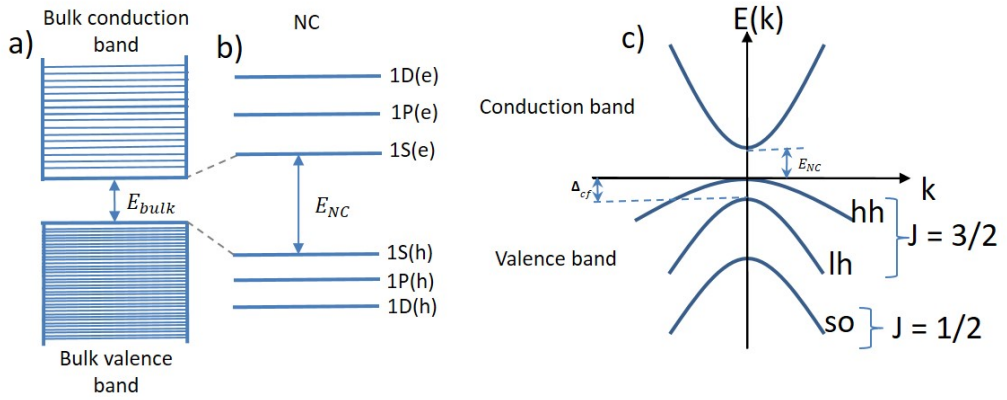

FIGURE 3.1: Energy level structure of the bulk semiconductor and nanocrystals. a) A bulk semiconductor containing continuous conduction and valence band energy levels with a bulk band-gap of E_{bulk}. b) The atomic-like energy level states of the NC with a band-gap of E_{NC} which is size-dependent. c) Spin-orbit interaction splits the valence band into the heavy-hole (hh), light-hole (lh) and the split-off band (so). Δ_{cf} is the crystal field splitting which exists for a hexagonal lattice.

$J_z = \pm\frac{1}{2}$ for the lh). For NCs with a hexagonal crystal structure crystal field further splits the hh and hl sub-bands at $k = 0$ by amount Δ_{cf}.

However, the valence band Hamiltonian contains contributions from both the crystal lattice as well the confinement potential and so neither J or L quantum numbers are conserved. Instead only the total angular momentum $F = J + L$ and the parity are conserved. The confinement potential further mixes with hole states with angular momentum L and $L + 2$ (known as S-D mixing) [122], but with the same F. The energy states are then labelled as nL_F. For example, for the lowest energy state in the valence band, identified as $1S_{\frac{3}{2}}$, is a mixture of three hole components: ($F = \frac{3}{2}$, $J = \frac{3}{2}$, $L = 0$), ($F = \frac{3}{2}$, $J = \frac{3}{2}$, $L = 2$), ($F = \frac{3}{2}$, $J = \frac{1}{2}$, $L = 2$). Finally to fully describe the valence band spectrum the confinement induced mixing between the hh, lh and so sub-bands also needs to be taken into account[123]. According to such treatment some of the lowest excitonic transitions for CdSe are shown in figure 3.2a, and which is in excellent agreement with the experimentally measured absorption spectrum in figure 3.2b.

Whereas as the confinement induced mixing can accurately describe the absorption spectra of the NCs their emission properties can only be understood by considering fine structure of the band-edge state, labelled as $1S(e) - 1S_{\frac{3}{2}}$ figure 3.2a. As was mentioned in chapter 2 the band-edge state is eight-fold degenerate, however, these degeneracies will be lifted as a result of the crystal field splitting (hexagonal crystal structure)[125], deviations from the perfect spherical shape of the NCs[126] as well as strong electron-hole exchange interactions[127].

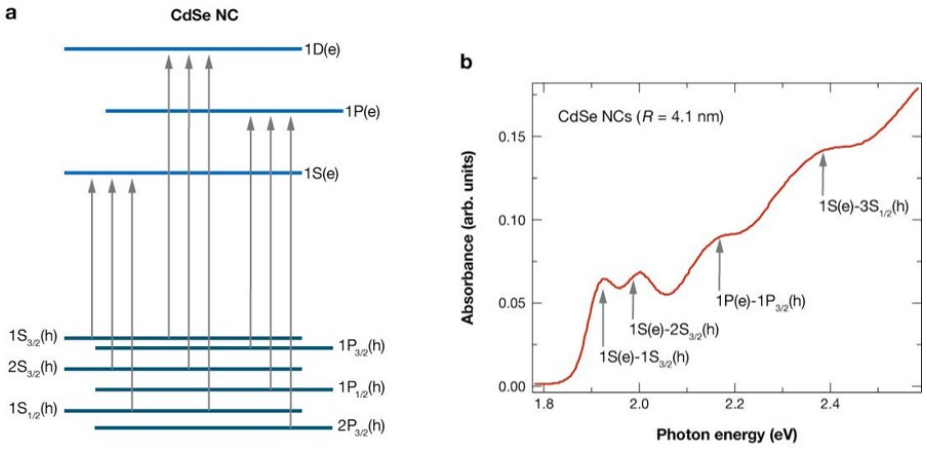

FIGURE 3.2: Electronic energy level spectrum for CdSe nanocrystals. a) Electronic energy levels in the conduction and the valence bands. Confinement induced mixing between the valence band states leads to a complex valance band structure. b) The ground-state absorption spectrum for CdSe with a radius of $R = 4.1$ nm showing the four lowest transitions. Reproduced from reference [124] with permission.

The exchange interaction is directly proportional to the electron and the hole wavefunction overlap, and is thus greatly enhanced in NCs compared to the bulk material. In this case, the band-edge electron ($1S(e)$) and the hole states ($1S_{\frac{3}{2}}$) cannot be treated independently but as a combined state with total angular momentum $N = F_e + F_h$, where $F_e = \frac{1}{2}$ and $F_h = \frac{3}{2}$ are electron and the hole total angular momentum. Thus, N can take the value of either 1 or 2. The exchange interaction lifts the degeneracy of these states forming a higher energy bright state ($N = 1$) and a low energy dark state ($N = 2$), as shown in figure 3.3a. These states are further split by into five sub-levels due to the crystal field and the shape asymmetry, forming the upper states (U) and lower (L) states. The labelling of these states is according to the magnitude of the projection of the total angular momentum, $|N_m|$, along the unique crystal axis. The lowest energy level ($|N_m| = 2$) remains optically dark and is separated by the next lower bright level, $|N_m| = 1^{\mathrm{L}}$, by several meV (ΔE), depending on the NC size. This forms the basis of the dark-bright exciton model[128, 129], shown in figure 3.3b, and which used to explain the decrease of the radiative lifetime from 1 μs at liquid He temperatures to several 10s of ns at room temperature[130]. This can be explained as follows. At lower temperature the exciton recombination occurs via the optically forbidden low energy dark state leading to long radiative lifetimes. At higher temperatures the thermal redistribution of the exciton population mixes the dark state with the higher bright states with a higher oscillator strength, leading to a shorter radiative lifetime.

The dark-bright splitting (ΔE) in addition to the higher level states in the fine structure (0^{U} and 1^{U}) contribute to the Stokes shift between the ensemble PL peak and the lowest absorption maximum as seen in figure 3.4.

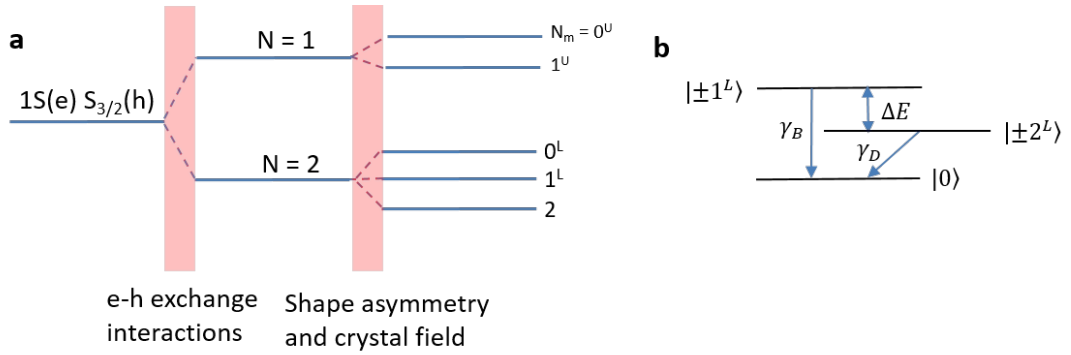

FIGURE 3.3: CdSe fine structure and the dark-bright exciton model a) A schematic of the ground states exciton fine structure resulting from the exchange interaction, the NC shape asymmetry and the crystal field. b) The dark-bright exciton splitting. The radiative rate from the dark and the bright state is γ_D and γ_B, respectively and ΔE is the energy splitting.

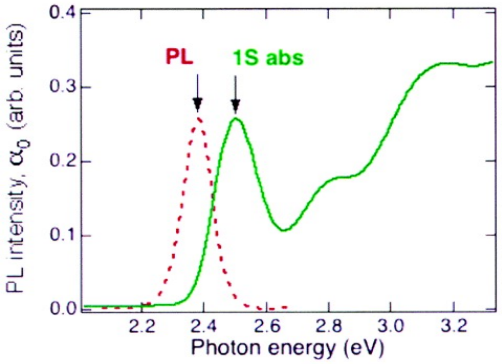

FIGURE 3.4: Band-edge emission and Absorbance. PL emission (red dashed line) and absorbance spectra (green solid line) for CdSe NCs with R = 1.2 nm. Reproduced from reference [77] with permission.

3.3.2 Nanoplatelets

Whereas the carriers inside NCs experience a spherical confinement potential, carriers in NPs experience confinement in only in one direction. The separation between the k-states within each plane is given by $\Delta k_{\mathrm{x,y,z}} = \frac{\pi}{L_{x,y,z}}$, where $L_{x,y,z}$ is the size of the nanoplatelet in the x, y or the z-direction. If the confinement is assumed to be in the z-direction energy levels then the separation between the energy states will be a lot larger in the z-direction than in the other two and for this reason the energy levels can be visualised in k-space as a series of planes, each associated with a quantum number n_z, as shown in figure 3.5a in the case of $n_z = 1$. The dispersion relation then consists of a series of bands each with a different n_z and each accommodating many carriers at energies very close to one another[16], as shown in figure 3.5b for the first two quantum numbers. Like in the case of NCs the spin-orbit interaction splits each of the valence bands into the hh, lh and so bands[131] and this is reflected in the measured absorption

spectrum shown in figure 3.5c. A Stokes shift between the hh absorption maximum and the ensemble PL peak is also shown in figure 3.5c and can be explained in terms of the exciton fine structure in a similar manner to the NCs[132].

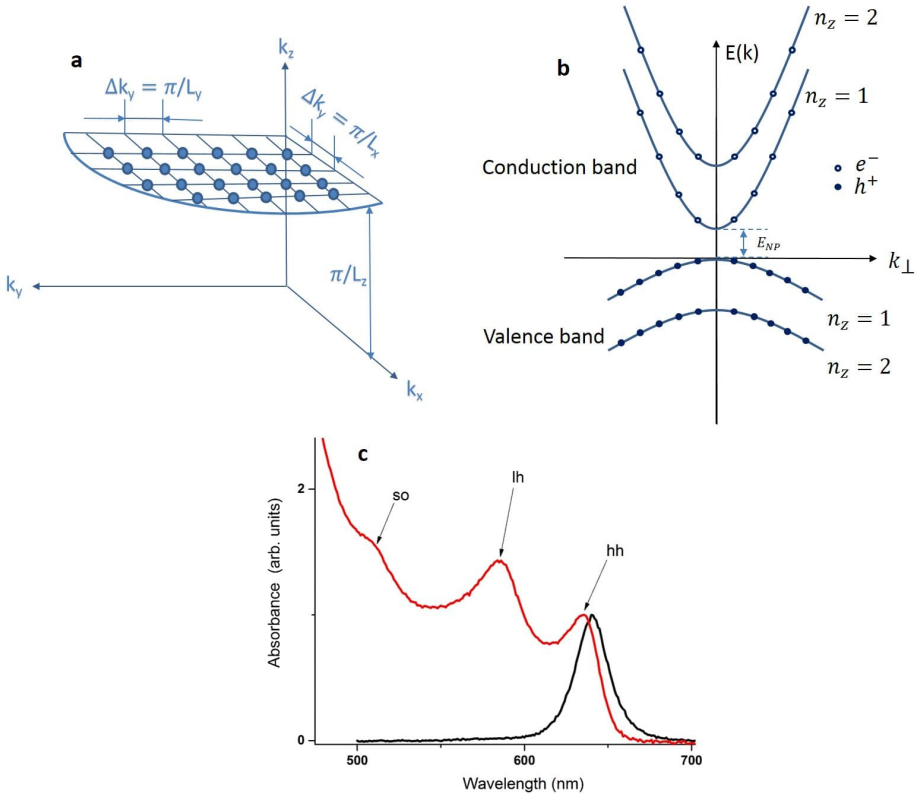

FIGURE 3.5: Energy level structure of Nanoplatelets. a) Representation of the energy states in k-space for $n_z = 1$. b) Dispersion relations for the $n_z = 1, 2$ sub-bands with the energy gap E_{NC}. The splitting due to the spin-orbit interaction is not shown. c) The absorption spectrum of CdSe NPs showing the hh, lh and the so bands overlaid on top of the ensemble PL curve.

3.4 Optical Gain and Lasing in Colloidal Quantum Dots

3.4.1 Condition for Optical Gain in Colloidal Quantum Dots

In this section the condition for optical gain for type-I and type-II CQDs is derived in terms of the average exciton number required at threshold. The model presented here takes into account effects of exciton-exciton interactions as well as the degeneracies associated with the band-edge state, and follows exactly the treatment detailed by Nanda and co-workers[133].

Consider an ensemble of CQDs for which the fraction of the unexcited CQDs (those that contain no excitons) is given by n_0. Then the fraction that are excited is given, $n_x = 1 - n_0$, and with the assumption that all these only contain a single exciton, we

have $n_x = \langle N \rangle_{\text{eh}}$, where $\langle N \rangle_{\text{eh}}$ is the average exciton number per CQD. The absorption cross-section of a single unexcited CQD, ${\sigma_{11}}^0(\omega)$, at the photon energy $\hbar\omega$ is assumed to have a Lorentzian profile:

$$ {\sigma_{11}}^0(\omega) = A \frac{\gamma {\Gamma_{11}}^2}{(\hbar\omega - \hbar\omega_{11})^2 + {\Gamma_{11}}^2} \tag{3.5} $$

where $A = 4\pi\omega\langle|d_{11}|^2\rangle(nc\Gamma_{11})^{-1}$, in which $\langle|d_{11}|^2\rangle$ is the square of the transition dipole matrix element averaged over all NC orientations, n is the refractive index, c is the speed of light, $\hbar$ is the reduced Planck's constant, γ is the degeneracy of the emitting state, $\hbar\omega_{11}$ and Γ_{11} are emission energy and the homogenous linewidth of the transition.

For a CQD containing a single exciton the absorption cross-section, ${\sigma_{11}}^{\text{X}}(\omega)$, in the presence of exciton-exciton interaction energy, Δ_{XX}, is then given by:

$$ {\sigma_{11}}^{\text{X}}(\omega) = A \frac{(\gamma - 1){\Gamma_{11}}^2}{(\hbar\omega - \hbar\omega_{11} - \Delta_{XX})^2 + {\Gamma_{11}}^2} \tag{3.6} $$

and the stimulated emission cross-section as:

$$ {\sigma_{11}}^{\text{SE}}(\omega) = -A \frac{{\Gamma_{11}}^2}{(\hbar\omega - \hbar\omega_{11})^2 + {\Gamma_{11}}^2} \tag{3.7} $$

Note that the factor $\gamma - 1$ in equation 3.6 marks a reduction the in absorption cross-section of the CQD due to state filling of the first excited state by a single exciton. Using these quantities the absorption coefficient, $\alpha_{11}(\omega)$, at the transition energy of the ensemble can be determined. However, in order to do so the CQD size poly-dispersity (inhomogeneous broadening) needs to be taken into account. This takes the form of a Gaussian function given by $g(\omega_{11}) = (\sqrt{\pi}\Gamma)^{-1} exp(\frac{-(\hbar\omega_{11} - \hbar\omega_0)^2}{\Gamma^2})$. Here ω_0 is central transition frequency of the CQD ensemble and Γ is the inhomogeneous linewidth. Then integrating over central frequency of each of the individual CQDs in the ensemble (ω_{11}) leads to the following expression for $\alpha_{11}(\omega)$:

$$ \alpha_{11}((\omega) = n_{CQD} \int_0^\infty [(1 - n_x){\sigma_{11}}^0 + n_x({\sigma_{11}}^{\text{X}} + {\sigma_{11}}^{\text{SE}}) g(\omega_{11})\, \mathrm{d}\omega_{11} \tag{3.8} $$

where n_{CQD} is the concentration. Under the assumption that homogenous broadening is much smaller than the inhomogeneous broadening equations 3.5-3.7 can be approximated by a δ function: $\Gamma_{11}\pi^{-1}(x^2 + {\Gamma_{11}}^2)^{-1} \sim \delta(x)$. Using this assumption the expression for the absorption coefficient becomes:

$$\alpha_{11}(\omega) = \frac{n_{CQD} A\sqrt{\pi}\Gamma_{11}}{\Gamma} exp\left(\frac{-\Delta^2}{\Gamma^2}\right) \times \left[\gamma - (\gamma+1)n_x + (\gamma-1)n_x exp\left(-\frac{{\Delta_{XX}}^2}{\Gamma^2}\right) exp\left(\frac{2\Delta\Delta_{XX}}{\Gamma^2}\right)\right] \tag{3.9}$$

where $\Delta = \hbar(\omega - \omega_0)$. Optical gain occurs when $\alpha_{11}(\omega)$ <0 so the threshold at ω is given by the condition $\alpha_{11}(\omega) = 0$. By setting $\omega = \omega_0$ i.e. $\Delta = 0$ in equation 3.9 yields an equation for the gain threshold in terms of the average exciton number per CQD, $\langle N\rangle_{\text{th}}$:

$$\langle N\rangle_{\text{th}} = \frac{\gamma}{\gamma + 1 - (\gamma-1)exp\left(-\frac{{\Delta_{XX}}^2}{\Gamma^2}\right)} \tag{3.10}$$

It should be noted that in this model both the electron and hole band-edge states are assumed to have the same degeneracy (γ). In this case of CdSe the degeneracy of the band-edge state electron state is two, but is more than two for the hole state due to the complex multi-subband structure of the valence band. However, for CdSe this degeneracy is reduced to two in the presence of exchange interactions, shape asymmetry and the crystal field. In the case of type-I CQDs, the exciton-exciton interaction energy is very small in comparison to the inhomogeneous linewidth ($\Delta_{XX} \ll \Gamma$) and in this case the factor $exp\left(-\frac{{\Delta_{XX}}^2}{\Gamma^2}\right) \sim 1$ and equation 5.21 is reduced to $\langle N\rangle_{\text{th}} \sim \frac{\gamma}{2}$. Since for CdSe $\gamma = 2$, this gives $\langle N\rangle_{\text{th}} \sim 1$. Poisson averaging over the ensemble increases this value to $\langle N\rangle_{\text{th}} \sim 1.15$[134]. In another words, optical gain requires at least one exciton on average per CQD. Intuitively, this makes sense since if $\gamma = 2$, an incoming photon has an equal probability of being absorbed or to stimulate emission of another photon in a CQD containing a single exciton i.e. zero net gain. Thus to obtain non-zero optical gain in type -I CQD requires the CQDs on average containing more than a single exciton i.e. biexcitons.

For type-II CQDs the opposite limit is true where the exciton-exciton interaction energy is much larger than the inhomogeneous linewidth ($\Delta_{XX} \gg \Gamma$). In this case the factor $exp\left(-\frac{{\Delta_{XX}}^2}{\Gamma^2}\right) \sim 0$ and equation 5.21 is reduced to $\langle N\rangle_{\text{th}} \sim \frac{\gamma}{\gamma+1}$ and for $\gamma = 2$ this gives $\langle N\rangle_{\text{th}} \sim \frac{2}{3}$. In other words, if the interaction energy is large enough the absorption of a second incoming photon at the emission energy is inhibited in a CQD containing a single exciton and only stimulated emission can occur and, thus lasing in the single exciton regime can be made possible. Giant exciton-exciton interactions energies can be created by spatially separating the electron and hole wavefunctions to create an internal electric field, which induces a Stark-effect[38]. This effect was used by Grivas *et al*[115] to achieved lasing in the single exciton regime using CdSe/CdS core-shell dot-in-rod structures

Whilst the above argument for the number of excitons at threshold certainly hold for the spherical CQDs the gain condition for NPs need to be considered a bit more carefully. This is because many carriers of the same emission energy can occupy a single NP[69, 135] whereas at most only two can be accommodated in the band-edge state of NCs. In this case the threshold condition defined above may not be applicable to NPs as several carriers (i.e. more than two) per NP may be required to achieve population inversion, like in the case of epitaxial quantum wells[136]. On the other hand, the works of several authors have experimentally hinted at the biexcitonic nature of optical gain in NPs[97, 137], consistent with what is found for NCs. However, to the best of my knowledge, no thorough experimental or theoretical investigation has been found that clearly demonstrate the condition for optical gain in NPs.

3.4.2 Condition for Lasing

As mentioned in section 3.4.1 optical gain requires population inversion. However, true lasing action can only be achieved by using a laser oscillator, in which the gain medium is enclosed by an optical cavity (see section 3.5 for more details). The purpose of an optical cavity is to:

1. Allow the build up of light intensity by repeated reflections of the photons through the medium, even if the gain is small.
2. Provide monochromaticity of the beam since laser oscillation is restricted to one (or more) of the optical modes of the cavity. This is due to the fact that the spectral width of the cavity mode can be a lot narrower than the linewidth of the transition.
3. Provide highly directional emission since only the photons propagating orthogonal to the mirrors are sustained and amplified inside the cavity.

At the lasing threshold of the increase the beam intensity is balanced exactly by the losses due to the imperfect reflectivity of the mirrors, as well as diffraction losses and other losses due to the active medium such as self-absorption and scattering. In this case, on following the path of the beam through a round trip of the cavity the threshold condition can be defined as [138]:

$$R_1 R_2 e^{2(g_{th}-\mathcal{L})L} = 1 \tag{3.11}$$

where R_1 and R_2 are the mirror reflectivities and L is the cavity length, g_{th} is the gain (per unit length) at threshold, which is proportional to the population inversion and $\mathcal{L}$ accounts for all other the losses (per unit length) mentioned previously. The factor of two in the exponential is due to the fact that light passes the length of the cavity twice per round trip.

In equation 3.11 we assume that the population inversion remains constant as the beam of light propagates through the medium at or above threshold. However, this is never strictly true since the laser beam derives its energy from the stimulated emission and this will deplete the initial population inversion created just after the pumping process. The reduction in the gain due to the stimulated emission process is known as gain saturation. Thus, g_{th} in equation 3.11 is the unsaturated gain coefficient and should be replaced by the saturated gain at threshold (g_{sat}). This process is shown in figure 3.6. In figure 3.6a it can be seen that below threshold (P_{th}) the (unsaturated) gain is proportional to the pumping power as the number of photons emitted by stimulated emission remain close to zero (figure 3.6b) and no stimulated emission takes place. As the gain approaches the total losses ($\mathcal{L}$) in the system (satisfying equation 3.11), laser oscillation can take place which results in a significant increase the number of lasing photons in the system, depleting the population inversion and locking the gain to the saturated value of g_{sat}. When the pumping power is increased beyond the threshold value the output intensity also increases (as this is proportional to the initial population inversion i.e. the unsaturation gain) but the gain will quickly reach the saturated threshold value of g_{sat} due to burning of the population inversion. Thus, the gain is clamped at this value for all pumping powers at or above threshold allowing equation 3.11 to be always satisfied.

Moreover, the efficiency (η) of the lasing process may be quantified by taking the slope (called the slope efficiency or the differential gain) of the graph in figure 3.6b:

$$\eta = \frac{dI}{dP} \tag{3.12}$$

One of the defining characteristics of the laser is a decrease in the spectral linewidth ($\Delta\omega$) of the lasing mode with pumping power. This makes sense intuitively since, assuming the line shape of the optical mode is Lorentzian (see section 3.5), the spectral intensities of the frequencies close to the peak frequency will grow (via stimulated emission) faster than those at the wings of the function. In fact, it can be shown that the linewidth above threshold is inversely proportional to the average number of photons (ϕ) inside the cavity[138]:

$$\Delta\omega = \frac{R_{sp}}{2\phi} \tag{3.13}$$

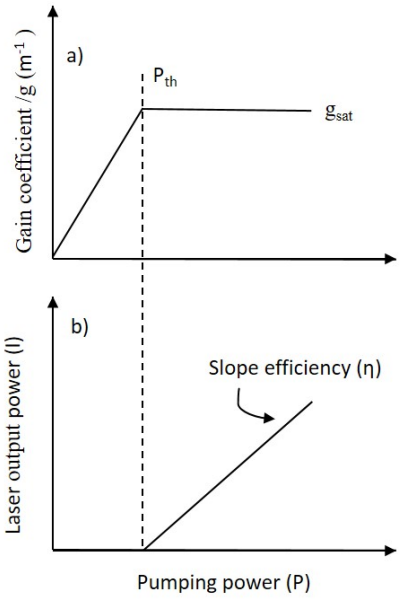

FIGURE 3.6: Variation of emission intensity and gain below and above threshold. a) Idealised variation of gain as a function of pumping power. b) Idealised variation of the output intensity as a function of pumping power.

where R_{sp} is the spontaneous emission rate of the emitter. Under steady-state conditions (i.e. satisfying equation 3.11) the photons lost through the cavity mirrors and other losses are replaced by both stimulated and spontaneous emission. Although the photons arising from stimulated emission are perfectly coherent (with the same frequency and phase) with those that initially stimulate emission, those that are emitted by spontaneous emission will have a random phase, which will lead to the diffusion of the overall phase of the oscillating mode (note that the amplitude of the mode is not significantly affected as the number of spontaneously emitted photons is much lower than those emitter by stimulated emission above threshold). Thus, for a particular pumping power, the noise introduced by spontaneous emission places a fundamental lower limit (so-called then Schawlow-Townes limit) to the linewidth of the lasing mode. In reality, however, additional factors such as self-absorption, scattering of the laser photons etc. will increase the linewidth above this limit.

3.5 Optical Microcavities

This section introduces the hemispherical cavities used to conduct the lasing experiments in this thesis. The primary advantage of these cavities is that they offer in-situ tunability providing a convenient method to perform gain spectroscopy experiments. From a technological standpoint, tunable lasing can be achieved with these cavities and

the hemispherical shape provides a low beam divergence, and due to their small size, the possibility of on-chip integration.

3.5.1 Fabry-Pérot Cavity

The simplest case of a cavity is a planar (or a Fabry-Pérot) cavity with two opposing mirrors with reflectivity R_1 and R_2 and optical cavity length, L_{opt}, as shown in figure 3.7a. The finesse (F) is one of the key parameters that determine the properties of cavities and can be intuitively thought of as the number of round trips a photon will make before decaying out of the cavity[120]:

$$F = \frac{\pi(R_1 R_2)^{1/4}}{1 - \sqrt{R_1 R_2}} \tag{3.14}$$

On resonance the cavity length L_{opt} is equal to an integer number of half wavelengths:

$$L_{opt} = \frac{q\lambda}{2} \tag{3.15}$$

where q is equal to the number of antinodes between the two mirrors. Wavelengths which satisfy the equation 3.15 produce peaks (optical modes) in the cavity transmission spectrum at their respective spectral position as shown in figure 3.7b. Since in reality the mirror reflectivities are less than unity ($1 > R_1,\ R_2$) the photons inside the cavity will decay at an exponential rate, the Fourier transform of which produces modes in the spectral domain with a Lorentzian line shape with a finite spectral linewidth, δv (in Hz). The linewidth is related to the photon decay rate (κ) by, $\kappa = 1/\tau_{cav} = 2\pi\delta v$, for which τ_{cav} is the cavity decay time.

Moreover, the spectrum shown in figure 3.7b can be used to calculate the cavity length. This is done by rearranging equation 3.15 and differentiating with respect to the wavelength:

$$\frac{dq}{d\lambda} = -\frac{2L_{opt}}{\lambda^2} \tag{3.16}$$

Here $d\lambda = \Delta\lambda$ can be taken as the spectral difference between two adjacent modes (i.e. $\Delta q = 1$), also known as the free spectral range (FSR). Then equation 3.16 yields cavity length equal to:

$$L_{opt} = \frac{\lambda^2}{2\Delta\lambda} \tag{3.17}$$

A general figure of merit that can be used to describe cavity of any geometry is the Q-factor:

$$Q = \frac{\lambda}{\delta\lambda} \tag{3.18}$$

where $\delta\lambda$ is the cavity linewidth (refer to figure 3.7b). The Q-factor is proportional to the amount of time a photon spends inside the cavity and can be intuitively thought of as the number of oscillations a photon makes inside the cavity before decaying. It is related to the finesse by the following:

$$Q = qF \tag{3.19}$$

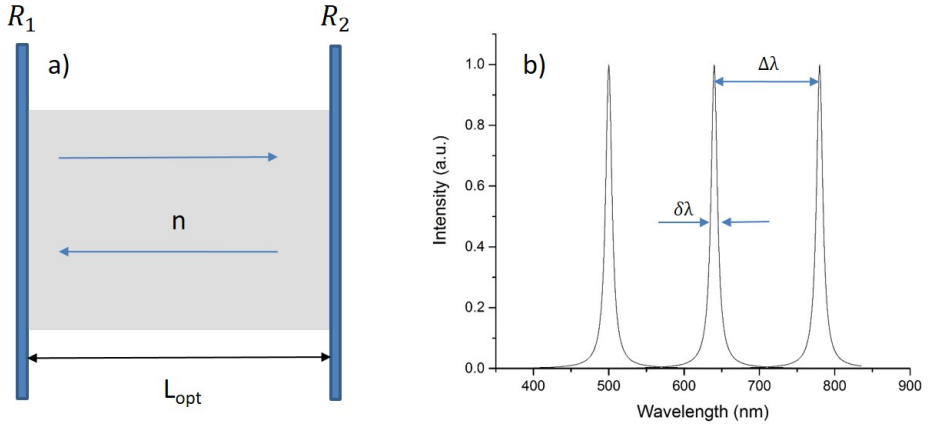

FIGURE 3.7: Fabry-Perot Cavity. a) A schematic of the Fabry-Perot cavity with length L filled with an active medium of refractive index n. b) The optical modes (normalised intensity) of the cavity with FWHM ($\delta\lambda$) and the FSR ($\Delta\lambda$).

3.5.2 Distributed Bragg Reflectors

In order to achieve high finesses it is necessary to confine the resonant photons inside the cavity as efficiently as possible. One way of doing this is by using metallic mirrors to reflect light, however, the reflectivity for such mirrors generally cannot exceed more than 95% because of the losses induced when the electric field interacts with the electrons in the metal. Although evaporated silver mirrors have been shown to achieve higher reflectivities[139] a higher degree of photon confinement can be achieved by using dielectric mirrors, like the ones used in this thesis. These comprise of a stack of alternating high and low index materials known as Distributed Bragg Reflector (DBR). The thickness of the alternating layers are chosen to be equal to $\frac{\lambda}{4n}$, where λ is the desired wavelength and n is the refractive index of the layer material. The layer thicknesses are

such that the path length differences between all reflections from low-index layers (i.e when light traveling through a high index material encounters an interface with a low index material) are always integer multiples of wavelength. Reflections from high index layers (i.e when light traveling through a low index material encounters an interface with a high index material) have exactly half a wavelength path difference, but there is a π-phase shift upon reflection meaning all of the reflected rays from the interfaces will be in phase.

The reflection and the transmission amplitude coefficients of light at the boundary between two materials are described by the Fresnel equations[140]. However, modelling multi-layered structures such as the DBR becomes increasingly complex as it needs to take into account multiple reflections and interference effects within the layers. A convenient way to model such layers is the transfer matrix method and a full description of this method can be found in Hecht[140]. In this method, the electric and the magnetic fields either side of the dielectric layer can be related by a matrix. This matrix can then be generalised to an arbitrary number of interfaces and, thus, can be used to calculate the reflectivities of the DBRs.

Figure 3.8 shows the reflectivity spectrum calculated using the transfer matrix model for a DBR consisting of 20 pairs on alternating dielectric layers with the low and high refractive index of $n_L = 1.4$ and $n_H = 2.1$, respectively. It can be seen that the reflectivity is almost unity for the wavelength range of $\sim$ 570-730 nm, which is known as the stop-band.

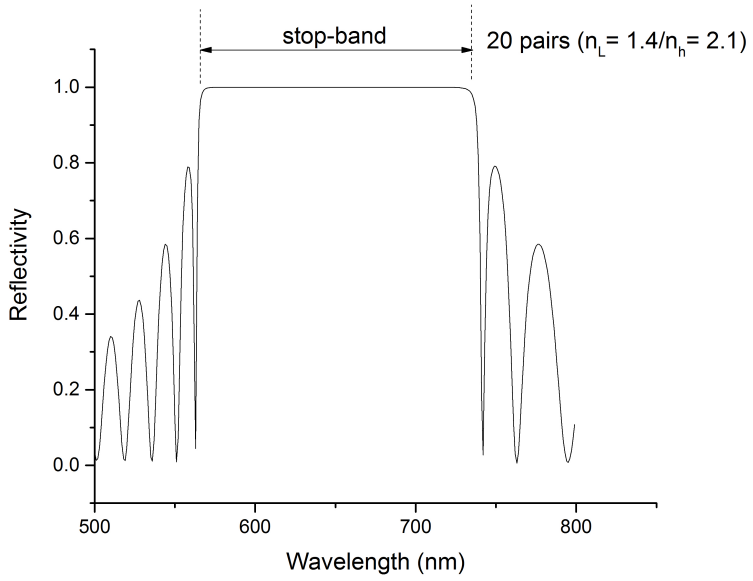

FIGURE 3.8: Typical reflectivity spectrum of a DBR.

A notable feature of the such mirrors is the penetration of the electric field into the DBR stack, known as the penetration depth, L_{DBR}. This depth depends on whether the terminating layer on the air-mirror (the space in between the two DBR stacks) is of low or high refractive index. For a high terminating layer this is given by[141]:

$$L_{DBR,H} = \frac{\lambda n}{4 n_{av} \Delta n} \tag{3.20}$$

and a for low terminating layer

$$L_{DBR,L} = \frac{\lambda n_{av}}{4 n \Delta n} + \frac{\lambda \Delta n}{2\pi^2 n n_{av}} \tag{3.21}$$

where $\Delta n = n_H - n_L$ and $n_{av}^{-1} = 2(n_H^{-1} + n_L^{-1})$. Thus, the total penetration depth of the cavity is $L_{DBR} = L_{DBR,1} + L_{DBR,2}$ where $L_{DBR,1}$ and $L_{DBR,2}$ are the penetration depths of the two mirrors. In this case, the total physical cavity length (L) is the sum of the physical separation between the mirrors (L_c) and the total penetration depth:

$$L = L_c + L_{DBR} \tag{3.22}$$

the optical cavity length is:

$$L_{opt} = n L_c + n_{av} L_{DBR} \tag{3.23}$$

3.5.3 The Gaussian Beam

In this section the expression for the Gaussian beam will be derived which describe the spatial distribution of the modes formed by the open access hemispherical cavities. Few details about other higher order modes associated with the cavities, known as Hermite-Gaussian modes, will also be detailed. A more complete derivation can be found in references[142] and [143]. The description starts with the Helmholtz equation describing the propagation of the spatial part of the electric field, $\mathcal{E}(\mathbf{r})$, in the absence of any charges or currents:

$$(\nabla^2 + k^2)\mathcal{E}(\mathbf{r}) = 0 \tag{3.24}$$

where k is the wavevector and $\nabla = \frac{\partial^2}{\partial x^2} + \frac{\partial^2}{\partial y^2} + \frac{\partial^2}{\partial z^2}$ is the Laplacian operator. Equation 3.24 has a solution of the form:

$$\mathcal{E}(\mathbf{r}) = U(\mathbf{r})e^{-ikz} \tag{3.25}$$

where $U(\mathbf{r})$ is the complex amplitude. The Helmholtz equation can be simplified by imposing the condition that the angle of divergence of the light (θ) from the direction of propagation is small (the paraxial approximation), or in another words $U(\mathbf{r})$ in equation 3.25 is a slowly varying function along the z-direction (i.e. $\frac{\partial^2 U}{\partial z^2} \ll k\frac{\partial U}{\partial z} \ll k^2 U$). With this assumption and by substituting equation 3.25 into 3.24 results in the paraxial Helmholtz equation:

$$\nabla_T^2 - 2ik\frac{\partial U}{\partial z} = 0 \tag{3.26}$$

where $\nabla_T^2 = \frac{\partial^2}{\partial x^2} + \frac{\partial^2}{\partial y^2}$ is the transverse Laplacian operator. The solution to equation 3.26 describes the Gaussian beam shape and has the following form:

$$\mathcal{E}(\mathbf{r}) = U_0\frac{\omega_0}{\omega(z)}e^{-\frac{r^2}{\omega(z)^2}}e^{-ikz}e^{-ik\frac{r^2}{2\beta(z)}}e^{i\zeta(z)} \tag{3.27}$$

where $r = \sqrt{x^2+y^2}$, $\omega(z)$ is identified as the 1/e radius of the beam at z, which is the propagation direction, as shown in figure 3.9. ω_0 and U_0 are the radius of the beam and the amplitude at $z = 0$, i.e. located at surface of the planar mirror (M_1 in figure 3.9). $\beta(z)$ and $\zeta(z)$ are the RoC of the phase profile and the Gouy phase shift, respectively. Hence, the first exponential term in equation 3.27 gives the Gaussian mode profile, the radial extent of which is determined by $\omega(z)$. The second term makes the wave propagate in the positive z-direction (provided k is positive). The third term gives information about the RoC of the wavefronts along the z-direction. Finally, the fourth exponential term contains the Gouy phase factor and plays a major role in determining the resonant frequencies of the cavities.

Moreover, the beam waist, RoC and the Gouy phase shift can be conveniently expressed in terms of the Rayleigh range, z_R, which is the distance along the z-axis at which the beam radius is equal to $\sqrt{2}\omega_0$ (refer to figure 3.9):

$$z_R = \frac{\pi w_0^2}{\lambda} \tag{3.28}$$

$$\omega(z) = \omega_0\left(1 + \left(\frac{z}{z_R}\right)^2\right)^{1/2} \tag{3.29}$$

$$\beta(z) = z + \frac{z_R^2}{z} \tag{3.30}$$

$$\zeta(z) = tan^{-1}\left(\frac{z}{z_R}\right) \tag{3.31}$$

For a more general case were both mirrors have a finite RoC the minimum mode waist (ω_0) at each of the mirrors (ω_1, ω_2) can be defined using the parameter g_i:

$$g_i = 1 - L_{geo}/R_i \tag{3.32}$$

where $L_{geo} = nL_c$ is defined as the geometrical cavity length for which n is the refractive index of the medium and R_i is the RoC of each mirror (i.e. $i = 1, 2$). Using this the beam the radius of the beam can be defined by the following set of equations:

$$\omega_0 = \left(\frac{\lambda L_{opt}}{\pi}\right)^{1/2}\left(\frac{g_1 g_2(1 - g_1 g_2)}{(g_1 + g_2 - 2g_1 g_2)^2}\right)^{1/4} \tag{3.33}$$

$$\omega_1 = \left(\frac{\lambda L_{opt}}{\pi}\right)^{1/2}\left(\frac{g_2}{g_1(1 - g_1 g_2)}\right)^{1/4} \tag{3.34}$$

$$\omega_2 = \left(\frac{\lambda L_{opt}}{\pi}\right)^{1/2}\left(\frac{g_1}{g_2(1 - g_1 g_2)}\right)^{1/4} \tag{3.35}$$

Since the RoC of mirror one used in this thesis is infinite then $g_1 = 1$ and it can be seen from equation 3.33 and 3.34 that $\omega_1 = \omega_0$. It can also be seen from equation 3.33 that in order to produce a positive value for ω_0 the numerator needs to satisfy the following condition:

$$0 \leq g_1 g_2 \leq 1 \tag{3.36}$$

which is the criterion for resonator stability. In other words, in order to effectively confine the modes inside the open cavity the cavity length needs to be smaller than the RoC of the hemispherical mirror (i.e $L_{geo} \leq R_2$). Furthermore, in order avoid diffraction losses it is also necessary for the diameter of the hemispherical mirror to be substantially larger than the beam waist that appears at its surface[144].

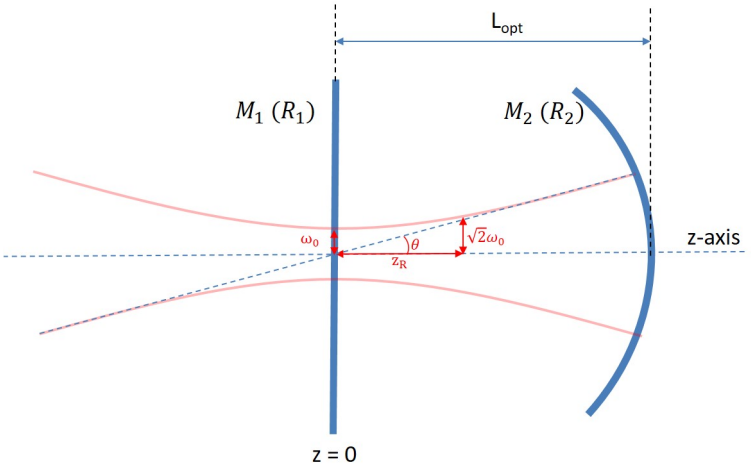

FIGURE 3.9: Schematic the Gaussian beam in a cavity of optical length L_{opt}. ω_0 is the mode waist located at the planar mirror and z_R is the Rayleigh range. The angle of divergence of the beam is θ. The two mirrors, M_1 and M_2, have RoC R_1 and R_2, respectively.

3.5.4 The Hermite-Gaussian Beam

Equation 3.27 in section 3.5.3 describes only the lowest-order Gaussian beam that can be produced by a cavity such as the one shown in figure 3.9. In other words, there exists other, higher-order modes which are also solutions to the paraxial Helmholtz equation, namely the Hermite-Gaussian beam, which has the following general form:

$$\mathcal{E}_{l,m}(\mathbf{r}) = U_0 \frac{\omega_0}{\omega(z)} H_l\left[\sqrt{2}\frac{x}{\omega(z)}\right] H_m\left[\sqrt{2}\frac{y}{\omega(z)}\right] e^{-\frac{r^2}{\omega(z)^2}} e^{-ikz} e^{-ik\frac{r^2}{2\beta(z)}} e^{i(l+m+1)\zeta(z)} \quad (3.37)$$

It can be seen that this more general solution contains the lowest-order solution as well two additional factors, $H_l\left[\sqrt{2}\frac{x}{\omega(z)}\right]$ and $H_m\left[\sqrt{2}\frac{y}{\omega(z)}\right]$, which are the Hermite polynomials and where the integers l and m denote their order. Thus, the modes of the cavity have an additional transverse mode structure in addition to the Gaussian shape discussed in the section3.5.3 and also acquire and additional phase shift of $e^{i(l+m)\zeta(z)}$. Each of the modes in equation 3.37 is referred to as $\mathrm{TEM_{lm}}$, which stands for "transverse electric and magnetic field."

The electric field intensity distribution located on the planar mirror on an area of 6×6 μm is shown in figure 3.10a as well as the corresponding spectrum in figure 3.10b for the first four Hermite-Gauss modes. The lowest-order mode ($\mathrm{TEM_{00}}$), also known as the fundamental mode, is non-degenerate. Higher-order modes, while having different spatial profiles are energetically degenerate for a perfectly symmetrical cavity. It is important to note that compared to the Fabry-Pérot cavity in section 3.5.1 the distribution of the

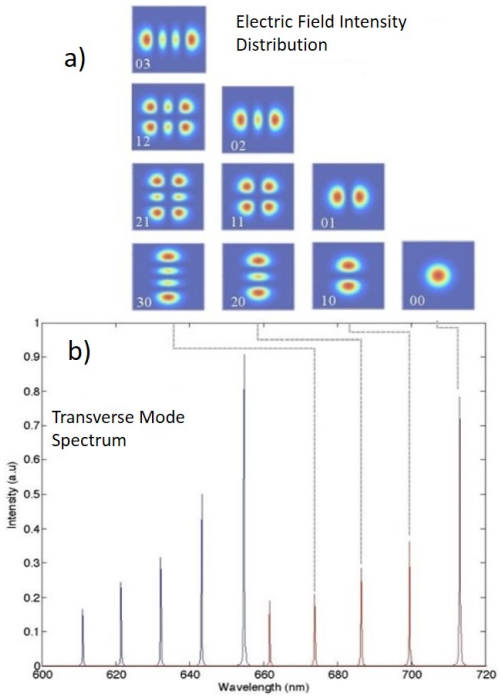

FIGURE 3.10: Schematic of the Hermite-Gaussian electric field distribution and mode spectra. a) The electric field distribution of the first four modes (i.e up to $TEM_{l+m=3}$) of the hemispherical cavities located on the surface of the planar mirror. Higher order modes with the same $l+m$ are energetically degenerate but spatially distinct. b) The mode spectrum showing two $TEM_{l+m=0}$ modes and the first four transverse modes associated with this mode. All the simulations were done using MATLAB. Images Courtesy of Sam Johnson.

mode frequency is modified by the hemispherical mirror. This means that the simple formula used to calculate the mode frequency using equation 3.15 can be used only as an approximate. Instead the formula used to calculate the mode frequencies, v_{qlm}, is now given by the following equation:

$$v_{qlm} = \frac{c}{2L_{opt}}\left(q + \frac{1}{\pi}(l+m+1)cos^{-1}\sqrt{g_1 g_2}\right) \tag{3.38}$$

where q is the order of the TEM_{00} mode.

Finally, by integrating the electric field given in equation 3.37 an expression for the optical cavity mode volume, V_{opt}, can be obtained[145]:

$$V_{opt} = \frac{\pi\omega_0^2 L_{opt}}{4} \tag{3.39}$$

3.6 Cavity Quantum Electrodynamics

The open access cavity described forms an essential component for producing lasing from CQDs. Cavity quantum electrodynamics (CQED) provides the theoretical basis for the interaction between the CQDs and the cavity. A non-zero vacuum electric field arises from the quantum treatment of the electromagnetic field and permeates all space and can be modified quite significantly in the presence of the cavity. If the coupling between the cavity and the emitter inside the cavity is stronger than the cavity photon decay rate and the total emitter decay rate, then system is said to enter the strong coupling regime. However, lasing occurs in the weak coupling regime, where the cavity or the emitter decay rates exceeds the coupling rate. Since in this regime the effect of the cavity is small, perturbation theory can be used describe the emitter-cavity interaction. The effect of the cavity in this regime then is to modify the emitter emission rate compared to free space. The transition rate, R, for spontaneous emission is given by the well-known Fermi's golden rule[120]:

$$R = \frac{2\pi}{\hbar^2}|M_{12}|^2 g(\omega) \tag{3.40}$$

where $g(\omega)$ is the optical DOS. M_{12} is the transition matrix element and is given by:

$$|M_{12}|^2 = \frac{1}{3}{\mu_{12}}^2{\mathcal{E}_{vac}}^2 = \frac{{\mu_{12}}^2\hbar\omega}{6\epsilon_0 V} \tag{3.41}$$

where $\mu_{12} = -e\langle 1|\mathbf{r}|2\rangle$ is the electric dipole matrix element for the initial (1) and the final (2) states and for which $\mathbf{p} = -e\mathbf{r}$ is the electric dipole, V is the modal volume and ϵ_0 is the vacuum permittivity. The factor $\frac{1}{3}$ comes from the averaging over all possible dipole orientations with respect to the vacuum electric field. As can be seen from equation 3.40 calculation of the transition rate requires the optical DOS. An optical cavity significantly modifies the DOS compared to free space and therefore also the emission rate of the emitter into the cavity. The ratio of the emission into the cavity to that of free space is known as the Purcell factor and the expression for this, which requires the optical DOS, is the subject of section 3.6.1.

3.6.1 Optical Density of States and the Purcell Factor

As can be seen from equation 3.40 the calculation of the emission rate, R, requires the derivation of the optical DOS in 3-D (i.e. in free space or in a cavity). In this section the optical DOS of the free space are compared to those inside the cavity, which will

eventually yield an expression for the Purcell factor. Full details of the derivation of these expressions are found in the book by Mark Fox[120]. The DOS in free space per unit volume is quadratic with respect to the angular frequency, ω:

$$g^{3D}(\omega) = \frac{\omega^2}{\pi^2 c^3} \tag{3.42}$$

The DOS in a cavity, $g(\omega)_{cav}$, of mode volume V is assumed to be a normalised Lorentzian with a central frequency, ω_c:

$$g(\omega)_{cav} = \frac{2}{\pi \Delta\omega_c} \frac{{\Delta\omega_c}^2}{4(\omega_0 - \omega_c)^2 + {\Delta\omega_c}^2} \tag{3.43}$$

where equation 3.43 is evaluated at the transition frequency of the emitter (ω_0) and $\Delta\omega_c$ is the FWHM, which is also equivalent to the cavity decay rate, κ. The emission rate into the cavity, R_{cav}, is then given by substituting equation 3.43 into equation 3.40 to obtain:

$$R_{cav} = \frac{2Q{\mu_{12}}^2}{\hbar\epsilon_0 V}\zeta^2 \frac{{\Delta\omega_c}^2}{4(\omega_0 - \omega_c)^2 + {\Delta\omega_c}^2} \tag{3.44}$$

where the normalised dipole orientation factor is reintroduced (recall that this factor equal to 1/3 when averaged over all dipole orientations). In order to compare this emission rate into the cavity to free space, we first need to multiply equation 3.42 (DOS per unit volume) by the cavity mode volume V and substitute it into equation 3.40 to obtain the emission rate into free space:

$$R_{free} = \frac{{\mu_{12}}^2 \omega^3}{3\pi\epsilon_0 \hbar c^3} \tag{3.45}$$

By taking the ratio of the emission rate into the cavity to the free space emission the Purcell factor, F_p, is obtained:

$$F_p = \frac{R_{cav}}{R_{free}} = \frac{3Q(\lambda/n)^3}{4\pi^2 V}\zeta^2 \frac{{\Delta\omega_c}^2}{4(\omega_0 - \omega_c)^2 + {\Delta\omega_c}^2} \tag{3.46}$$

where c/ω has been replaced $(\lambda/n)/2\pi$ for which n is the refractive index of the medium inside the cavity. In an ideal cavity all of the photons emitted by the emitter would enter the cavity mode. In reality, since the direction of spontaneous emission is random only a fraction of the photons will enter the cavity mode and the rest will be lost to other non-resonant (free space) modes. This fraction is known as the beta factor (β-factor):

$$\beta = \frac{R_{cav}}{R_{cav} + R_{free}} = \frac{F_p}{F_p + 1} \tag{3.47}$$

The lasing experiments described in this thesis require the use of an ensemble of CQDs, the dipoles of which are randomly orientated with respect to the electric field. In this case the factor $\zeta^2 = 1/3$ as before. Furthermore, if an ideal case is assumed were the emitters are located at exact resonance with the cavity mode the expression for the Purcell factor becomes:

$${F_p}^{max} = \frac{3Q(\lambda/n)^3}{4\pi^2 V}\frac{1}{3} \tag{3.48}$$

3.6.2 Effective Purcell Factor

The derivation in section 3.6.1 of the Purcell factor assumes that the linewidth (or FWHM) of the emitter is much smaller than that of the cavity mode (i.e. a transform limited emitter) such that only the DOS of the cavity mode feature in equation 3.40. This is known as the good-emitter regime and here the Q-factor is dominated by that of the cavity. However, in solid-state systems such as the CQDs used in the experiments at hand electron-phonon interactions can broaden the emitter linewidth (homogenous broadening) rendering it much larger than the intrinsic cavity linewidth. This is known as the bad-emitter regime and is especially true for experiments described in this thesis where high-finesse cavities are coupled to CQDs at room temperature. For example, whereas the typical homogenous linewidths for CQDs is around 14 nm, for that of the cavity used in these experiments is typically around 0.1 nm[146]. In this case, one must use the expression for the effective Q-factor, Q_{eff}[146]:

$$\frac{1}{Q_{eff}} = \frac{\delta\lambda_{emit}}{\lambda_{emit}} + \frac{\delta\lambda_{cav}}{\lambda_{cav}} = \frac{1}{Q_{emit}} + \frac{1}{Q_{cav}} \tag{3.49}$$

where $\delta\lambda_{emit}$ and $\delta\lambda_{cav}$ are the linewidths of the emitter and the cavity and λ_{emit} and λ_{cav} are the emitter and cavity central wavelengths, respectively. Similarly, Q_{emit} and Q_{cav} are the emitter and the cavity Q-factors, respectively. It can be seen from equation 3.49 that if the linewidth of the emitter is much larger than that of the cavity then Q-factor is dominated by that of the emitter. In this case, substituting the effective Q-factor into equation 3.48 gives the effective Purcell factor, ${F_{p\eta}}^{eff}$[147]:

$${F_{p\eta}}^{eff} = \frac{3Q_{emit}(\lambda/n)^3}{4\pi^2 V}\eta(\lambda)\frac{1}{3} = {F_p}^{eff}\eta(\lambda) \tag{3.50}$$

where $\eta(\lambda) = g(\lambda)/g_{max}$ for which $g(\lambda)$ is the homogenously broadened spectral distribution of the emitter and g_{max} is its maximum value. This additional factor takes into account the detuning of the cavity mode from the maximum of the emitter spectrum.

3.7 Rate Equation Modelling

In this section a general form of the semi-classical coupled differential rate equation model, based on the Einstein model for interaction of matter and radiation is presented, to stimulate lasing behaviour of CQDs. Although the rate equations presented here are rather simple, it will be seen later that they will accurately reproduce the results of gain spectroscopy presented in this thesis. As an example system, we will consider a rate equation model for a three-level system as shown in figure 3.11. The total number of emitters contained in the physical cavity mode volume V_c with energy levels S_1, S_2 and S_3 is given by N_1, N_2 and N_3, respectively. Similarly, N_{nr} is the total number of emitters in the non-radiative state S_{nr} arriving from level S_2, which we assume decays very rapidly to level S_1. Furthermore, ϕ represents the total number of photons within the physical mode volume. An excitation by a pump to level S_3 decays very rapidly to level S_2, such that population inversion can be established between this level and S_1. The total number of emitters within the physical cavity mode will then be given by $N_{tot} = N_{conc} \times V_c = N_1 + N_2$, where N_{conc} is the concentration.

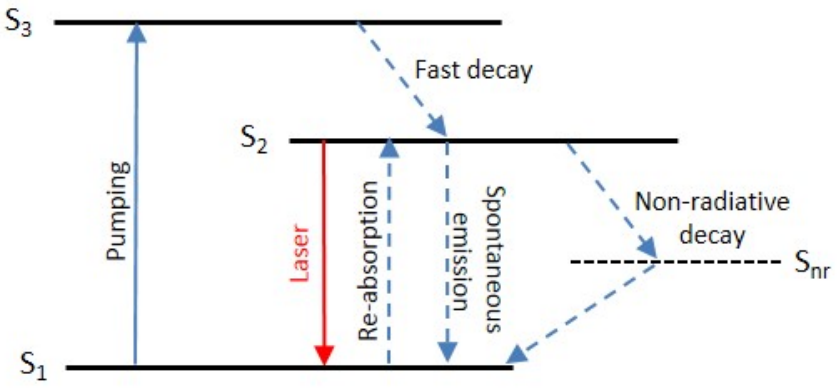

FIGURE 3.11: Three level laser scheme.

The rate equations governing these populations interacting with a narrowband radiation (such as a laser) centred at frequency ω are then given by the following set of equations[138]:

$$\frac{dN_1}{dt} = -\underbrace{P(t)}_{\text{pumping rate}} - \overbrace{N_1\Gamma B_{12}\rho(\omega)}^{\text{re-absorption rate of laser photons from } S_1 \text{ to } S_2} + \underbrace{N_2\Gamma B_{21}\rho(\omega)}_{\text{stimulated emission rate from } S_2 \text{ to } S_1} + \overbrace{N_2\Gamma A_{21}}^{\text{spontaneous emission rate from } S_2} + \underbrace{\frac{N_2}{\tau_{nr}}}_{\text{non-radiative rate from } S_2} \tag{3.51}$$

$$\frac{dN_2}{dt} = \underbrace{P(t)}_{\text{pumping rate}} + \overbrace{N_1\Gamma B_{12}\rho(\omega)}^{\text{re-absorption rate of laser photons from } S_1 \text{ to } S_2} - \underbrace{N_2\Gamma B_{21}\rho(\omega)}_{\text{stimulated emission rate from } S_2 \text{ to } S_1} - \overbrace{N_2\Gamma A_{21}}^{\text{spontaneous emission rate from } S_2} - \underbrace{\frac{N_2}{\tau_{nr}}}_{\text{non-radiative rate from } S_2} \tag{3.52}$$

$$\frac{d\phi}{dt} = -\overbrace{N_1\Gamma B_{12}\rho(\omega)}^{\text{re-absorption rate of laser photons from } S_1 \text{ to } S_2} + \underbrace{N_2\Gamma B_{21}\rho(\omega)}_{\text{stimulated emission rate from } S_2 \text{ to } S_1} + \underbrace{N_2\Gamma A_{21}}_{\text{spontaneous emission rate from } S_2} - \overbrace{\frac{\phi}{\tau_{cav}}}^{\text{cavity decay rate}} \tag{3.53}$$

where $B_{12/21}$ are the Einstein B coefficients, $\rho(\omega)$ is the total energy density, A_{21} is the Einstein A coefficient and Γ is the confinement factor, which determines the fractional energy contained in the active gain medium. The Einstein B coefficients can be related to the absorption/emission cross-sections as $\sigma_{12/21} = \frac{\hbar\omega}{v_g}B_{12/21}$, where $v_g = c/n$ is the group velocity and n is the material refractive index. The Einstein A coefficient can be related to the radiative lifetime as $\frac{1}{\tau_{rad}} = A_{21}$. Furthermore, the energy density can be related to the number of photons inside the cavity with the active mode volume V_c using the relation $\rho(\omega) = \frac{\hbar\omega\phi}{V_c}$. Moreover, it can be shown that the stimulated emission cross-section can be related to the radiative lifetime as $\frac{v_g\sigma_{21}}{V_c} = \frac{\beta}{\tau_{rad}}$[148], where β is the beta factor defined in equation 3.47.

It was shown in section 3.6 that the presence of the cavity strongly modifies the optical DOS and, thus, will modify the spontaneous as well as stimulated emission rates. This

can be taken into account by simply replacing τ_{rad} with the cavity enhanced emission rate $(F_p + 1)/\tau_{rad}$, where F_p is the Purcell factor given by equation 3.48 (or equation 3.50 for homogenously broadened systems).

In the lasing experiments presented in this thesis pumping is achieved using a pulsed excitation source. In order to explicitly take into account the time dependence the temporal profile of the pumping term it is described using a Gaussian function of the form:

$$G(t) = \frac{P_{num}}{\sigma_t\sqrt{2\pi}} e^{-\frac{(t-t_{off})^2}{2{\sigma_t}^2}} \tag{3.54}$$

such that

$$\int_0^\infty G(t)\,\mathrm{d}t = P_{num} \tag{3.55}$$

where P_{num} is the total number of photons per pulse, $\sigma_t = \frac{L_t}{2\sqrt{2ln2}}$ is the standard deviation for which L_t is the temporal FWHM of the excitation laser and t_{off} is its time-offset. The fraction of the photons that enter the cavity mode, $spat(\omega_0)$, is given by:

$$\int_0^{2\pi}\int_0^{\omega_0} spat(r) r\, dr d\theta = spat(\omega_0) \tag{3.56}$$

where

$$spat(r) = \frac{1}{2\pi{\sigma_{spt}}^2} e^{-\frac{r^2}{2{\sigma_{spt}}^2}} \tag{3.57}$$

is the normalised 2-D Gaussian function which describes the spatial intensity distribution of the laser spot into the cavity and ω_0 is the mode waist. Here $\sigma_{spt} = \frac{L_{spa}}{2\sqrt{2ln2}}$ is the standard deviation for which L_{spa} is the FWHM of the laser spot. The limit of the integration in equation 3.56 to only the mode waist of the cavity is the result of mode-matching i.e. where only a fraction of the photons from the pump pulse enter the cavity mode (the mode waist is in these experiments is typically a lot smaller than the pump spot size). The number photons that go on to excite the CQDs per unit time is then given by:

$$P(t) = \varsigma T G(t) spat(\omega_0)\left(1 - e^{-\frac{\sigma_{abs} N_{conc} L_c}{T}}\right) \tag{3.58}$$

where ς is the QY, T is the cavity transmission aat the pump wavelength, σ_{abs} is the absorption cross-section at the excitation wavelength. The QY is here takes into account the fraction of the carrier generated by the pump photons that are then trapped at surface defects etc... i.e. those that do not contribution to the emission at the band-edge states. The exponential function describes the Beer-Lambert law which calculates the fraction of the photons that remain after travelling through the physical cavity length, L_c. Thus, the fraction that are absorbed by the emitters and go on to excite them is given by subtracting the exponential from unity. Equations 3.51 - 3.53 then become:

$$\frac{dN_1}{dt} = -\underbrace{\varsigma TG(t)spat(\omega_0)\left(1-e^{-\frac{\sigma_{abs}N_{conc}L_c}{T}}\right)}_{\text{pumping rate}} - \overbrace{\frac{N_1\Gamma v_g\sigma_{12}\phi}{V_c}}^{\text{re-absorption rate of laser photons from } S_1 \text{ to } S_2} + \underbrace{\frac{N_2\beta\Gamma(F_p+1)\phi}{\tau_{rad}}}_{\text{stimulated emission rate from } S_2 \text{ to } S_1} + \overbrace{\frac{N_2(F_p+1)}{\tau_{rad}}}^{\text{spontaneous emission rate from } S_2} + \underbrace{\frac{N_2}{\tau_{nr}}}_{\text{non-radiative rate from } S_2} \tag{3.59}$$

$$\frac{dN_2}{dt} = \underbrace{\varsigma TG(t)spat(\omega_0)\left(1-e^{-\frac{\sigma_{exc}N_{conc}L_c}{T}}\right)}_{\text{pumping rate}} + \overbrace{\frac{N_1\Gamma v_g\sigma_{12}\phi}{V_c}}^{\text{re-absorption rate of laser photons from } S_1 \text{ to } S_2} - \underbrace{\frac{N_2\beta\Gamma(F_p+1)\phi}{\tau_{rad}}}_{\text{stimulated emission rate from } S_2 \text{ to } S_1} - \overbrace{\frac{N_2(F_p+1)}{\tau_{rad}}}^{\text{spontaneous emission rate from } S_2} - \underbrace{\frac{N_2}{\tau_{nr}}}_{\text{non-radiative rate from } S_2} \tag{3.60}$$

$$\frac{d\phi}{dt} = -\overbrace{\frac{N_1\Gamma v_g\sigma_{12}\phi}{V_c}}^{\text{re-absorption rate of laser photons from } S_1 \text{ to } S_2} + \underbrace{\frac{N_2\beta\Gamma(F_p+1)\phi}{\tau_{rad}}}_{\text{stimulated emission rate from } S_2 \text{ to } S_1} + \underbrace{\frac{N_2\beta\Gamma(F_p+1)}{\tau_{rad}}}_{\text{spontaneous emission rate from } S_2} - \overbrace{\frac{\phi}{\tau_{cav}}}^{\text{cavity decay rate}} \tag{3.61}$$

Note in the case of open access microcavities used in the experiments the spontaneously emitted photons go into the cavity mode (fraction β) as well free space (fraction 1 - β). Thus by adding these two terms we arrive the spontaneous emission terms in equations 3.59 and 3.60 that are independent of β. In equation 3.61, however, we do need to include β as only this fraction contributes to ϕ.

By inserting a set of specific set parameters, as summarised in table 3.1, equations 3.59-3.61 can be solved numerically (using MATLAB) to reveal a threshold behaviour. Note that these parameters are chosen such that lasing can be obtained from the rate equations at a sensible threshold. Figure 3.12a displays a graph of the photon density (ϕ) as a function of the time plotted on a log-linear scale for two different pumping power, one below (blue) and one above (red) the lasing threshold (P_{th}). It can be seen that above threshold there is much faster recombination due to stimulated emission compared to the spontaneous emission curve below threshold. A plot of the time integrated photons density (Φ) reveals a clear threshold behaviour (at around 15 pJ per pulse) as seen in figure 3.12b. In order to determine the lasing threshold a linear least squares fit is made at this graph to the power dependence curve on a log-log scale, both above and below the threshold as shown in figure 3.12b. The lasing threshold is then the value at which the two lines intersect.

3.8 Conclusion

In this chapter the concept of quantum confinement was introduced leading to different electronic density of states which depend strongly on the dimensionality of the CQDs. By extending this concept to core-shell systems like the ones used in this experiment different electron and hole wave function localisation regimes were identified, allowing the CQDs to be classified as either type-I, quasi type-II and type-II depending on the degree

Excitation spot size, L_{spa}	5 μm
Transmission, T	0.9
Absorption-crossection, σ_{abs}	1×10^{-18} m^2
Radiative lifetime, τ_{rad}	15 ns
Non-radiative lifetime, τ_{nr}	50 ps
Purcell factor, F_p	0.003
Concentration, N_{conc}	5×10^{22} m^{-3}
Refractive index, n	1.5
Physical Mode volume, V_c	9×10^{-18} m^3
Confinement factor, Γ	0.7
Cavity decay rate, τ_{cav}	50 ps
Absorption cross-secton, σ_{12}	5×10^{-21} m^2
QY, ς	60%

TABLE 3.1: Summary of an arbitrary set of parameters for the theoretical model.

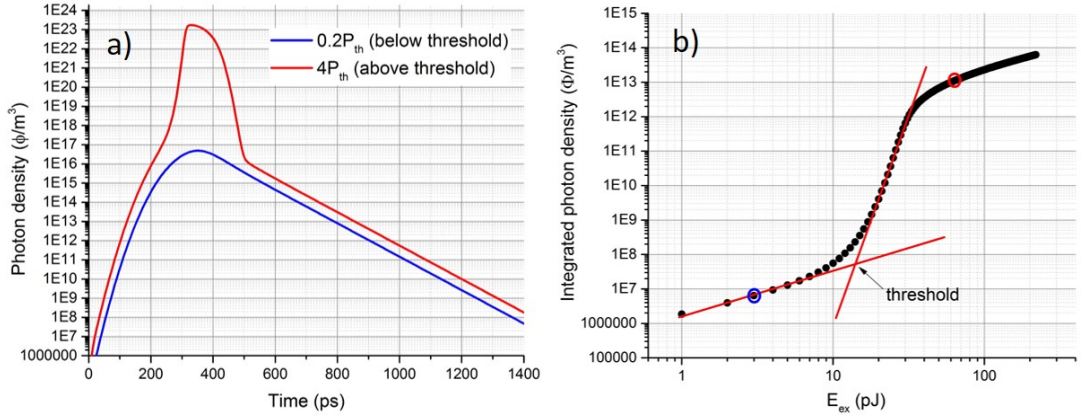

FIGURE 3.12: Rate equation output. a) Plot of photon density (ϕ) as a function of time below (blue) and above (red) threshold P_{th}. The rapid initial decay above threshold is signature of stimulated emission. b) A plot of time integrated photon density (Φ) as a function of the pumping power showing a clear threshold behaviour. The circles correspond to the pumping power for the traces showing in a).

of overlap between the carriers. Quantum confinement effects were shown to accurately describe the energy level structure of CQDs and which were in very good agreement with the experimentally observed absorption spectra. However, in order to explain the emission properties of the CQDs it was necessary to consider the ground-state exciton fine structure, which has strong influences from electron and hole exchange interaction, spin-orbit interaction, the crystal field and the shape asymmetry of the CQDs.

The description of the energy level structure lead to the condition for optical gain in CQDs. In CQDs with exciton-exciton interactions energies smaller than the ensemble inhomogeneous linewidth biexcitons are required in order to achieve optical gain and stimulated emission (type-I CQDs). By spatially separating the electron and hole pairs using the appropriate core-shell structures an internal Stark effect is created which

greatly increases the exciton-exciton interaction energy beyond the ensemble inhomogeneous linewidth enabling lasing in the single exciton regime. Although the CdSe/CdS core-shell structures used in this thesis have the potential to show lasing in the single exciton regime, as shown by Grivas *et al*[115] using dot-in-rods structures, in the case of spherical CQDs and NPs very thick shells would be required to meet the condition for single exciton gain. In this case, the CQDs used in this experimental will require biexcitons to produce optical gain. The basic theory of lasing was then introduced. By comparing the total losses to the gain a condition for the lasing threshold was obtained.

Some important cavity parameters such as the Q-factor and finesse were introduced followed by a description of the Hermite-Gaussian modes which are produced in hemispherical cavities. This then lead to the description of the coupling between CQDs and the cavities used to produce lasing described in the context of cavity quantum electrodynamics. The cavity was shown to strongly modify the optical DOS for the CQDs leading to an enhancement (or suppression) in their emission lifetimes (Purcell effect). In this regard, the homogenous broadening resulting from electron-phonon interactions in CQDs can reduce the CQD-cavity coupling and this was taken into account by an effective Q-factor (the bad-emitter regime). The latter result will be important in the theoretical treatment of the results of gain spectroscopy, as will be seen in chapters 5 and 6. The chapter ended with a detailed discussion of the rate equation model used to describe a three-level laser. By inserting a set of sensible parameters the rate equations where solved numerically to demonstrate lasing behaviour.

Chapter 4

Experimental Methods

4.1 Introduction

The chapter discusses the experimental techniques used to successfully perform lasing experiments with CQDs. Initially, the experimental tools used to characterise the CQDs are discussed. These include measuring radiative lifetime, PL and absorbance measurements as well as measuring the ultrafast non-radiative Auger process. Accurate measurements of such quantities is required in the interpretation of the results as well as development of the theoretical descriptions that describe gain spectroscopy results.

The sample preparation process will then be discussed with a focus on achieving high packing densities, a key parameter needed to obtain lasing. The mirror alignment process is then highlighted, which is crucial on obtaining small cavity lengths, and brief a discussion on the efficient coupling of the excitation laser to the CQDs will be given. This is followed by the description of the experimental set-up used to perform gain spectroscopy experiments. Finally, a description of the techniques used to measure some of the other key parameters, such as excitation laser spot size and the concentration of CQDs inside the cavity, will be presented.

4.2 Materials characteriation

4.2.1 Lifetime Measurements

As will be seen in chapters 5 and 6 the lifetime of the excited state of the CQDs is an important experimental parameter in the theoretical treatment of the results of gain spectroscopy. In order to measure the lifetime it is necessary collect photons emitted by

the CQDs into a detection device which is sensitive enough to detect arrival of single photons. Examples of these include photomultiplier tubes (PMTs), avalanche photo-diodes (APDs) or single photon avalanche photo-diodes (SPADs), and the last was the detector used in the experiments in this thesis. The SPAD functions by producing a current pulse (of order mA) upon arrival of a photon with a timing resolution of 100s of ps. A pulsed laser source is used to excite the CQDs and is required to have both the temporal pulse width and the arrival time between two consecutively laser pulses shorter and longer, respectively, than the CQD lifetime. For this reason, a PicoQuant LDH-D-C-375 diode laser was used producing photons at wavelength 375 nm and with a pulse width below 100ps. In conjunction, a PicoQuant PDL 800-D laser driver was used with an adjustable repetition rate between 31.25 kHz-80 MHz, and can also be operated in the continuous wave regime. In the case of the lifetime measurements the repetition rate was set to 1 MHz producing a time difference of 1μs between the arrival of two consecutive laser pulses, which is much larger than the typical lifetime of the CQDs. The laser driver generates a current pulse used in the production of the laser and simultaneously generates a trigger pulse which is fed into an electronic device called a time-correlated single photon counter (TCSPC). The current pulses generated by the SPAD are also fed into the TSCPC. The device then correlates the two currents pulses by measuring the difference in the time of arrival between current pulse from the laser driver and from the SPAD, which indicates the arrival of a photon from the CQDs. The data is then plotted in the form of histograms of intensity versus time, which is referred to as time-resolved photoluminescence spectrum (TRPL). In order to obtain accurate lifetimes measurements the timing resolution of the TCSPC must be very quick and for the device used in this thesis this was $\sim$ 900ps, which is faster than the typical radiative decay rate of CQDs. In order to improve the signal to noise ratio the lifetime data was obtained by integrating over$\sim$ 150 s (i.e. over 150 x 10^6 laser pulses).

Figure 4.1 shows the schematic of the lifetime setup. Both of the CQDs (NCs and NPs) are initially in the solution form dissolved in hexane, reflecting the fact that the gain spectroscopy experiments were also performed using solution-based CQDs. Although the concentration of this original solution was unknown, the concentration of the NCs when placed inside the cavity (also in solution form) was measured to be of the order $\sim$ 10^{23} m^{-3} (see section 4.6 for details on how the concentration was measured), giving a packing density of $\sim$ 20% by volume. However, it is expected that the concentration of the original solution in hexane is slightly lower and the reason for this is stated in section 4.3. For the NPs the concentration was not measured in the same way as for the NCs (the method detailed in section 4.6 was developed after the lasing experiments using NPs were conducted), however, rate equation simulations suggested a concentration of $\sim$ 10^{21} m^{-3}, giving a packing density of $\sim$ 0.5% by volume inside the cavity (as will

be seen in Chapter 6). Furthermore, the CQDs were placed in a 10 ml vial with a diameter of $\sim$ 1 cm. The excitation laser is directed at the vial containing the CQDs, the direction of which is at right angles to the collection arm of the set-up to minimise the laser light entering the SPAD. An additional 450 nm long pass (LP) filter is used to block any remaining scattered light entering into the SPAD. The emission from the CQDs is initially collimated and then focused using a microscope objective with $\times$ 20 magnification onto a multimode fibre which then directs the photons onto the SPAD. The objective is fitted to a z-axis translation mount to optimise the signal into the fibre.

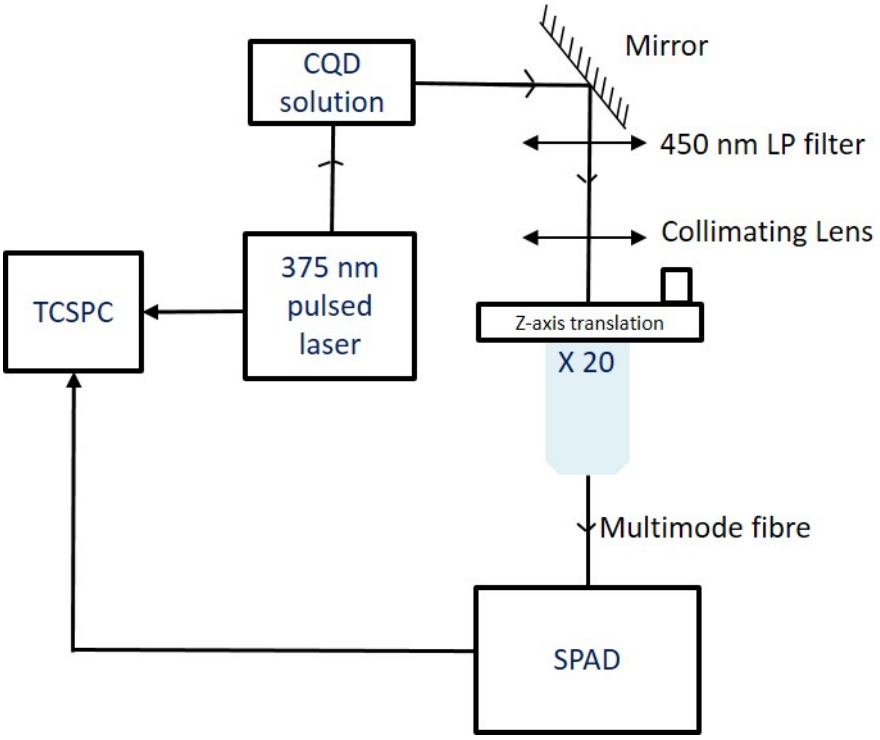

FIGURE 4.1: Schematic of the lifetime measurement apparatus.

4.2.2 Photoluminesence Spectroscopy and Absorbance Measurements

Together with lifetime measurements photoluminescence (PL) and absorbance measurement are vital in interpreting the results of gain spectroscopy and in its theoretical treatment. Figure 4.2 shows the schematic of the experimental set-up used to obtain PL data from an ensemble of solution-based CQDs. Unlike lifetime measurements where a pulsed excitation is required a CW excitation will suffice in this case. The CQDs were excited using a 375 nm PicoQuant LDH-D-C-375 diode laser operated in the continuous wave regime. The excitation is at right angles to the collection angle to minimise mixing of the signal and the laser beam. The emission from the CQDs is isotropic and part of the signal is then collected using a $\times$ 10 microscopy objective, which is then directed

into the Andor shamrock 500i spectrometer attached to a Newton 940 CCD (thermo-electric cooling) by initially focusing the signal onto the spectrometer slit to obtain a PL spectrum. A 450 nm long pass filter is used to block any remnant laser beam entering into the spectrometer.

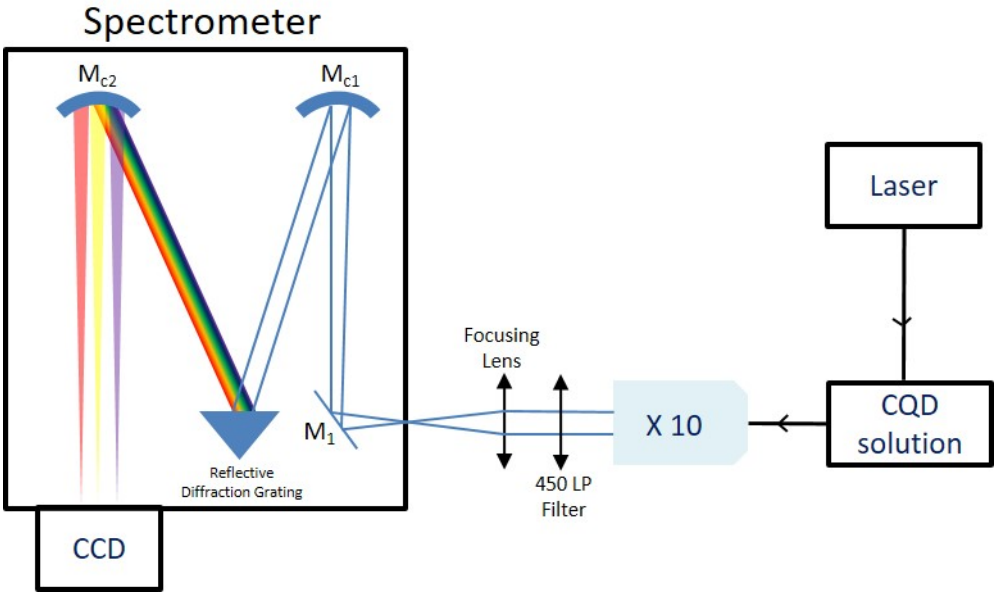

FIGURE 4.2: Schematic of the PL measurement apparatus and the spectrometer. M_1 is a planar mirror and M_{c1} and M_{c2} are curved mirrors used for collimation and focusing of the light.

Absorbance measurements were taken using the Cary 5000 UV-Vis-NIR spectrometer (wavelength range 175-3300 nm) for the CQDs in solution form. The samples are initially diluted, with the concentration typically less than 1mg/mL (in terms of the QCDs this is a very clear solution). Mathematically the absorbance, A, at a certain wavelength can be calculated by taking the negative logarithm of the ratio of the incident radiant flux (Φ^i) to the transmitted (Φ^t):

$$A = log\left(\frac{\Phi^i}{\Phi^t}\right) = -log(T) \tag{4.1}$$

where $T = \frac{\Phi^t}{\Phi^i}$ is the transmittance of the material. The sample are prepared in a clear quartz cuvette as this is transparent to light in the UV region. A basic representation of the spectrometer is given in figure 4.3. In order to take into account any absorbance from the cuvettes and from the solution dissolving the CQDs a reference (or a blank) sample is also inserted into the spectrometer which is just an another cuvette containing the dissolving solvent (hexane). The spectrometer then measures the true absorbance of the sample for a selected wavelength range of interest (typically 200nm - 800 nm in the case of CQDs).

FIGURE 4.3: Schematic of the Cary 5000 UV-Vis-NIR spectrometer. A white light source is dispersed using a diffracting grating. A particular wavelength of light is then selected by the exit slit which is then directed onto the sample and fraction of the light remaining is then passed onto the detector. The diffraction grating is rotated into order to cover the full wavelength range of interest.

4.2.3 Pump-probe Spectroscopy

A very useful experimental tool in studying the properties of CQDs is called Transient Absorption (TA) Spectroscopy or Pump-Probe spectroscopy. In TA a pump pulse generates excited carriers and the absorption change is then measured by a second lower intensity probe pulse. The probe pulse can be either generated from either a monochromatic tunable source (e.g. optical parametric amplifier) or from a broadband light source (e.g. pulses of femtosecond white-light continuum generated in a sapphire plate) and the timing between the pump and probe pulses can be controlled with femtosecond or picosecond resolution. Thus, by monitoring the changes in the absorption or transmission in the time and spectral domain one can obtain information regarding electronic energies, carrier relaxation and recombination dynamics on an ultrafast timescale.

The physical quantity measured in this project was the normalised or fractional transmission:

$$\frac{dT}{T_{grd}} = \frac{T_{exc} - T_{grd}}{T_{grd}} \tag{4.2}$$

where T_{exc} and T_{grd} are the excited state and the ground state transmission. The fractional transmission of the excited state population is governed by three different physical processes, which are also shown schematically in figure 4.4.

1. **Bleach** The pump pulse puts a significant fraction of the CQDs into the excited state (state-filling) and thus reduced the population of the ground state. In this case $\frac{dT}{T_{grd}} > 0$
2. **Stimulated emission** There is a probability that an incoming probe photon from the probe pulse stimulates radiative emission from the excited state to the ground state, hence the transmission of the probe pulse is amplified. Again in this case $\frac{dT}{T_{grd}} > 0$

3. **Induced absorption** Induced absorption can happen for two different reasons. One is the result of the electric fields generated by carriers initially excited into high energy states. The induced electric fields leads to modifications in the oscillator strength (Stark effect) of the original transitions shifting them to new energies while reducing the absorption strength at the position of the original ones. As a result, $\frac{dT}{T_{grd}}$ <0 (induced absorption) at the position of these new transitions and $\frac{dT}{T_{grd}}$ >0 (bleaching) at the position of the original transitions. However, induced absorption change in QCDs can also often be a direct consequence of carrier trapping. For example, ultrafast carrier trapping can lead to additional excitation into surface states or an unoccupied state due to the surrounding solvent (section 2.5.2).

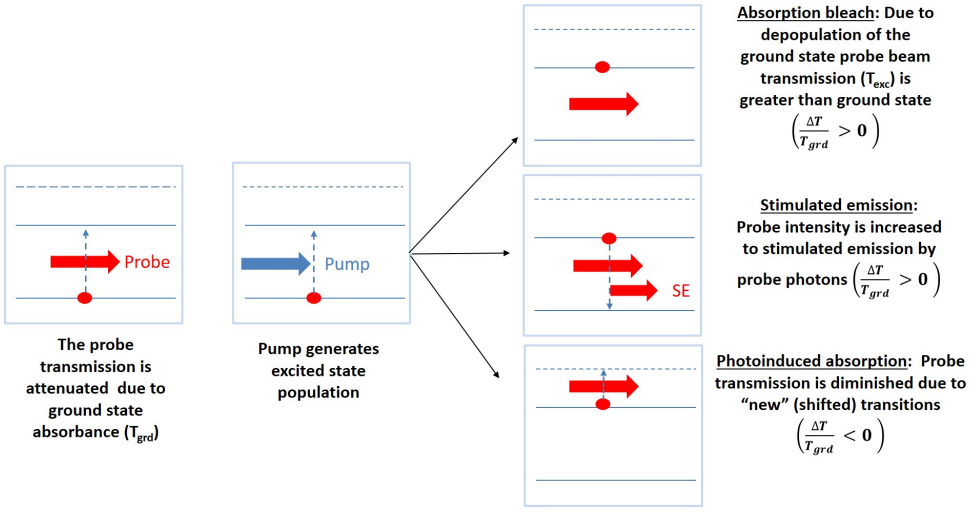

FIGURE 4.4: The processes involved in pump-probe spectroscopy.

This technique was employed in this project to measure the multiexciton Auger lifetimes of the CQDs. Measuring the Auger lifetime is important in informing which excitation source to use (it is desirable to have the temporal pulse duration of the laser to be smaller than the Auger lifetime), in calculating the required packing density of the CQDs to obtain lasing (equation 2.1 in chapter 2) and also in formulation of the theory of gain spectroscopy. To do this the probe wavelength is fixed at a particular wavelength, which is typically resonant with the lowest emitting transition (or the band-edge state) as this is the transition of interest in lasing experiments. The delay between the pump (the wavelength of which is well above the band gap) and probe is then varied at a femo or pico-second time scale to produce a time transient.

All pump-probe experiments on CQDs were performed with our collaborators at the University of Manchester. Figure 4.5 shows a schematic of this experimental set-up. A mode-locked Ti:sapphire regenerative amplier laser system (Spectra-Physics Spitre-Pro)

is used to produce pulses at 800 nm at 1 kHz repetition rate with a pulse duration of 100fs. A beam splitter was used to direct 95% of the light into an optical parametric amplifier (OPA, Light Conversion Ltd. TOPAS-C) which is used to produce the pump beam photons with a wavelength that is tunable from the ultraviolet to the visible region. Subsequently, the pump beam was passed through a mechanical chopper synchronized to half the repetition rate of the laser (500 Hz) before being focused onto the sample. A neutral density (ND) filter was used to control the power delivered to the sample. The other 5% forms the probe beam and was directed onto a delay stage which is computer controlled to vary the delay time between the probe and the pump beam. The power was again controlled using an ND filter before being directed into a sapphire crystal to produce a white light continuum (via the process of supercontinuum generation). This was subsequently split using a beam splitter to form a probe beam and a reference beam which was passed through a spectrometer (SpectroPro 2500i) and then onto a Si photodiode. The probe beam was then focused onto the sample and directed into the spectrometer (the sample and the reference beams are directed onto separate Si photodiodes) and minute changes in the difference in the intensities of the reference and the probe beams can then be detected using a digital lock-in amplifier (Stanford Research Systems SR830). This amplifier was synchronized to the mechanical chopper to improve the signal-to-noise ratio. The samples were magnetically stirred at 1000 rpm to circulate the NC solution through the pumped volume and is known to reduce the build-up of trapped charges at the surfaces, hence avoiding the formation of trions[149–151].

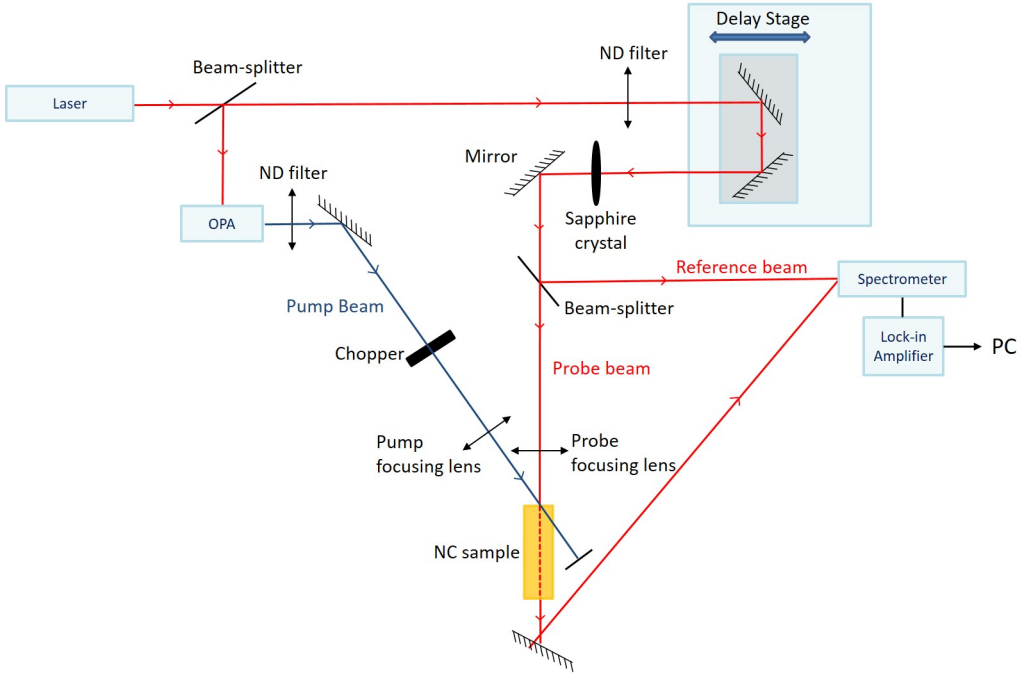

FIGURE 4.5: Schematic of the pump-probe spectroscopy set-up.

4.3 Sample Preparation

In order to prepare the samples the cavities are initially cleaned by soaking them in chloroform which removes residual CQDs and other organic matter that may be there from previous experiments and then are sonicated in acetone for ~ 5 mins as additional mean to clean them. Two different systems are examined in this thesis, which are the CdSe/CdS NCs and nanoplatelets (NPs). The nominal CdSe core diameter of the spherical CQDs was 4.23 nm with a 2.6 nm (or ~ 7.6 ML) CdS shell thickness. The nominal CdSe core dimensions of the NPs are $\sim 44 \times 8 \times 1.35$ (nm), with ~ 0.7 nm (or 2 ML) CdS shell thickness encapsulating the core. Both the shperical CQDs and NPs are passivated with oleic acid ligands. As was mentioned in section 2.5.3 in order to achieve stimulated emission and lasing the packing density of the CQDs must be over a certain value. This is so that, according to equation 2.1, the stimulated emission rise time can be faster than the non-radiative Auger process, which, at least in the case of spherical CQDs, ultimately puts an intrinsic limit of the optical gain lifetime. As well as achieving a high packing density it is also important to produce smooth CQD films into order to reduce scattering of the photons which can degrade the quality of the optical modes and ultimately the lasing performance.

In order to satisfy both of the aforementioned criteria (high packing density and smooth films) two methods were initially implemented. These are spin-coating (SPS Spin150) and drop-casting. Since all of the CQDs were initially dispersed in the solvent hexane, which is highly volatile at room temperature, the solvent quickly evaporates leaving behind only the CQD film. The initial concentration of the solution, however, was not known. The CQD solution was deposited directly on top of the planar mirror of the cavity. Although spin-coating gave good quality films, it failed to produce lasing, which was most likely due to the low packing density produced in these films. On the other hand, drop-casting can produce very high packing densities due to the coffee stain effect[152] and has been shown to producing lasing from CdSe/CdS nanorods[153]. However, in our case this method produced films that were too thick (greater than the RoC ~ 25 μm of the cavity and thus beyond the stability of the optical modes, see section 3.5.3) and/or the films were too rough to observe a proper mode structure.

Eventually this problem was solved by mixing octadecane into the solution of CQDs containing the hexane. Octadecane has a boiling point 317 °C and is thus highly non-volatile. This means with the correct mixture drop-casting the solution into the planar mirror will initially increase the concentration of the CQDs (due to the evaporation of the solvent hexane) but because of the octadecane CQDs remain in the form of a solution at room temperature during the course of the experiment. This method produced the required high packing density and reduced scattering of the photons in the solution.

By systematically increasing the octadecane volume, an ideal mixture was found to be a solution containing between 3 - 5.6% octadacane by volume for both NCs and NPs (and thus the other being hexane). It is important to note that during the course of the experiments, which takes $\sim$ 2-3 hours, there will be negligible evaporation of the octadecane and so does not influence on the results of gain spectroscopy.

4.4 Experimental Set-up

Figure 4.6a shows the schematic of the experimental set-up. In all experiments the CQDs are excited using a pulsed laser system. An ND filter was used to control the power delivered to the CQDs. A fraction of the laser power is directed into a power meter (Thorlabs, PM100D). The rest of the power is directed onto a 0.4 numerical aperture (NA) objective with a magnification of $\times$ 20 which focuses the excitation laser beam onto the cavity. The CQD emission is collected using a 0.25 NA lens with $\times$ 10 magnification and directed on the spectrometer with a cooled silicon CCD camera (Andor newton 970). A 450 nm long-pass filter is used to block the excitation beam going into the spectrometer. During alignment a temporary white light source (in place of the x 20 objective) is used to image the cavities in transmission using a webcam/CCD for alignment purposes (see section 4.5). Fine tuning of the cavity length is given by fixing the planar mirror to a ring actuator (HPSt 1000/35-25/7, piezosystem jena GmbH) with a maximum travel range approximately 7 μm. The length was controlled using a Keithley 2400 voltage source meter. Figure 4.6b shows expanded view of the cavity geometry containing the CQD solution. The entire cavity set-up is mounted on a XYZ translational stage which provides independent manoeuvrability of the cavities with respect to the excitation objective lens. This is very useful in optimizing the position of the excitation beam onto the cavity.

The data acquisition was automated by using the software Labview for all experiments. The automation process was crucial in order to obtain many lasing spectra over a short period of time, which would otherwise be very time consuming. This requires the use of a stepper motor (controlled using an Arduino UNO microcontroller) attached to the ND filter to automatically increment the power of the excitation laser in a step-by-step manner, whilst the power and the spectra get recorded automatically by the software after each iteration. Similarly, part of the data analysis (the fitting of the lasing spectra) was also automated using Labview.

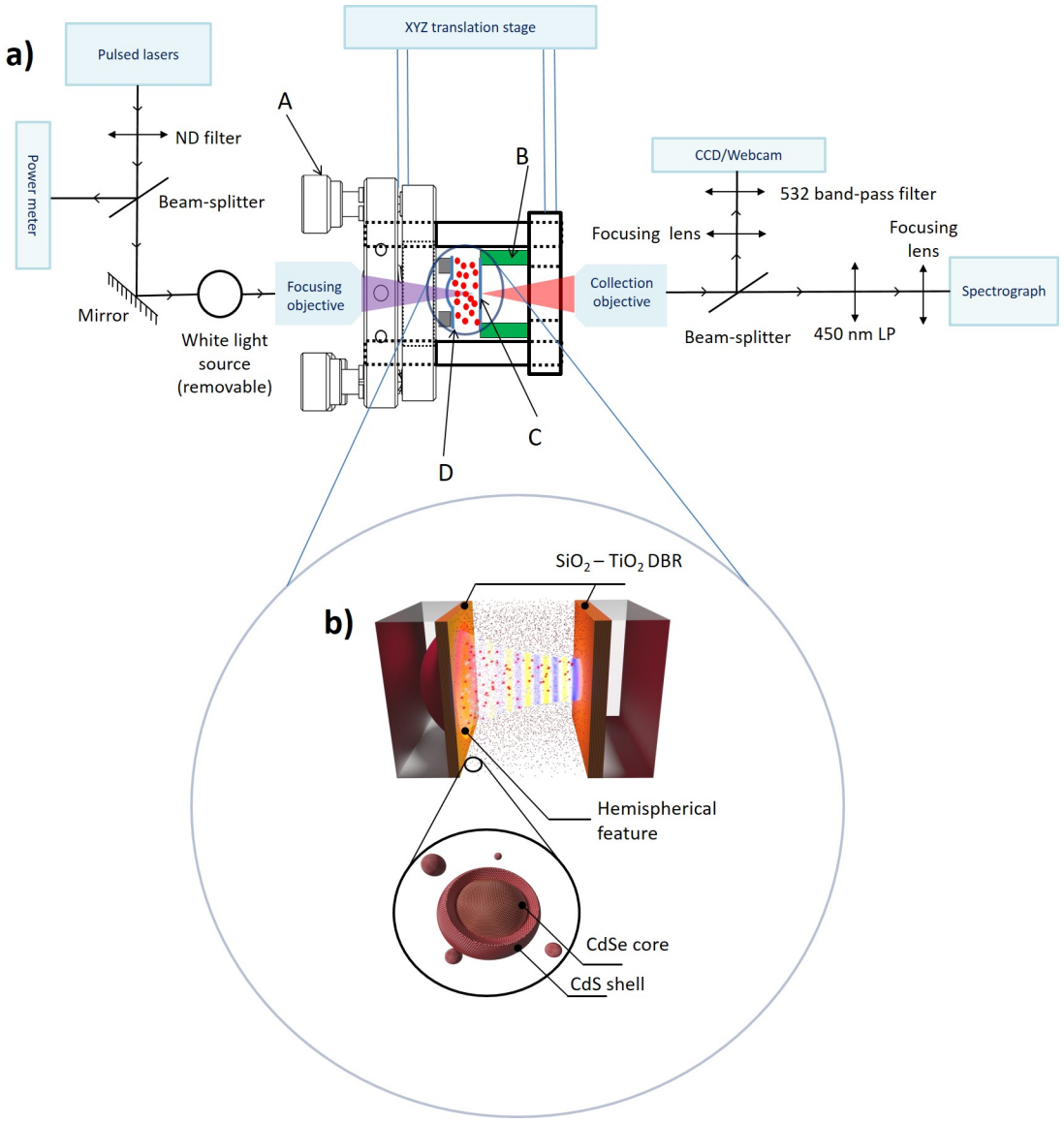

FIGURE 4.6: The experimental set-up. a) Schematic of the experimental set-up used to perform gain spectroscopy. A = tilt control, B = piezo ring actuator, C = planar mirror, D = hemispherical mirror. b) Cavity consisting of a planar and a hemispherical mirror each with $\lambda/4n$ alternating pairs of SiO_2/TiO_2 forming distributed Bragg reflectors (DBRs). Image b) courtesy of Dave Coles.

4.5 Cavity Alignment and Coupling

After the deposition of the CQD solution onto the planar mirror the cavity is mounted onto the experimental set-up as shown in figure 4.6a. As was mentioned previously, in order to produce stable cavity modes it is necessary to get the cavity length below the RoC of the hemispherical mirror, which in this case is 25 μm. In order to achieve such short cavity lengths the angle between the hemispherical and the planar mirror is adjusted such that both mirrors are as parallel as possible. This is achieved by a three-axis kinematic control attached to the hemispherical mirror (labelled A in figure 4.6a),

which can also be used to coarsely control the separation between the cavity mirrors. During this alignment procedure a temporary white light source is used to image the cavities in transmission. Using the × 10 objective a focused image is created onto the webcam/CCD. The white light is filtered using a 532 nm band-pass filter which creates interferences fringes (Fabry-Pérot modes) as a result of angular deviation between the two mirrors when the two mirrors are brought close to each other. Upon bringing the mirrors into a more parallel configuration the number of fringes is reduced. This process in shown in figure 4.7. With this method physical cavity lengths between 1-4 μm are produced, and since the gain medium is in solution form and fills the entire cavity volume the cavity length is also equal to the gain medium thickness.

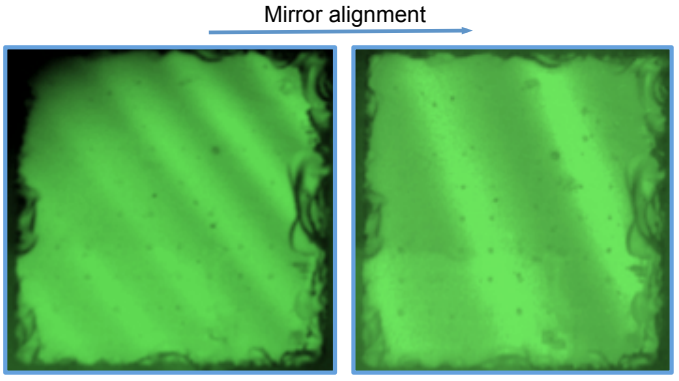

FIGURE 4.7: Mirror alignment. White light transmission shows multiple fringes in case of a misaligned cavity (left) and in the case of an aligned cavity (right) where the number of fringes are reduced. Image courtesy of Sam Johnson.

Once the cavity is aligned parallel they are imaged onto the camera. The white light source is then removed to allow for the excitation of the CQDs using a laser, which is focused down onto the cavity using the × 20 objective. Finally, using the XYZ translation stage the cavities are carefully manoeuvred relative to the excitation beam until cavity modes can be seen on the spectrometer. Such cavities modes are shown in figure 4.8a overlaid on top of the ensemble PL curve (grey). In this case three fundamental cavity modes (TEM_{00}) and their associated transverse modes $TEM_{m+n\ \#\ 0}$ can be seen. From this spectrum the cavity length, which is an essential parameter in the theory of gain spectroscopy, can be calculated by measuring the FSR and then using the formula 3.17. Although this formula is an approximate for hemispherical cavities it can be used to estimate the cavity length. Using this the mode number, q, can be determined from equation 3.38. This is important as the initial cavity length almost always allows for more than one longitudinal mode with the stop-band of the cavity. This is referred here to the "open-cavity " case. However, as will be seen in the following chapters single mode lasing, which is highly desirable from a technological standpoint, requires only a single longitudinal mode to exist within the stop-band (referred to as the "closed-cavity" case). This can be achieved by decreasing the cavity length (as shown in figure

4.8b) and by tracking the number of modes that sweep by the final cavity length can be determined by using equation 3.38 again. To perform gain spectroscopy the cavity length is controlled using the ring actuator using the voltage source, which gives fine control on the spectral position of the modes. Typical FWHM of the CQD ensemble are $\sim$ 24-32 nm and for those of the cavity modes are $\sim$ 0.15-0.6 nm (minimum), giving Q-factors of $\sim$ 4000-1000. It will be seen in the next chapter that the cavity Q-factors are in fact limited by the self-absorption (and also scattering) of the lasing photons inside the cavity, and not by the reflectivity of the cavity mirrors.

Note that during the course of the experiment there is a constant spectral drift of the optical modes. The cause of this drift is the mechanical relaxation of the springs used to control the kinematic and which consequently causes small changes in the cavity length. This makes it challenging to lock the cavity mode in one spectral position, which is crucial in performing accurate gain spectroscopy measurements. In order to get around this problem the voltage on the ring actuator used is constantly adjusted manually to keep the mode in a desired spectral position during data acquisition.

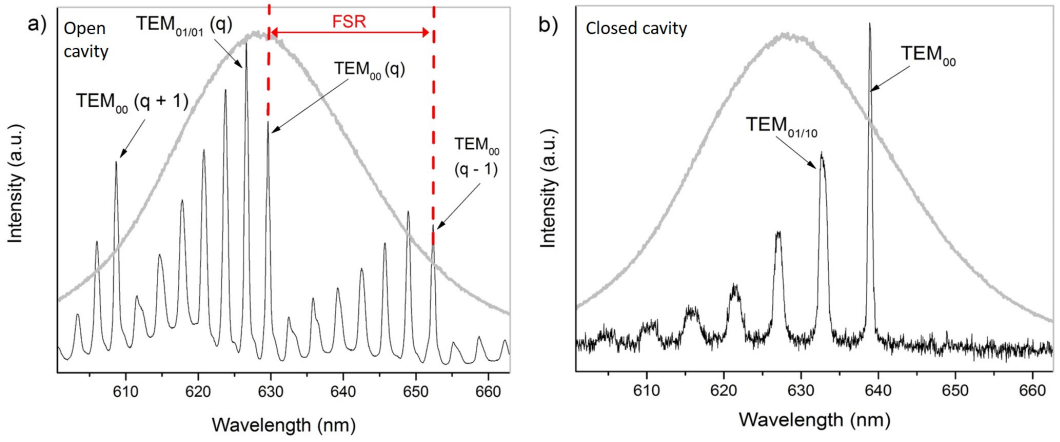

FIGURE 4.8: Cavity modes. a) Three TEM_{00} modes with mode numbers q - 1 to q + 1 are seen from the emission of CQDs coupled to the cavity. Their corresponding transverse modes can also be seen. The modes are overlaid on top of the ensemble PL spectrum (grey). b) By decreasing the cavity length the FSR range can be increased to enter the single longitudinal mode regime where only one TEM_{00} mode can be seen.

4.6 Measuring Spot Size and Concentration

The excitation spot size and concentration of CQDs solution inside the cavity are also important physical parameters that feed into the theoretical description of the results of the gain spectroscopy. To measure the spot size an image of the excitation spot (which is essentially formed because of the PL emission from the CQDs) is formed using the spectrometer CCD. A horizontal and a vertical trace is taken across the middle of the

spot and a Gaussian function is fitted to each to extract the FWHM. This process shown in figure 4.9a and b respectively. The spot size is taken as the average of the horizontal and vertical FWHM. The pixel number now needs to be converted into real length units. In order to do this an apparatus called the Ronchi ruling is used. This is simply a series of evenly spaced opaque lines which when viewed in transmission using a white light and focused produces an image like the one shown in 4.9c. Since the spacing between the lines is known (in this case 10 μm) the number of pixels between two lines can then be measured and used calibrate the pixel number with the length. This then allows the spot size measured in pixels to be converted into real units. Note that an objective lens of the same magnification used to image the spot size must be used to image the Ronchi ruling.

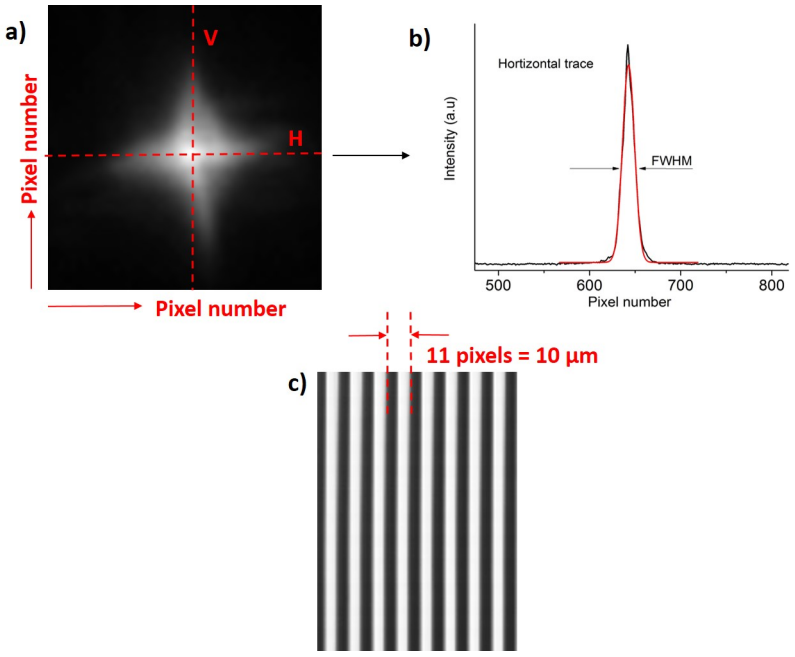

FIGURE 4.9: Measurement of the spot size. a) An image of the excitation spot size viewed using a CCD. Horizontal and vertical traces are taken to estimate the spot size. b) The spectral intensity profile of a horizontal trace. The FWHM is taken by fitting a Lorentzian profile. c) Ronchi ruling imaged using a CCD.

To measure the concentration initially the transmission of the cavity containing the CQDs, (I), was measured using a laser. To do this, the laser beam was focused using an objective lens onto to a single cavity. The laser power entering the objective lens was measured. The power of the transmitted laser was then measured from the other side of the cavity. The transmission of the cavity without any CQDs was then measured as a reference, (I_0), using and identical set-up. The cavity length was matched as closely as possible to the original experiment. Then, the concentration, C, can be determined using the Beer-Lambert law 4.3:

$$ln\left(\frac{I_0}{I}\right) = \sigma_{abs} LC \tag{4.3}$$

where L is the cavity length and σ_{abs} is the absorption cross-section at excitation wavelength. In the case of shperical CQDs the value of σ_{abs} can be estimated by the method detailed by Park *et al*[154], which will be highlighted below. We estimate the absorption cross-section of the spherical CQDs at very high spectral energies (such as for the excitation laser at 400 nm used to measure the concentration) using the following equation[76]:

$$\sigma_{abs} = \frac{4}{3}\pi\alpha(\omega)|f(\omega)|^2 \frac{n_{CQD}}{n_{solv}} R^3 = \xi(\omega)R^3 \tag{4.4}$$

where $\alpha(\omega)$ is the absorption coefficient at frequency ω, n_{CQD} and n_{solv} are the bulk material and solvent refractive indices, respectively, R is the CQD radius and $f(\omega)$ is the local-field correction factor, which takes into account the difference in the electric field outside and inside the semiconductor material. In the case of the spherical core-shell CQDs equation 4.4 takes the form of:

$$\sigma_{abs} = \xi_{core}(\omega)R^3 + \xi_{shell}(\omega)[(R+H)^3 - R^3] = \xi_{shell}\,(R+H)^3 + [\xi_{core}(\omega) - \xi_{shell}(\omega)]R^3 \tag{4.5}$$

where R and H is the CQD core radius and shell thickness (nm), respectively. In the case of CdSe/CdS the optical constants at 400 nm are $\xi_{core}(400nm) = 3.50 \times 10^{-16}$ cm^2nm^{-3} and $\xi_{shell}(400nm) = 3.43 \times 10^{-16}$ cm^2nm^{-3}[154]. Thus, the total cross-section at 400 nm is found by substituting these values at into equation 4.5 to obtain:

$$\sigma_{abs}(400nm) = 3.43 \times 10^{-16}\,(R+H)^3 + 7 \times 10^{-16} R^3 \approx 3.43 \times 10^{-16}\,(R+H)^3 \tag{4.6}$$

Whereas the above approach is valid in the case of spherical CQDs, the same method cannot be used in the case of NPs due to their non-spherical shape. In this case, however, a value from literature (reference [16]) for NPs with similar core and shell dimensions to the ones used in this thesis is taken at the desired excitation wavelength (450 nm), as will be mentioned in chapter 6.

4.7 Conclusion

In this chapter the experimental techniques used to characterise the CQDs were presented. These measurements are essential in order to understand the results of gain spectroscopy as well as in the formulation of the theoretical descriptions of the results.

Initial attempts to prepare closed-packed films of CQDs (from a solution of CQDs containing hexane) onto the planer mirror of the cavity failed to produce lasing. Here two methods were used, spin-coating and drop-casting. Whereas spin-coating produced good quality films, it failed to produce a high enough packing density to obtained lasing. Drop-casting on the other hand can produce high packing densities, however, the thickness of the films were either too large (greater than the RoC of the cavity used which was ~ 25 μm) and/or the quality of the films were bad such that a proper mode structure could not be obtained (due to scattering of the photons from the roughness of the film). Eventually, an optimal sample preparation method was found by adding a small quantity of a non-volatile solvent such as octadecane to the CQD solution containing hexane. Upon depositing the solution of the mirror a highly concentration CQDs solution is formed. This produced a solution with required packing density and also minimised the scattering inside the cavity to produce lasing from good quality optical modes.

The description of the experimental set-up to carry out the gain spectroscopy experiments presented including the mirror alignment procedure, which is important in achieving small cavity lengths. Finally, methods to estimate the estimate the excitation spot size and the concentration of CQDs inside the cavity was also mentioned.

Chapter 5

Gain Spectroscopy of CdSe/CdS Nanocrystals

5.1 Introduction

This section presents the results of gain spectroscopy of solution based CdSe/CdSe core-shell spherical NCs using tunable open access microcavities. Understanding the interplay between the various absorption and emission processes is essential in order to optimise the NC design. One method of performing gain spectroscopy of CQDs is the transient absorption (or pump-probe) method[82], which also allows the investigation of the ultrafast intraband carrier relaxation dynamics. However, optical gain and such ultrafast relaxation processes are considerably removed from lasing behaviour in the presence of optical feedback, and a good understanding of the lasing process is currently lacking.

Tunable cavities and laser emission have been demonstrated by others using, for example, electric-field[111, 118]], strain[117], or pressure[119]. However, these methods have too low a tuning range to enable useful spectroscopy or there is a chance that the emission properties of the NCs may be modified due to changes made to their environment, making the interpretation of the results difficult. On the other hand, in our cavities the NCs experience no change in temperature or stress during tuning and so the changes in lasing performance can be attributed unambiguously to the change in feedback wavelength. To date, this is the first time NCs have been coupled to an open access cavity system to study the lasing behaviour enabled via in-situ tuning of the cavity feedback wavelength. Furthermore, tunable and single mode laser emission from the fundamental cavity mode is demonstrated, for which the spectral resolution is limited only by the resolution of the actuator. Finally, a theoretical model is proposed which accurately

describes the results of gain spectroscopy and provides insights into the processes that govern the lasing behaviour of the NCs. The study forms the basis our publication in Advanced Optical Materials[155].

5.2 Nanocrystal Lasing Experiments

This section describes gain spectroscopy experiments conducted using CdSe/CdS spherical NCs using hemispherical cavities of $\beta = 25$ μm. The mirrors consist of 10 pairs of alternating SiO_2/TiO_2 with maximum reflectivity of 99.87% at the design wavelength of 640 nm (this is calculated using the transfer matrix method as highlighted in section 3.5.2). The nominal diameter of the CdSe core is 4.23 nm and the CdS shell thickness is 2.6 nm (corresponding to $\sim$ 7.6 ML). These samples were provided by our collaborators at the Samsung Advanced Institute of Technology. Two batches of such NCs were provided, which we will call SAIT-1 and SAIT-2, both having nominally the same core and shell thicknesses. Both were passivated with oleic acid ligands. The NC sample was prepared using the method outlined in section 4.3. The experimental set-up is described in section 4.4. In all the lasing experiments the focus was primarily on the lasing behaviour of the fundamental cavity mode (TEM_{00}). From a technological standpoint it is expected that the fundamental cavity mode should give the lowest lasing thresholds, produce minimal beam divergence and enable single mode lasing.

5.2.1 Power Dependence Curve

This section concerns experiments using SAIT-1. The experiments were conducted using a frequency double mode-locked Ti:sapphire laser (Mira 900) at 400 nm with a pulse duration of 100 fs and capable of delivering energies in excess of 700 pJ per pulse. A pulse picker was used to reduce the repetition rate from 76 MHz down to between the range 40-80 kHz in order to prevent photo-bleaching of the NCs[156–158]. These experiments were conducted in the lab of Prof Robert Taylor in the Department of Physics (University of Oxford). Figure 5.1a shows typical emission spectra below threshold (blue) where the fundamental cavity mode located at 641 nm (TEM_{00}) with the mode number q and higher order transverse modes (up to $m + n = 4$) can be seen. Note that on the higher wavelength side of the fundamental mode $(q, 0, 0)$, other transverse modes associated with a lower longitudinal mode number $q - 1$ can also be seen. By measuring the FSR and using equation 3.17 the optical cavity length was calculated to be 5.3 μm. Then, by using equation 3.38 the value q was calculated to be equal to 17. As the pumping power is increased multimode laser emission from the fundamental and higher order cavity modes can be seen (green).

In order to confirm NC lasing a power dependence spectrum is obtained. This is a plot of the intensity of the optical mode versus the pumping power. Lasing is identified by a characteristic kink in the power dependence resulting from the stimulated emission process. The integrated intensity (I) of the fundamental mode as a function of excitation energy per pulse (E_{ex}) plotted on a log-log scale reveals a clear threshold behaviour, as presented in figure 5.1b. Here, two power dependence graphs are for the same cavity mode but located at two different spectral positions (622 and 641 nm as seen in the inset of figure 5.1b), tuned into position by changing the cavity length. These display lasing with thresholds of 190 ($\pm$ 7.6) pJ per pulse at 622 nm and 80 ($\pm$ 3) pJ per pulse at 641 nm, strongly hinting at the variation of the lasing threshold as a function of spectral positon. Figure 5.1b also shows the FWHM as a function of excitation energy which can be seen to drop sharply at threshold due to the increase in the coherence time of the system and quickly reaches the resolution limit of the spectrometer ($\sim$ 0.1 nm). This sharp reduction in the linewidth provides conclusive evidence of lasing and also provides an accurate way of measuring the lasing threshold. Note that the linewidth of the mode below threshold at 641 nm is narrower than that of the mode at 622 nm due to weaker re-absorption of cavity photons by the NCs (see Section 5.2.2). Moreover, the lasing indicates that the minimum packing density required to achieve lasing has been exceeded in our system (see equation 2.2).

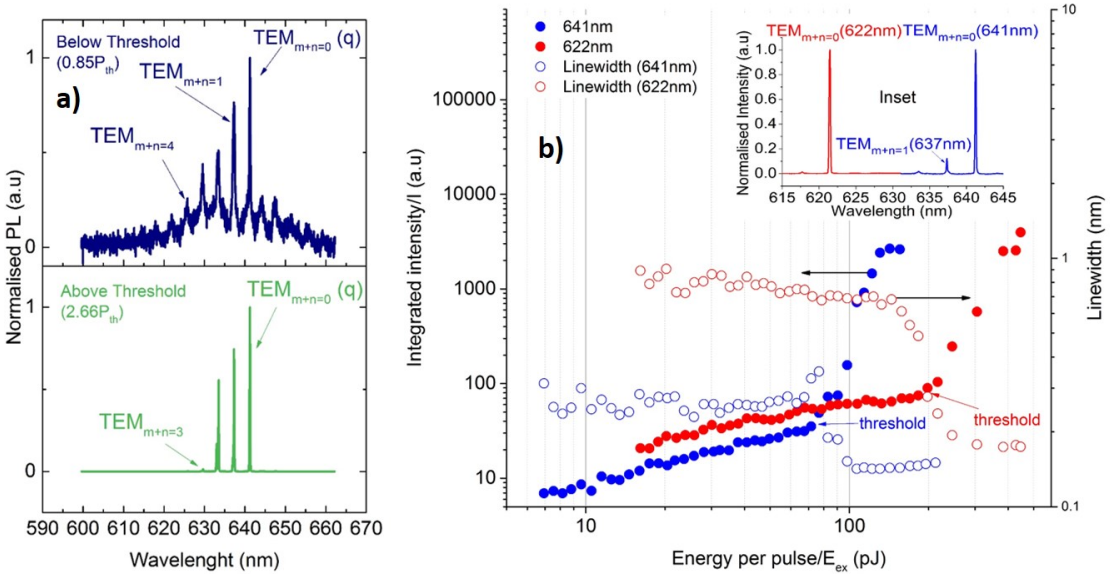

FIGURE 5.1: NC lasing.(a) Spectra below and above threshold at pump energies of $0.85P_{th}$ and $2.66P_{th}$ (400 nm excitation), respectively, and where P_{th} is the threshold energy per pulse. Multi-mode laser emission (from $TEM_{m+\ n\ =\ 0}$ to $TEM_{m+\ n\ =\ 3}$) can be seen above threshold. (b) Threshold behaviour from the fundamental cavity mode, $TEM_{m+\ n=0}$, at two different spectral positions (622 nm and 641 nm), along with the linewidths, showing a sharp decrease at threshold. The inset shows the spectra of this lasing mode at two different spectral positions, both above threshold.

5.2.2 Gain Spectroscopy

Once lasing was achieved the cavity length was then tuned to place the cavity mode in the desired spectral position and the threshold extracted. Figure 5.2a shows a graph of the threshold as function of the wavelength for the fundamental cavity mode and the first transverse mode ($TEM_{m\,+\,n\,=\,1}$) over a range of $\sim$ 32 nm. The lasing threshold for both modes shows a clear minimum at around 638 nm which is red-shifted by $\sim$ 10 nm from the ensemble PL peak. The full ensemble PL curve (FWHM 32 nm) and the absorbance curves are shown in figure 5.2b. It is also interesting to see that the lasing thresholds for the first transverse mode are equal in magnitude to the fundamental cavity mode. This is somewhat unexpected given that finesse, and hence the threshold of the transverse mode, is expected to be lower, however, the reason for this will be discussed a little later in the chapter.

This red-shifted lasing minimum indicates a spectral positon where the lasing process is the most efficient and is consistent with other observations in NCs[82, 95, 113, 159, 160] and also in dye-doped systems[161] in the absence of resonant optical feedback. In these reports, the appearance of ASE to the red of the PL peak has been justied by the fact that the net gain is a result of the competition between stimulated emission and absorption processes, the latter always being stronger at shorter wavelengths. However, the spectral position of this minimum can also be strongly influenced by the binding energy of multiexcitons. Gollner et al[162] showed that the position of the ASE peak in CdSe/CdS NCs can be tuned by altering the exciton-exciton interaction energy via modification of the core and shell sizes. Thus, both of the aforementioned factors could play a role in determining the measured gain profile of our NCs and this will be discussed further in section 5.3.2.

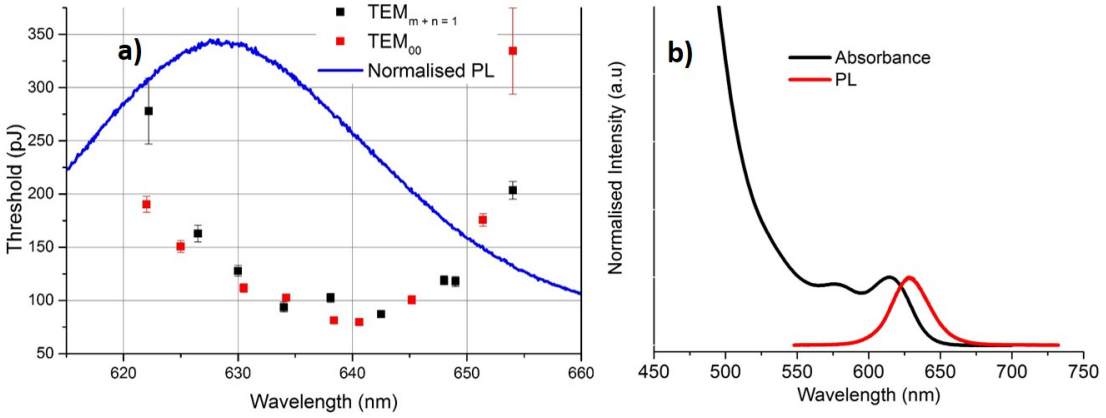

FIGURE 5.2: NC Gain spectroscopy. a) A plot of the lasing threshold of the TEM_{00} and $TEM_{m+\,n\,=\,1}$ as a function of wavelength, along with the normalised PL spectrum. a) c) Extended ground state absorbance (normalised at the first absorbance peak) and the normalised PL spectrum.

Before moving on it is important to confirm that the threshold behaviour seen as a function of wavelength is a property of the NCs rather than the cavity. In order to test this we have measured the Q-factor of an empty cavity for a similar cavity length ($\sim$ 5.3 μm) to the one used in the described experiment.

The linewidth ($\delta\lambda$) of the cavity filled with the NCs below the lasing threshold is plotted in figure 5.3 along with the normalised absorbance curve (grey). The Q-factor is calculated using equation 3.18. Consequently, in figure 5.3b the Q-factor is seen to increase with wavelength (blue) with a maximum value reaching around 3800. This is in contrast to the empty cavity (black) where the Q-factor is seen to decrease with the wavelength with a minimum value of around 6200 (this was measured with a resolution of 0.03 nm corresponding to a resolution limited Q-factor of 21000). The limit of Q-factor for the empty cavity can be the reflectivity of the mirrors or diffraction losses. More importantly, the Q-factor of the filled cavity is significantly lower than empty cavity which indicates it is limited by the re-absorption of the lasing photons. This provides an explanation of why the Q-factor is increasing with wavelength as the absorption of is always lower at higher wavelengths and confirms that the threshold behaviour we have measured is in fact the property the NCs themselves and has no influence from reflectivity of the cavity itself. Furthermore, this also explains why the threshold of the $TEM_{m\,+\,n\,=\,1}$ is equal to the TEM_{00} mode in figure 5.2. Even though the intrinsic Q-factor (i.e. for an empty cavity) of the $TEM_{m\,+\,n\,=\,1}$ will be lower the Q-factor of this mode in the presence of NCs will be re-absorption limited and will therefore be equal to the TEM_{00} mode.

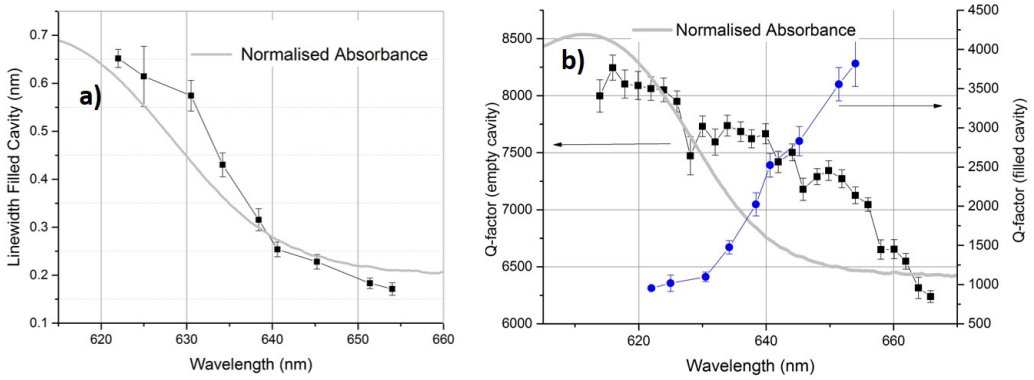

FIGURE 5.3: Measuring the quality factor. a) A plot of the FWHM of the TEM_{00} as a function of wavelength along with the normalised absorbance curve. b) A plot of the Q-factor for the empty cavity and the filled cavity as a function of wavelength, along with the normalised absorbance curve. In all cases the errors bars originate from the error in the linewidth given by fitting the modes with a Lorentzian function.

An interesting feature is revealed by looking at the power dependence curve below threshold on a linear-linear scale. This shown in figure 5.4a for the fundamental cavity mode located at 622 nm. It can be seen that the intensity of the mode saturates at high pumping powers before the onset of lasing. This hints at the multiexcitonic nature of

the optical gain in our NCs and can be understood as follows. At low pump energy the NCs mostly contain single excitons which are responsible for producing the PL emission. However, emission from multiexcitons is efficiently quenched by the non-radiative Auger recombination as this process can be much faster than the radiative lifetime of the multiexcitons. Hence, as the number of NCs containing single excitons saturates with increasing pumping power so does the emission intensity.

However, one can use this saturation behaviour to correlate the pumping power with the average exciton number per NC, $\langle N \rangle$. By considering the fact the PL emission from the ensemble is proportional to the probability that they contain at least one exciton, $1 - P(0)$, where $P(0)$ is the probability that they contain zero excitons we arrive at an equation for the spontaneous emission intensity below threshold, I_{sp}:

$$I_{sp} = P_{sp}(1 - e^{-\frac{E_{ex}}{E_1}}) \tag{5.1}$$

where P_{sp} is the intensity at saturation , E_{ex} is the excitation power and E_1 is the power at which $\langle N \rangle$ is equal to unity. The function, $P(k)$, where k is the number of excitons, is the Poisson probability distribution given by:

$$P(k) = \frac{\langle N \rangle^k e^{-\langle N \rangle}}{k!} \tag{5.2}$$

This fit is shown in 5.4a. By extracting the parameter E_1 a plot of $\langle N \rangle$ as a function of the pumping power is shown on the top axis. Figure 5.4b shows the plot of the average exciton number at threshold, $\langle N_{th} \rangle$, as function of spectral position. The graph shows a minimum in $\langle N_{th} \rangle$ with a value of ~ 1.5 at 638 nm coinciding with the minimum in the lasing threshold in figure 5.2a. This value suggests that lasing occurs from biexcitons which is consistent with what is calculated theoretically for type-I structures in section 3.4.1. The values of $\langle N_{th} \rangle$ measured experimentally can be compared to the ones calculated using the following equation[9]:

$$\langle N \rangle = \frac{T \sigma_{400nm} E_{ex}}{\hbar \omega A_{exc}} \tag{5.3}$$

where T is the transmission of the cavity mirror at the pump wavelength, σ_{400nm} is the absorption-cross section at the excitation wavelength (400 nm), E_{ex} is the pulse energy, $\hbar\omega$ is the excitation energy and A_{exc} is the area of the excitation spot. The assumption is that the absorption of the NC is non-saturable at the pump wavelength and that the probability of creating an exciton independent of the number of excitons already present inside the NC.

The absorption cross-section at 400 nm was estimated using the method detailed by Park et al[154] using the core and shell dimensions of our NCs and gives a value of $\sim 4 \times 10^{-18}$ m^2. The spot size (diameter) is also measured using the technique outlined in 4.6 and was $\sim$ 10.5 ($\pm$ 1.4) μm. The transmission at 400 nm for mirrors consisting of 10 pairs of alternating layers is $\sim$ 0.97 and is calculated using the transfer matrix method. Figure 5.4c compares the curve for $\langle N_{th} \rangle$ calculated using equation 5.3 to the one measured experimentally.

The error in the values calculated using equation 5.3 originate from the error in the measured lasing threshold pulse energies as well as the uncertainly in the measured spot size (using method shown in section 4.6). However, as will become clear in section 5.2.3 the measured spot size is likely very much bigger than the actual spot size due to the scattering of the photons from the CQD solution. This uncertainly in the A_{exc} value was not taken into account when calculating the analytical values, as it cannot be known by how much is the actual spot size is smaller than the measured value from this experiment. This reason for this is because the analytically calculated values in figure 5.4c (red) greatly exceeds the experimental values, even when using the measured spot size of 10.5 μm. This indicates that perhaps the excitation laser spot is not perfectly mode-matched to the TEM$_{00}$ mode (meaning a lot of the laser pump energy is lost in exciting the tranverse modes). If the excitation laser spot was perfectly mode matched to the TEM$_{00}$ mode then we would expect the analytically calculated values of $\langle N_{th} \rangle$ using the measured spot size of 10.5 μm to be smaller than the ones measured by using the saturation method due to the fact that the actual spot size is expected to be smaller than 10.5 μm. Note, however, that such mode mismatch should not influence value of $\langle N_{th} \rangle$ at threshold measured using the saturation method. Nonetheless, this points towards further experiments with the possibility of attaining even lower lasing thresholds by optimising the alignment such that the excitation laser is better mode matched to the TEM$_{00}$ mode, and these will be described in section 5.2.3.

Another physical quantity that can be extracted from the power dependence curve is the differential gain, η, which is just the slope of the curve above threshold. Figure 5.5a shows the power dependence curves for four different spectral positions, plotted on a linear-linear scale, and where the evolution of the slope can be clearly seen. By plotting the same curves on a log-log scale as shown in figure 5.5b, the differences in the thresholds can also be seen and correlate well with the slopes (lower slopes for higher thresholds). In order to measure the differential gain the integrated intensity of the cavity mode (I_{sp}) is initially normalised with the intensity at saturation (P_{sp}) to give the normalised intensity, χ. The differential gain is then extracted using a linear least squares fit to the graph of χ vs $\langle N \rangle$ above the lasing threshold i.e. ($\eta = \frac{d\chi}{d\langle N \rangle}$)as seen in figure 5.5c (shown for λ = 638.4 nm). A plot of η as a function of spectral positon in figure 5.5d shows a

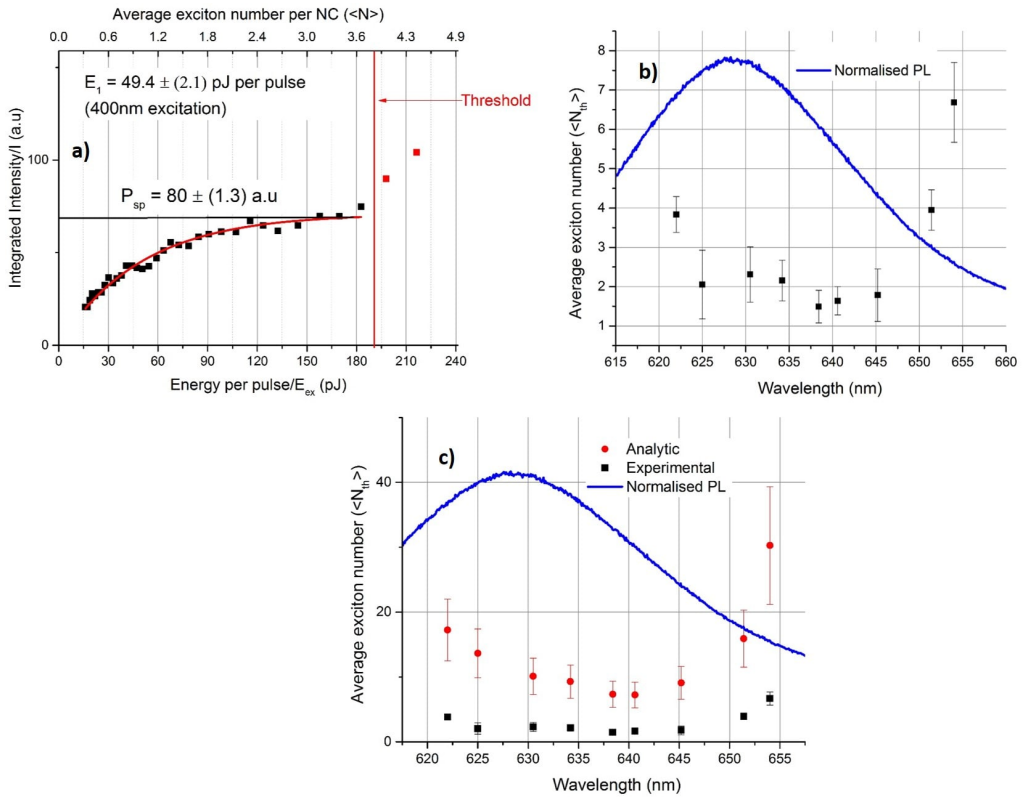

FIGURE 5.4: Calculating the average exciton number. a) Calibration of the pumping power with $\langle N \rangle$ for the TEM_{00} mode at 622 nm. b) A plot of experimentally measured values $\langle N_{th} \rangle$ as a function of wavelength for the TEM_{00} mode on top of the ensemble PL curve. c) A comparison of the $\langle N_{th} \rangle$ measured experimentally and those calculated using equation 5.3, for the TEM_{00} mode.

maximum in the differential gain corresponding to a spectral position where the lasing threshold is at its minimum. This provides further confirmation that the lasing process is indeed the most efficient at this spectral position. Moreover, the significant decrease of the differential gain at wavelengths larger than 654 nm and shorter than 622 nm also provides evidence as to why no lasing was observed beyond these spectral ranges.

5.2.3 Further Experiments to Improve Lasing Threshold

As was seen in the previous section a mismatch between the experimentally measured values of $\langle N_{th} \rangle$ and those calculated analytically suggests that there could be a mode mismatch between the TEM_{00} mode and the excitation laser. Thus, lower lasing thresholds can potentially be obtained by improving this alignment. As a result, further experiments were conducted to see if lower lasing thresholds were possible to achieve. On this occasion in order to ensure that the excitation laser spot is perfectly mode matched to the TEM_{00} mode the laser spot was manually scanned on top the hemispherical cavity by moving the cavity relative to the excitation spot using the XYZ translation stage,

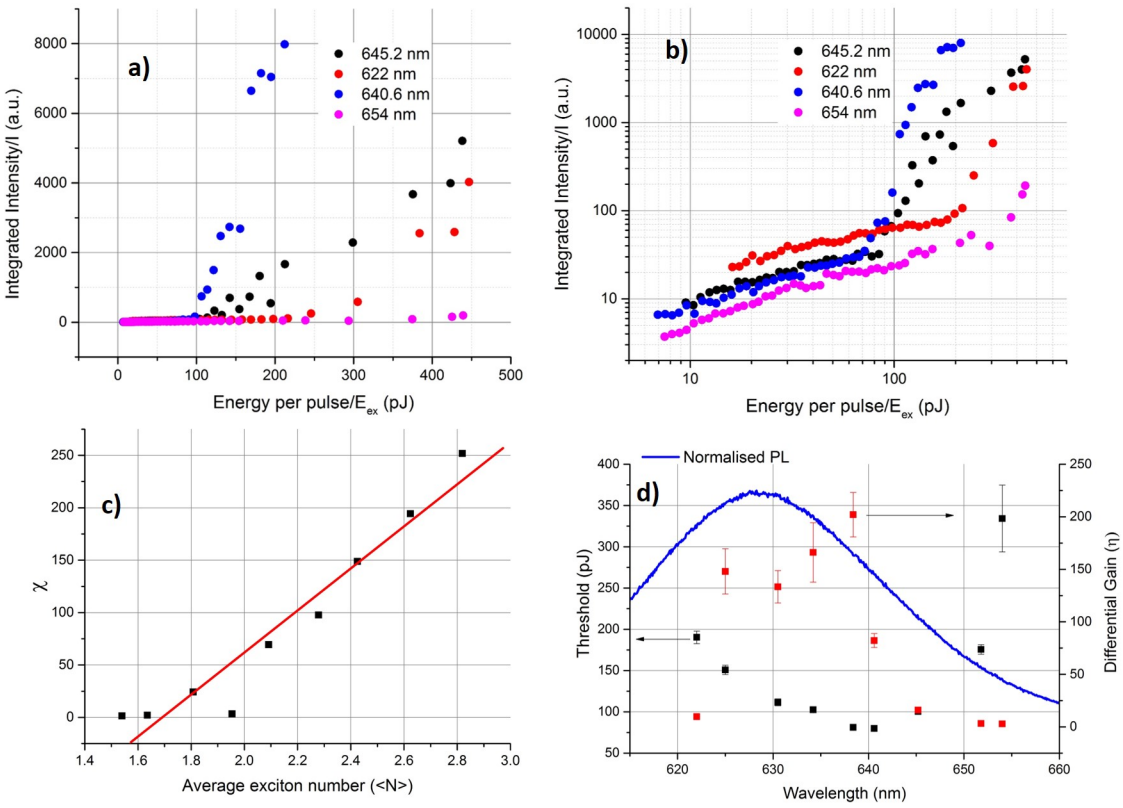

FIGURE 5.5: Differential gain. a) Different power dependence curves plotted on a linear-linear scale. b) Different power dependence curves plotted on a log-log scale. c) A linear least squares fit to extract the differential gain for the TEM_{00} mode at 638.4 nm. d) A plot of the lasing threshold and differential gain for the TEM_{00} mode along with the ensemble PL spectrum.

as shown in figure 4.6. The lasing threshold of the TEM_{00} mode was then measured at several spatial positions (say at the spectral position at which is minimum lasing threshold is expected i.e. $\sim$ 640 nm). Thus, the optimal mode matching condition is obtained when the lowest lasing threshold for the TEM_{00} mode is measured.

On this occasion, however, the second batch of the material, SAIT-2, was utilized as the first batch were used up. Figure 5.6a shows the lasing threshold as a function of spectral position along with the differential gain for the TEM_{00} mode both on top of the ensemble PL curve. The full PL (with a FWHM of 33 nm) and the absorbance curves are shown in figure 5.6b. As can be seen, there is a minimum in the lasing threshold of $\sim$ 7.5 ($\pm$ 0.2) pJ per pulse at $\sim$ 632 nm, which is red-shifted by about 9 nm with respect to the PL curve and coincides with the maximum in the differential gain at the same spectral position. This is consistent with what was observed using the SAIT-1 sample in section 5.2.2, however, the threshold minimum has blue shifted by $\sim$ 6 nm with respect to the SAIT-1 sample. This difference is perhaps a result of a slightly different core and shell thickness of the SAIT-2 compared to SAIT-1. However, the minimum lasing threshold is more than an order of magnitude lower than measured for the SAIT-1 sample.

Figure 5.6c shows a graph of $\langle N_{th} \rangle$ measured using the saturation curve as a function of wavelength (black squares). At the position of the lasing minimum (632 nm) $\langle N_{th} \rangle$ takes a values of ~ 1.4. This value is very close to what was obtained for the SAIT-1 sample at its minimum (1.5). It will be seen in section 5.3 that the lasing threshold depends strongly on the concentration of NCs. Therefore, if the lower lasing thresholds obtained for the SAIT-2 was simply due to a difference concentration then we should also expect the $\langle N_{th} \rangle$ values to be different for the SAIT-1 and SAIT-2. Thus, we can confirm that the lower lasing thresholds are a result of the fact that the excitation laser spot is better mode matched to the TEM_{00} mode and not due to the difference in the concentrations. As before the measured $\langle N_{th} \rangle$ can be compared to those calculated using equation 5.3, which are shown in 5.6c (red circles). However, in order to get a good agreement the measured spot size which had the diameter ~ 10 ($\pm$ 1) μm had to be reduced by a factor ~ 1.5 to a value of 6.5 ($\pm$ 0.7) μm (propagation of error is used here to calculate the erro in the reduced spot size). This mismatch can be attributed to the scattering of the photons from the NCs which increases the observed spot size. However, it is also important to note that since the actual spot size (the spot size without the influence of scattering) has not been measured directly, there will inevitably an error introduced in this value which cannot be accounted for in this experiment.

In order to show the reproducibility of the gain profile shown in 5.6a the gain spectroscopy experiment was repeated a further two times on different cavities, but with the same RoC (25 μm) and on the same sample. Thus, it is expected that the concentration and the excitation spot size will remained unchanged. Figure 5.7a shows the results of gain spectroscopy for further two cavities, cavities two and three (green and red, respectively) along with the first cavity (which we will call cavity one and is the same as in 5.6a). It can be seen all of the cavities show very similar threshold behaviour with a common minimum at around 632 nm. No lasing was observed for any of cavities for the spectral range greater than 647 nm and less than 618 nm. It can also be seen that in all of the cavities very similar lasing threshold are obtained giving further confirmation that the excitation laser is indeed optimally mode matched to the TEM_{00} mode.

However, as can also be seen the data points produce a lot of scatter. Therefore, in order to rule out the possibility that scattered data points are not produced due to photo-bleaching or charging an experiment was conducted where the lasing threshold was measured repeatedly at a particular spectral position. This is shown in figure 5.7b, where the lasing threshold was measured eight times consecutively at 632 nm in the case of cavity two. The threshold values are found to be fairly consistent providing evidence that there is no photo-bleaching or charging after each measurement. The jumps in the thresholds, for example, at number 5, which also reflect the scattered data in figure 5.7a, is then mostly likely due to some misalignment introduced into the system resulting from

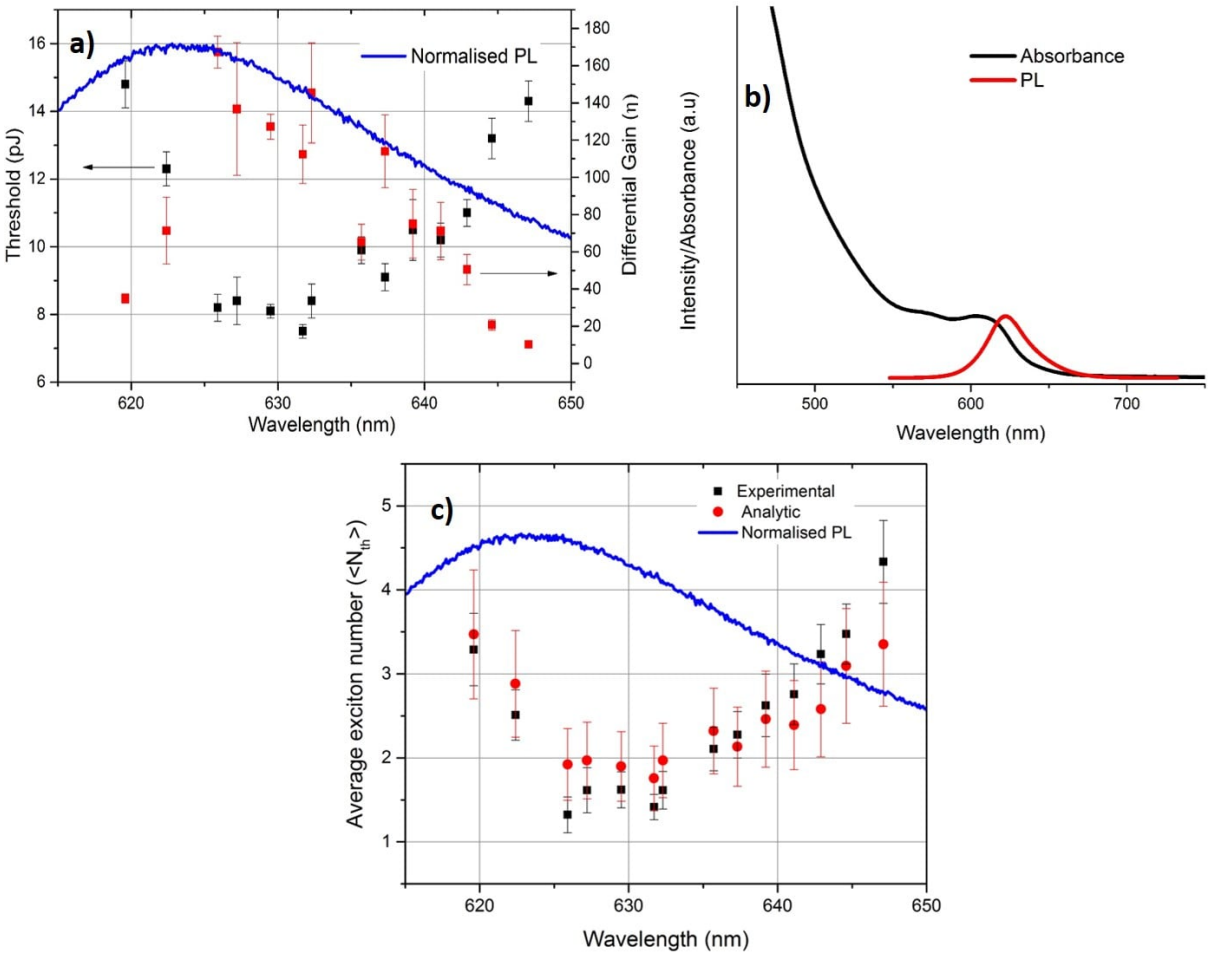

FIGURE 5.6: Gain spectroscopy with lower lasing thresholds. a) A plot of lasing threshold and differential gain as a function of wavelength, along with the normalised PL spectrum. b) The full normalised ensemble PL and the absorbance spectrum. c) A comparison of the experimentally measured values of $\langle N_{th} \rangle$ (squares) to the analytically calculated values (circles) on top on the ensemble PL spectrum.

the constant adjustment (manual) of the cavity length using the piezo to account for mechanical drift.

By taking the spot size of 6.5 ($\pm$ 0.7) μm converts to a minimum measured lasing threshold intensity of $\sim$ 23 ($\pm$ 5) μJ cm^{-2} at 632 nm (cavity one for which the lowest lasing threshold was measured). The error in the threshold comes from the error in the measure threshold ($\pm$ 0.2 pJ per pulse) as well as the error in the spot diameter ($\pm$ 0.7 nm). However, it is important to note that there is also a source of error due to the uncetainly in the measured spot size due to scatterring, which could not be taken account in this calculation.

The measured threshold is 100-200 times smaller than those previously reported in type I systems[159, 163] and lower than those reported for lasing in the single exciton regime ($\sim$ 60 μJ cm^{-2})[113]. The low lasing threshold measured here is, in fact, comparable to

ASE threshold of 30 μJ cm^{-2} as demonstrated by Guzelturk *et al*[95] (with a comparable pump pulse width of 120 fs) using CdSe/CdS NCs with a smooth confining barrier to reduce the Auger recombination rate, and also comparable to lasing threshold of 13.5 μJ/cm^2 from CdSe/ZnS NCs reported by McLellan *et al*[101] from a DFB laser. The lasing in the latter paper was, however, achieved with a 5 ns pump pulse width, and this was made possible by the use of alloyed core-shell CdSe/ZnS NCs to mitigate the effects of multiexcitonic Auger recombination (see section 2.6) and also by integrating a layer on top of the NC film made from polyvinyl alcohol (PVA) for better mode confinement. We attribute such low lasing thresholds in our experiments to the high absorption cross-section at the excitation (400 nm) due to the thick CdS shell, the high gain cross-sections due to their size and/or the high NC packing densities achieved inside of our cavities.

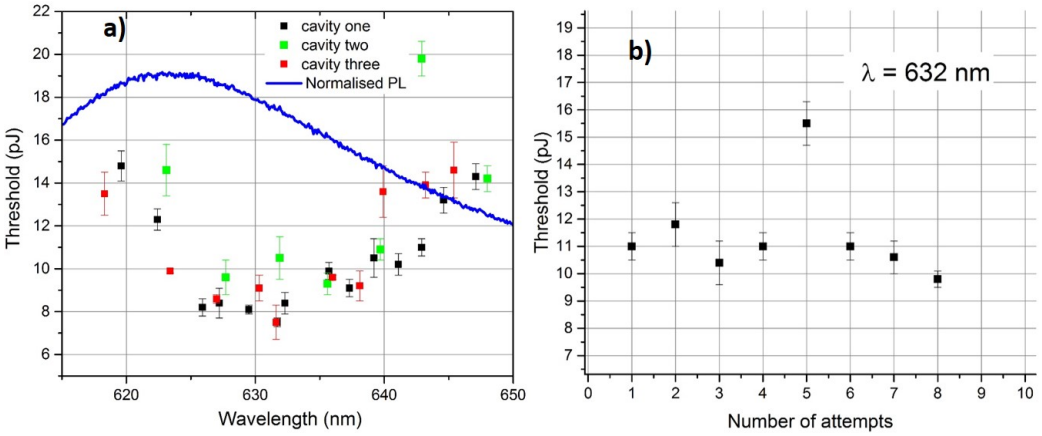

FIGURE 5.7: Reproducibility experiments. Threshold as a function of wavelength for three different cavities, along with the normalised PL spectrum. b) Eight consecutive threshold measurements at the 632 nm for cavity two.

5.2.4 Tunable Lasing

As seen in the previous section the threshold and the differential gain can be measured at any wavelength within the spectral range over which lasing is observed by tuning the cavity length. This sort of cavity architecture therefore also provides a very convenient way to tune the laser emission in-situ, with a tuning range and fine control limited only by the resolution of the actuator. Figure 5.8 shows the tuning of the TEM_{00} lasing mode from 619-651 nm, a range of 32 nm for which lasing was observed using the SAIT-1 sample. Note that between 619 and 644 nm we are able to select a pump power at which lasing occurs predominantly in the TEM_{00} mode (red). For the spectra in which the TEM_{00} is dominant, percentages are given for the fractional peak intensity of the second strongest mode ($TEM_{m+\ n\ =\ 1}$). When the TEM_{00} mode is tuned to wavelengths longer than 648 nm, higher transverse modes become dominant. This occurs because the minimum threshold of the transverse and the fundamental cavity modes spectrally

overlap at $\sim$ 641 nm as was shown in section 5.2.2. This means as the TEM_{00} mode moves away from the lasing minimum towards the red side it will be replaced by the next mode on the left ($TEM_{m+\,n\,=\,1}$). Since now the lasing threshold of this $TEM_{m+\,n\,=\,1}$ will be lower than the TEM_{00} mode it will begin to lase before the TEM_{00} and eventually dominate the spectrum. This allows the transverse modes to dominate the spectra for when the TEM_{00} mode is placed at spectral position beyond the 641 nm for any particular pumping power.

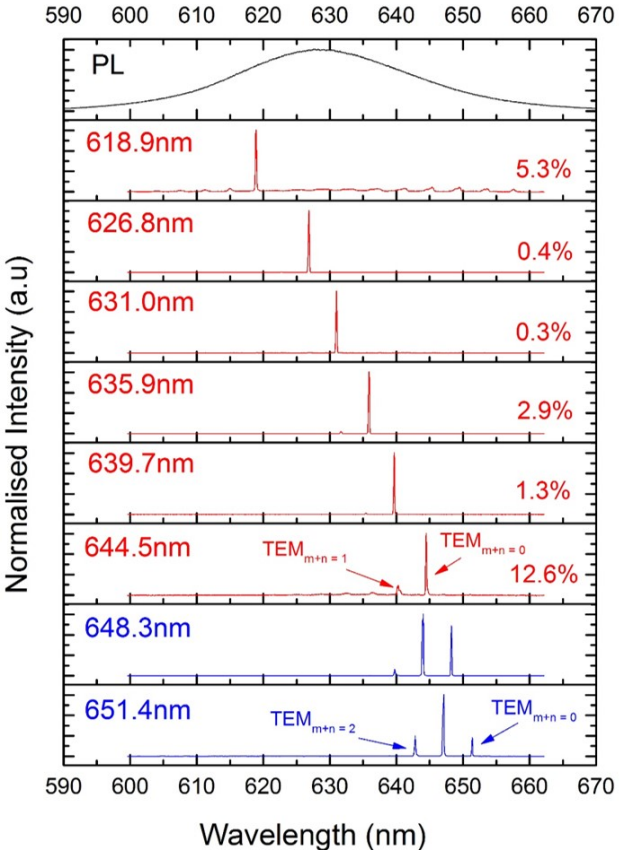

FIGURE 5.8: Tunable laser emission using the NCs. The percentage on the right shows the fractional peak intensity of the next dominant mode ($TEM_{\,m\,+\,n\,=\,1}$) compared to the peak intensity of the TEM_{00} for the spectra where the TEM_{00} is dominant (red). The normalised PL spectrum is also plotted for comparison.

5.3 Theoretical Analysis of the Gain Spectroscopy Results

In this section a theoretical model is derived to describe the results of gain spectroscopy. A rate equation model is initially proposed, but which is shown to have limitations resulting from the inhomogeneous broadening of the NCs. As a result, an analytically model is then proposed, which accurately describes lasing behaviour of the NCs.

5.3.1 Rate Equation Model

Here we present a set of semi-classical coupled differential rate equations that can be used to model the lasing behaviour of the NCs. As mentioned previously, we assume that the band-edge state for CdSe is two-fold degenerate. In this case, the rate equations describe the transitions between the ground state (S_0), the first excited state (S_1 i.e. a single exciton) and the second excited states (S_1 i.e. a biexciton), as shown in figure 5.9, and also govern the total number of photons (ϕ) contained in the cavity. These states have the total population with the cavity of N_0, N_1 and N_2, respectively. Note that from here on the state S_2 includes all the NCs that contain more than one exciton because in a two-fold degenerate emitting state the contribution to the band-edge emission from a given NC containing more than two excitons is the same as for a NC contain a biexciton. The total number of NCs within the cavity is then given by $N_{tot} = N_{conc} \times V_c = N_0 + N_1 + N_2$ where V_c is the physical mode volume calculated using the physical cavity length L_c (see equation 3.22) and N_{conc} is the NC concentration. Then, following the treatment detailed in section 3.7 the rate equations governing the NC populations for narrow-band radiation are given by:

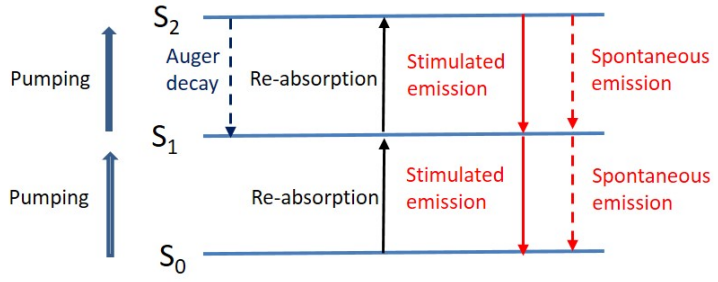

FIGURE 5.9: NC transitions. Schematic of the different transitions involved in the NC lasing process.

$$\frac{dN_0}{dt} = -P(t) - \overbrace{\frac{v_g \Gamma \sigma_{abs,01}}{V_c}\phi N_0}^{\text{re-absorption of laser photons from } S_0 \text{ to } S_1} + \overbrace{\frac{v_g \Gamma \sigma_{stm,10}}{V_c}\phi N_1}^{\text{stimulated emission from } S_1 \text{ to } S_0} + \overbrace{\frac{N_1({F_p}^{eff} + 1)}{\tau_{rad}}}^{\text{spontaneous emission from } S_1} \tag{5.4}$$

$$\frac{dN_1}{dt} = P(t) + \overbrace{\frac{v_g\Gamma\sigma_{abs,01}}{V_c}\phi N_0}^{\text{re-absorption of laser photons from } S_0 \text{ to } S_1} - \overbrace{\frac{v_g\Gamma\sigma_{stm,10}}{V_c}\phi N_1}^{\text{stimulated emission from } S_1 \text{ to } S_0} - \overbrace{\frac{N_1({F_p}^{eff}+1)}{\tau_{rad}}}^{\text{spontaneous emission from } S_1} + \underbrace{\frac{N_2}{\tau_{aug,bi}}}_{\text{Auger decay from } S_2} + \overbrace{\frac{v_g\Gamma\sigma_{stm,21}}{V_c}\phi N_2}^{\text{stimulated emission from } S_2 \text{ to } S_1} - \underbrace{\frac{v_g\Gamma\sigma_{abs,12}}{V_c}\phi N_1}_{\text{re-absorption of laser photons from } S_1 \text{ to } S_2} + \overbrace{\frac{4N_2({F_p}^{eff}+1)}{\tau_{rad}}}^{\text{spontaneous emission from } S_2} \tag{5.5}$$

$$\frac{dN_2}{dt} = P(t) - \overbrace{\frac{4N_2({F_p}^{eff}+1)}{\tau_{rad}}}^{\text{spontaneous emission from } S_2} - \underbrace{\frac{N_2}{\tau_{aug,bi}}}_{\text{Auger decay from } S_2} - \overbrace{\frac{v_g\Gamma\sigma_{stm,21}}{V_c}\phi N_2}^{\text{stimulated emission from } S_2 \text{ to } S_1} + \underbrace{\frac{v_g\Gamma\sigma_{abs,12}}{V_c}\phi N_1}_{\text{re-absorption of laser photons from } S_1 \text{ to } S_2} \tag{5.6}$$

$$\frac{d\phi}{dt} = \overbrace{\frac{4N_2({F_p}^{eff}+1)\Gamma\beta}{\tau_{rad}}}^{\text{spontaneous emission from } S_2} + \underbrace{\frac{N_1({F_p}^{eff}+1)\Gamma\beta}{\tau_{rad}}}_{\text{spontaneous emission from } S_1} + \overbrace{\frac{v_g\Gamma\sigma_{stm,21}}{V_c}\phi N_2}^{\text{stimulated emission from } S_2 \text{ to } S_1} + \underbrace{\frac{v_g\Gamma\sigma_{stm,10}}{V_c}\phi N_0}_{\text{stimulated emission from } S_1 \text{ to } S_0} - \overbrace{\frac{v_g\Gamma\sigma_{abs,12}}{V_c}\phi N_1}^{\text{re-absorption of laser photons from } S_1 \text{ to } S_2} - \underbrace{\frac{v_g\Gamma\sigma_{abs,01}}{V_c}\phi N_0}_{\text{re-absorption of laser photons from } S_0 \text{ to } S_1} - \overbrace{\frac{\phi}{\tau_{cav}}}^{\text{cavity decay rate}} \tag{5.7}$$

where $\tau_{aug,bi}$ is the biexciton Auger lifetimes, $\sigma_{abs,01}$ and $\sigma_{abs,12}$ are the absorption cross-sections of the states N_0 and N_1, respectively, at the emission wavelength. Similarly $\sigma_{stm,10}$ and $\sigma_{stm,21}$ are the stimulated emission cross-sections of the states N_1 and N_2, respectively, at the emission wavelength. Here we have defined β using the effective Purcell factor ${F_p}^{eff}$. This is because we assume that the homogenous linewidth of a single NCs is much bigger than intrinsic cavity linewidth at room temperature and also

that all the NCs at a specific wavelength are perfectly at resonance with the cavity mode ($\eta(\lambda) = 1$). We have assumed the carriers behave as free as opposed to bound excitons, which is true in the case of NCs where the confinement energy dominates and hence the radiative rate for the biexciton is set four times faster than the single exciton.

Equations 5.4 - 5.7 concern NCs resonant at a single emission wavelength. For particular set of NCs used in this experiment the ensemble FWHM is $\sim$ 33 nm whereas the single NC FWHM is $\sim$ 14 nm[146] at room temperature, indicating that the NC PL spectrum is inhomogeneously broadened. This means that the number of NCs in the ensemble change as a function of the spectral position and this can be difficult to incorporate into the above rate equations. Furthermore, for a cavity mode at any given spectral position there will be contribution to the absorbance from NCs that have their emission energy that is not resonant with the cavity mode because of the extended tail of the absorbance resulting from higher-order transitions. This is also very difficult to account for into the above equations. Therefore, incorporating such spectral dependence of the PL and absorbance into the rate equations such that they reproduce the observed variation in the NC threshold as a function of wavelength becomes difficult. It is for this reason an analytical model was derived which is an approximation to the dynamical system described above and will be now described in the following section.

5.3.2 Analytical Approach

We start by calculating the total number of photons spontaneously emitted into the cavity mode, N_{spt}, after a pulsed excitation:

$$N_{spt} = N_{cav}\left(1 - P(0)\right)\beta = N_{cav}\left(1 - e^{-\langle N\rangle}\right)\frac{{F_p}^{eff}}{{F_p}^{eff} + 1} \tag{5.8}$$

where $N_{cav} = AL_cN_{conc}$ is the total number of NCs coupled to the mode. N_{conc} is the concentration of the NCs, L_c is the physical cavity length, and $A = \frac{\pi\omega_0^2}{4}$ is the area of the mode at the planar mirror for which ω_0 is the mode waist. Thus, the physical mode volume (V_c) is defined by $A \times L_c$. Furthermore, ${F_p}^{eff}$ is the effective Purcell factor and we assume that all the NCs coupled the cavity mode are perfectly at resonance ($\eta(\lambda) = 1$). In equation 5.8 we have assumed that the NCs that contain more than one exciton are able to emit only a single photon due to the competing Auger process which quenches emission from multiexcitons. In other words, the NCs containing more than a single exciton contribute equally to the ones that contain a single exciton. The probability of a NC containing at least one exciton is given by $1-P(0)$, where $P(0)$ is the Poissonian probability that there are zero excitons per NC. This is then multiplied by

the factor β which takes into account the fraction of the photons emitted into a desired cavity mode.

The number of photons spontaneously emitted into the cavity mode within the gain lifetime, N_{spg}, is then given by:

$$N_{spg} = N_{cav}\left(1 - e^{-\langle N\rangle}\right)\frac{{F_p}^{eff}}{{F_p}^{eff}+1}\frac{\tau_g}{\tau_{rad}}\left({F_p}^{eff}+1\right) = N_{cav}\left(1 - e^{-\langle N\rangle}\right){F_p}^{eff}\frac{\tau_g}{\tau_{rad}} \tag{5.9}$$

where τ_g and τ_{rad} are the gain and the radiative lifetimes, respectively. Now we assume that the stimulated emission cross-section inside the cavity, σ_{stcav}, is time-dependent with the decay time governed by the gain lifetime:

$$\sigma_{stcav}(t) = \sigma_{st0cav}e^{-\frac{t}{\tau_g}} \tag{5.10}$$

where σ_{st0cav} is the cross-section at time $t = 0$. Since the photons take τ_g to be emitted into the mode the average stimulated emission cross-section of the NCs the photons encounter is:

$$\sigma_{stcav}(\tau_g) = \sigma_{st0cav}e^{-1} \tag{5.11}$$

The number of photons that they stimulate into the mode is therefore:

$$N_{vst} = N_{spg}\sigma_{st0}e^{-1}\frac{N_{cav}}{A}2F = N_{cav}^2\left(1 - e^{-\langle N\rangle}\right){F_p}^{eff}\frac{\tau_g}{\tau_{rad}}\sigma_{st0cav}e^{-1}\frac{2F}{A} \tag{5.12}$$

where the area A as defined previously is introduced here for normalisation and F is the finesse. The factor two comes because the finesse is equal to the number of round trips and the photons travel the length of the cavity twice per round trip. Note here than we have assumed the fact that the spontaneously emitted photons (N_{spg}) can stimulate emission from all of the NCs coupled to the cavity mode i.e.N_{cav}. In reality, however, we should replace N_{cav} with $N_{cav}(1 - P(0))$, which gives the total number of NCs coupled to the cavity mode that contain at least one exciton, and which are therefore able to undergo stimulated emission. However, we choose not to do this here as this will make the mathematically easier to arrive at an equation for the threshold, as will be seen later. Since the value of 1 - P(0) is close to unity, especially for $\langle N\rangle \geq 2$, which is close to minimum average exciton number we measure in our system at threshold, making such an approximation it is not expected to have a significant effect on the final result.

The lasing threshold is then defined when the total number of spontaneously emitter photons equals to those emitted by stimulated emission ($N_{spg} = N_{vst}$):

$$\begin{aligned} N_{cav}\left(1-e^{-\langle N\rangle}\right)\frac{{F_p}^{eff}}{{F_p}^{eff}+1} &= N_{cav}^2\left(1-e^{-\langle N\rangle}\right){F_p}^{eff}\frac{\tau_g}{\tau_{rad}}\sigma_{st0}e^{-1}\frac{2F}{A} \\ \implies \frac{1}{{F_p}^{eff}+1} &= N_{cav}\frac{\tau_g}{\tau_{rad}}\sigma_{st0}e^{-1}\frac{2F}{A} \end{aligned} \tag{5.13}$$

Furthermore, the cavity enhanced stimulated emission cross-section, σ_{stcav}, can be related to the free space stimulated emission cross-section, σ_{stfree}, as follows. As with the radiative rate the cross-section inside the cavity will be enhanced by the ratio of the optical DOS inside the cavity to free space in one dimension (Purcell factor). For a single cavity mode the DOS per unit energy is described by a normalised Lorentzian function, which at peak of the cavity mode gives the following:

$$DOS_{cav} = \frac{2}{\pi\Delta E} \tag{5.14}$$

where ΔE is the linewidth of the cavity mode. The DOS per unit length, DOS_{cavuni} , is then given by dividing equation 5.14 by the cavity length:

$$DOS_{cavuni} = \frac{2}{\pi\Delta E L} = \frac{2Q}{\pi E L} = \frac{2Q}{\pi\hbar c k L} \tag{5.15}$$

where we have utilized the fact that the Q-factor is given by $\frac{E}{\Delta E}$ where E is the energy at resonance of the cavity mode and also the relation $E = \hbar ck$. In free space the separation between the k-states is given by $\frac{\pi}{L}$ then the DOS in k-space is simply $\frac{L}{\pi}$. Then using the relation $E = \hbar ck \rightarrow dE = \hbar cdk$ the DOS in per unit energy per unit length is given by:

$$DOS_{freeuni} = \frac{1}{\pi\hbar c} \tag{5.16}$$

Finally, taking the ratio of the cavity and the free space DOS gives:

$$\frac{DOS_{cavuni}}{DOS_{freeuni}} = \frac{2Q}{kL} = \frac{2}{\pi}\frac{Q\lambda}{2L} = \frac{2}{\pi}\frac{Q}{q} = \frac{2}{\pi}F \tag{5.17}$$

where q is the mode number. We can now relate the free space stimulated emission cross-section to the cavity enchanced cross-section as $\sigma_{stcav} = \frac{2}{\pi}F\sigma_{stfree}$. Thus, equation 5.13 becomes:

$$\frac{1}{{F_p}^{eff}+1} = N_{conc}L_c\frac{\tau_g}{\tau_{rad}}\sigma_{stfree}e^{-1}\frac{4}{\pi}F^2 \tag{5.18}$$

where we have used $N_{cav} = AL_cN_{conc}$. The gain relaxation time, τ_g, can be related to the Auger lifetime using the "cascade" idea. If one were to assume that the Auger lifetimes were independent of $\langle N\rangle$, then we have:

$$\tau_g = (\langle N\rangle - 1)\,\tau_{aug,bi} \tag{5.19}$$

where $\tau_{aug,bi}$ is the biexciton Auger lifetime. The idea here is that the gain lifetime is prolonged as the number of carriers increase. This is because in an event of Auger recombination of one of the pairs of carriers they will be rapidly replaced by the ones that are higher up in energy. This effectively then prolongs amount of time at least a biexciton remains inside a NC, which is required to achieve lasing, and thus extends the gain lifetime. However, we also know that the Auger lifetime decreases with the number of carriers present[9], so a better relationship might be:

$$\tau_g = \sqrt{\langle N\rangle - 1}\tau_{aug,bi} \tag{5.20}$$

Furthermore, we can relate the excitation energy in energy per pulse, E_p, to $\langle N\rangle$ via equation 5.3 and arrive at the analytical threshold equation:

$$E_p = \frac{\hbar\omega A_{exc}}{T\sigma_{400nm}}\left[\left(\frac{2.7\pi\tau_{rad}}{4\tau_{aug,bi}({F_p}^{eff}+1)N_{conc}L_c\sigma_{stfree}F^2}\right)^2+1\right] \tag{5.21}$$

where we have approximated e $\sim$ 2.7. In order to reproduce the measured gain profile we normalised the PL and the absorbance (at the first absorbance peak) and subtract the absorbance from the PL (PL - ABS). This is shown in figure 5.10 and gives the fraction of the photons are emitted into the cavity mode or when this factor is multiplied with σ_{stfree} can be thought of as the "net" stimulated emission cross-section for the NC ensemble.

We then arrive at the equation for the threshold:

$$E_p = \frac{\hbar\omega A_{exc}}{T\sigma_{400nm}}\left[\left(\frac{2.7\pi\tau_{rad}}{4\tau_{aug,bi}({F_p}^{eff}+1)N_{conc}L_c\sigma_{stfree}(PL-ABS)F^2}\right)^2+1\right] \tag{5.22}$$

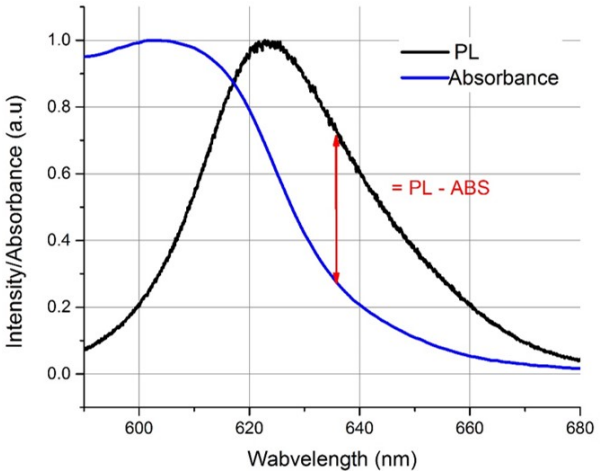

FIGURE 5.10: Net stimulated emission cross-section. The procedure for calculating the "net" stimulated emission cross-section by subtracting the normalised absorbance (normalized at the first absorbance peak) from the normalised PL.

However, the above method has a limitation as the "net" stimulated emission goes to zero at the point where the normalised PL and absorbance cross (at around 620 nm in figure 5.10), which off course is not true in reality. Therefore, in order to circumvent the problem we introduce two additional parameters, A and B, in equation 5.22 to arrive at the final threshold equation:

$$E_p = \frac{\hbar\omega A_{exc}}{T\sigma_{400nm}}\left[\left(\frac{2.7\pi\tau_{rad}}{4\tau_{aug,bi}({F_p}^{eff}+1)N_{conc}L_c\sigma_{stfree}(A*PL-B*ABS)F^2}\right)^2+1\right] \tag{5.23}$$

The idea is to change the A and B parameters between zero and unity in equation 5.23 to get a good fit to the experimental data, as will be seen later. Also notice that there is no inclusion of the QY of the NCs in the equation 5.22, which for the NCs (for both SAIT-1 and 2) was measured to be $\sim$ 60 %. To justify this we can argue that for moderately well passivated (7 ML shell) NCs like the ones used in this experiment the dominant contribution to the non-radiative processes comes from the Auger process (as opposed to carrier trapping at surface states) and this process has already been incorporated in to the threshold equation. Table 5.1 gives the values of all the physical quantities used in equation 5.22 for the experiment described in section 5.2.3 for the SAIT-2 samples for which the optimal alignment was achieved.

The ensemble radiative lifetime is measured using method described in section 4.2.1. The TRPL spectrum is shown in figure 5.11a. The spectrum is well described with a tri-exponential of the form:

$$y(t) = y_0 + A_1 e^{-\frac{t-t_0}{t_1}} + A_2 e^{\frac{t-t_0}{t_2}} + A_3 e^{\frac{t-t_0}{t_3}} \tag{5.24}$$

here y_0 is the background count, A_1, A_2 and A_3 are amplitude of the respective components and t_0 are the time offsets form the zero. The lifetime with the strongest component was $\tau_2 = 35.7$ ns with $A_2 = 25216$ and can be attributed to emission from single excitons. The other two components had lifetimes of $\tau_1 = 13.2$ and $\tau_3 = 86.4$ with amplitudes $A_1 = 3990$ and $A_3 = 757$. These components are mostly likely related to the charging of the NCs and since they are only 15.8% (A_1) and 3% (A_3) of the single exciton lifetime component they will not contribute significantly to the radiative emission of the NCs.

The Auger lifetime was measured using pump-probe spectroscopy outlined in section 4.2.3. Figure 5.11b shows the plots of the normalised differential transmission ($\frac{dT}{T_{grd}}$) as a function of the delay between the pump (400 nm excitation) and the probe with progressively higher pumping powers. The probe wavelength was set to 610 nm, which is at the first peak of the absorbance curve and therefore probes the band-edge state. As can be seen, as the pumping power is increased an initial fast component develops on top of the much slower component at lower pumping powers. Since the samples were stirred during the measurement to avoid the formation of trions the rise of the initial faster component can safely be attributed the Auger decay of biexcitons. The longer component, which forms the background, is then due to the radiative decay of single excitons. The Auger lifetime was extracted by initially fitting a single exponential to the curve with the lowest pumping power (orange) to extract the longer lifetime. Then by fitting a bi-exponential to the curve with the highest pumping power (black) and fixing one of the lifetimes to that measured previously a biexciton lifetime of 189 ps was extracted.

The concentration is measured using the method outlined in section 4.6 and was 4.8 $\times$ 10^{23} m^{-3}, giving a packing density of $\sim$ 21 % by volume. The NCs are assumed to be in the bad-emitter regime and following the paper by Ziyun et al[146] the effective Q-factor was set to 45, giving ${F_p}^{eff}$ equal to 0.02. To calculate the latter the refractive index of $n = 1.7$ was used and was calculated using the following equation:

$$n = n_{eff} V_{NC,frac} + n_{oct} V_{oct,frac} \tag{5.25}$$

where $n_{eff} = \frac{V_{CdSe}}{V_{tot}} n_{CdSe} + \frac{V_{CdS}}{V_{tot}} n_{CdS}$ is the effective refractive index of CdSe/CdS for which $V_{CdSe/CdS}$ and $n_{CdSe/CdS}$ are the volumes and the refractive indices (for $\sim$ 600-640 nm)[164] of the core and the shell, respectively. $V_{NC,frac/oct,frac}$ are the fractional

volumes of the NCs and Octadecane contained in the solution and n_{oct} is the Octadecane refractive index at the lasing wavelength.

The finesse is re-absorption limited and is taken as a mean value averaged over all spectral positions for which the lasing threshold was measured. These parameters are summarised in table 5.1. However, the value of the free space stimulated cross-section for CdSe was uncertain. Therefore, this parameter was varied until the theoretical fit was consistent with the experimental data. This is shown in figure 5.12a (grey lines), where the cross-section is varied from a value of 3×10^{-20} m^2 to 8×10^{-20} m^2. A best fit to the data is found for a value of 4.3×10^{-20} m^2. This is a factor of 22 times bigger than the value of 2×10^{-21} m^2 quoted for core-only CdSe by Klimov et al [82]. However, the radius of the CdSe NCs in the quoted paper[82] is almost twice as small (1.3 nm) as the core radius of NCs use in this experiment (2.1 nm) and that without taking into account the additional layer due to the shell. Thus, we are able to justify the large value of the cross-section to the bigger physical size of the NCs we use in this experiment. This argument is consistent with Schafer et al[165] where lasing from spherical liquid micro-droplets formed from a solution of core-shell CdSe/ZnS NCs was observed at packing densities 33 times lower than that predicted by condition given by equation 2.2 using the stimulated emission cross-section quoted by Klimov et al [82]. In order to satisfy this condition Schafer et al[165] et al predicted that the stimulated emission must increase by at least 23 times due to the larger size of the NCs used in the experiment (core radius 2.6 nm).

Furthermore, there will also be some degree of error in the concentration of the NCs from the measured value of 4.8×10^{23} m^{-3} and also the Purcell factor. Since both the free space stimulated emission cross-section and the concentration are products in equation 5.22 varying the concentration (for all other parameters fixed) will have the same effects as for the stimulated emission cross-section, which the best fit value given by 4.2×10^{-20} m^{-3}. Varying the Purcell factor, however, will have a insignificant effect on the curve since the its value is small in the first place and the factor ${F_p}^{eff} + 1$ is equation 5.22.

However, it can be seen from figure 5.12a that the theoretical threshold fit diverges very rapidly at it approaches the blue side (less than 622 nm) whereas the experimental values do not. This is because we have set the A and B parameters in equation 5.23 equal to unity and thus the PL and the absorbance values are equal in magnitude at 620 nm, meaning that the $PL - ABS$ term approaches zero in equation 5.23 at around 620 nm, making the threshold value infinite at this point (i.e. implying zero "net" stimulated emission at 620 nm). Therefore, it was found that by setting $A = 0.92$ and $B = 0.72$, a better fit to the experimental data can be obtained for the case where $\sigma_{stfree} = 4.3 \times 10^{-20}$, as seen in figure 5.12b.

Excitation spot area, A_{exc}	3.3×10^{-11} m^2
Transmission, T	0.97
Absorption-crossection, σ_{400nm}	4×10^{-18} m^2
Radiative lifetime, τ_{rad}	35.7 ns
Biexciton Auger lifetime, $\tau_{aug,bi}$	189 ps
Effective Purcell factor, $F_p{}^{eff}$	0.02
Concentration, N_{conc}	4.8×10^{23} m^{-3}
Cavity Length, L_c	1.2 μm
Free space stimulated emission cross-section, σ_{stfree}	4.3×10^{-20} m^2
Finesse, F	197
Refractive index, n	1.7

TABLE 5.1: Summary of the parameters used in the NC rate equation model.

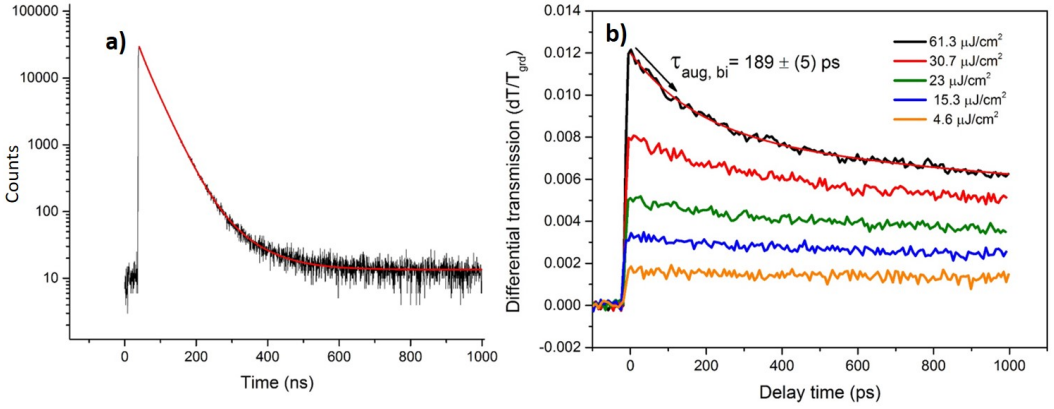

FIGURE 5.11: NC radiative and Auger lifetimes. a) An ensemble time resolved photoluminescence spectrum for SAIT-2, with counts plotted logarithmically. b) Time transients of NCs at various pumping powers. The sample was excited at 400 nm. The probe wavelength was at 610 nm.

It was mentioned previously that the gain profile of the NCs is governed by the competition between stimulated emission and absorption as well the by the biexciton binding energy. The derivation of the threshold equation in section 5.3.2 does not include any Coulomb interactions between the excitons yet we still get a good fit to the experimental data. Thus, we argue that in our system the governing process that determines the gain profile is the interplay between the stimulated emission and the re-absorption of the photons and the biexciton binding energies play a negligible role.

5.4 Conclusion

The results of gain spectroscopy of solution based CdSe/CdS spherical NCs has been presented. The open access design of the cavity provides a convenient method for the direct investigation of the lasing behaviour of NCs enabled via in-situ tuning of the cavity feedback wavelength.

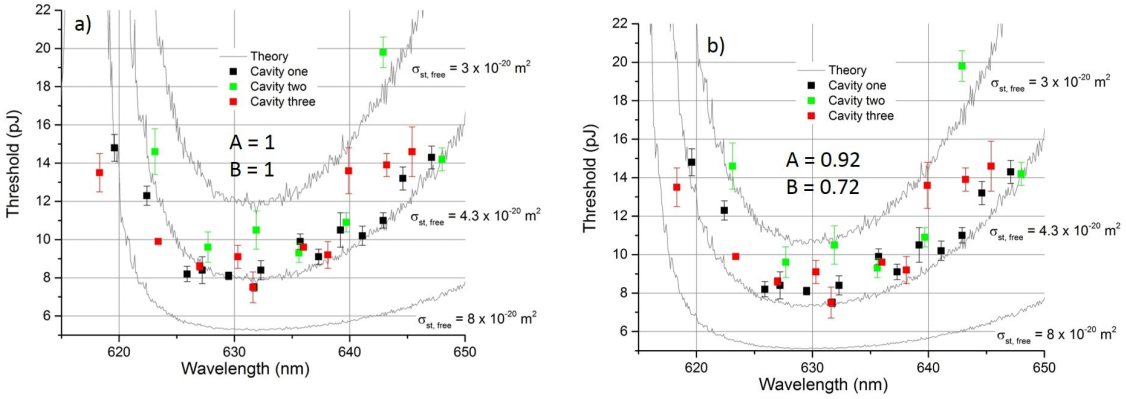

FIGURE 5.12: Theoretical fits to the experimental thresholds for different cavities (with the same RoC). A) Fits in the case where the A and B parameters are set to unity. B) Fits in the case where the $A = 0.92$ and $B = 0.72$.

The lasing process was found to be the most efficient (lowest lasing thresholds) at a spectral positon which is red-shift with respect to the ensemble PL curve. Moreover, the average exciton number at the minimum lasing threshold was measured to be$\sim$ 1.4, indicating a biexciton lasing mechanism consistent with type-I structures. Comparison of the magnitude and the trend in the Q-factor as function of wavelength between an empty and for a cavity filled with NCs revealed that the Q-factors of the latter were in fact re-absorption limited. Thus, any influence from the changes in the reflectivity of the mirrors as the mode moves across the stop-band on the results of the gain spectroscopy was ruled out. A consequence of this is that lasing thresholds cannot be improved by the using a cavity of higher reflectivity as the re-absorption of the lasing photons by the NCs is the dominant loss mechanism inside the cavity. Furthermore, the NC solution within the cavity experience no change in temperature or stress during tuning and so the changes in lasing performance can be attributed unambiguously to the change in feedback wavelength. A rate equation model was proposed to describe the result of the gain spectroscopy, but was found to have limitation due to the size polydispersity of the NCs. Therefore, an alternative model was proposed which was an analytic approximation to the dynamical system. By comparing the results of the gain spectroscopy to the analytical model it was found that the factor governing the shape of the gain profile was the interplay between the stimulated emission and self-absorption of the lasing photons.

From a technological standpoint, the results demonstrate a new approach to widely tunable single mode lasers for chip-scale and low power applications. The capability to change the feedback wavelength enabled tunable laser emission from the fundamental cavity mode for a total range $\sim$ 32 nm and single mode lasing for a range of $\sim$ 25 nm. Furthermore, a threshold intensity of $\sim$ 23 μJ cm^{-2} was measured, which is 100-200 times smaller than those previously reported in type I systems[159, 163] and lower than those reported for lasing in the single exciton regime ($\sim$ 60 μJ cm^{-2})[113]. This could

be the result of the high absorption cross-section at the excitation wavelength due the thick (7 ML) CdS shell, a high packing density (21%) and/or a high gain cross-section due to the large physical size of the NCs.

Chapter 6

Gain Spectroscopy of CdSe/CdS Nanoplatelets

6.1 Introduction

This section presents the results of gain spectroscopy of solution based CdSe/CdSe core-shell spherical NPs using tunable open access microcavities. The quantum well geometry offers several advantages compared to the spherical NCs in terms of optical gain performance. This includes suppressed Auger rates as a result of one dimensional quantization[16], which imposes a stricter momentum conservation rule for the process, and higher gain cross-sections due to the large exciton binding energies and the Giant oscillator strength (GOST) effect[18, 99]. Furthermore, they also offer a higher gain coefficients due to multiple excitons of the same emission energy occupying single NPs as well as high absorptions coefficients due to their larger physical size.

Just like in the case of NCs the lasing threshold and differential gain are measured as a function of the cavity length. Tunable and single mode lasing is demonstrated and the stability of the laser (how long lasing can be sustained) is investigated, which ultimately depends on the quality of the NPs (the degree of passivation, number of defects etc.). A rate equation model is proposed to simulate the NP lasing dynamics and which accurately describes the results of the gain spectroscopy.

6.2 Nanoplatelet Lasing Experiments

This section describes the lasing experiments using CdSe/CdS core-shell NPs, which were provided by our collaborators at the Italian Institute of Technology (IIT). The

nominal core NP dimensions are $\sim 44 \times 8 \times 1.35$ (nm). The core is encapsulated with a CdS shell of thickness ~ 0.7 nm (2 ML), giving the total core-shell dimensions of $\sim 45.4 \times 9.4 \times 2.75$ (nm), as shown in figure 6.1. They are coated with oleic acid ligands. As with NCs, the NP sample was prepared using the method outlined in section 4.3. The experimental set-up is described in section 4.4 and in all the lasing experiments the focus was on the lasing behaviour of the fundamental cavity mode (TEM_{00}).

All the experiments were conducted using cavities with mirrors consisting of 20 pairs of alternating SiO_2/TiO_2 and with nominal RoC = 25 μm. This is in contrast with the NCs where mirrors consisting of only 10 pairs were used. Here the idea was to increase the finesse of the cavity to achieve lower lasing thresholds. However, this was before realisation that finesse in our system is governed by the re-absorption of the lasing photons and not the cavity reflectivity (see figure 5.3). Since this also expected to apply in the case of NPs the results of gain spectroscopy are expected to be independent of the intrinsic cavity finesse.

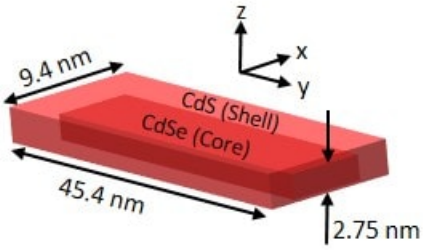

FIGURE 6.1: Schematic showing the full (core and shell) dimensions of the NPs (note ligands are not included for clarity).

6.2.1 Power Dependence Measurements

Power dependence measurements were conducted using the PicoQuant P-C-450B diode laser with the pulse width of less than 100 ps (minimum 68 ps) capable of delivering 125 pJ per pulse. The repetition rate was set to 5 MHz, which prevented the photo-bleaching of the NPs.

Figure 6.2a shows the emission spectra below (blue) threshold with the TEM_{00} (with mode number q) located at 684 nm. Multimode laser emission is visible as the pumping power is increased (green) where lasing from up to the $TEM_{m+\,n\,=\,3}$ transverse mode can be clearly seen. Figure 6.2b shows the integrated intensity as a function of pumping power on a log-log scale for the same TEM_{00} mode located at 660 nm (blue) and at 684 (red), tuned into position by changing the cavity length. The graphs display lasing with the threshold of 9 pJ (660 nm) and 23 pJ (684 nm). However, the characteristic kinks in the power dependence curves are not accompanied by a notable collapse in the mode

linewidth as would be expected in the lasing regime. The reason for this anomaly is not certain, although one possibility that the spectrometer slits may not be adequately closed, meaning that the resolution of the modes is compromised.

Therefore, in order to confirm that we are in the lasing regime the spectra for the TEM_{00} mode located at 660 nm are compared below and above threshold. To do this the TEM_{00} mode is normalised in both cases and the spectra are plotted on top to each other as shown in figure 6.2c. It can be clearly seen that in comparison to the spectrum below threshold, in the above threshold transverse mode intensity is greatly reduced in comparison to the TEM_{00} mode. This indicates a highly non-linear increase in the intensity of the TEM_{00} mode which is expected in the lasing regime. In order to accurately determined the lasing threshold a linear least squares fit is made to the power dependence curve on a log-log scale, both above and below the threshold as shown in figure 6.2b. The lasing threshold is then the value at which the two lines intersect. It can also be seen that the onset of lasing is accompanied by a blue-shift of the modes by ~ 1 nm. This shift is perhaps result of the carrier-induced refractive index change within the NPs. More importantly, the blue-shift was found to be reversible with pumping power and was not accompanied by the decrease in the emission intensity of the lasing mode (as can be seen from figure 6.2b, ruling out photo-bleaching of the NPs. An important remark to make here is that lasing in NPs could be achieved with picosecond excitation source.

It should be noted in some of the cavities fabrication imperfections break the rotational symmetry of the hemispherical mirrors making them slightly elliptical i.e the mirrors have a slightly different RoC along the two principle axes. As a result the two-fold polarisation degeneracy of modes is lifted causing a splitting of the modes[166]. This is seen clearly in an example spectra in figure 6.2d (top) in the case of TEM_{00} mode (and also in transverse modes) and was the case with the cavity use in the NP lasing experiment. Thus, by using a circular polariser one of the polarisation components (the one that is not preferentially selected for lasing) for the TEM_{00} was eliminated, as seen in figure 6.2d (bottom). This then gives us the ability to produce single mode lasing without the interference form the other polarisation component, as will be shown later in the chapter.

6.2.2 Gain Spectroscopy

The lasing threshold of the cavity modes as a function of their wavelength can be extracted by tuning the cavity length. Figure 6.3a displays the lasing threshold as a function of spectral position for the TEM_{00} for a range of ~ 42 nm. The full ensemble

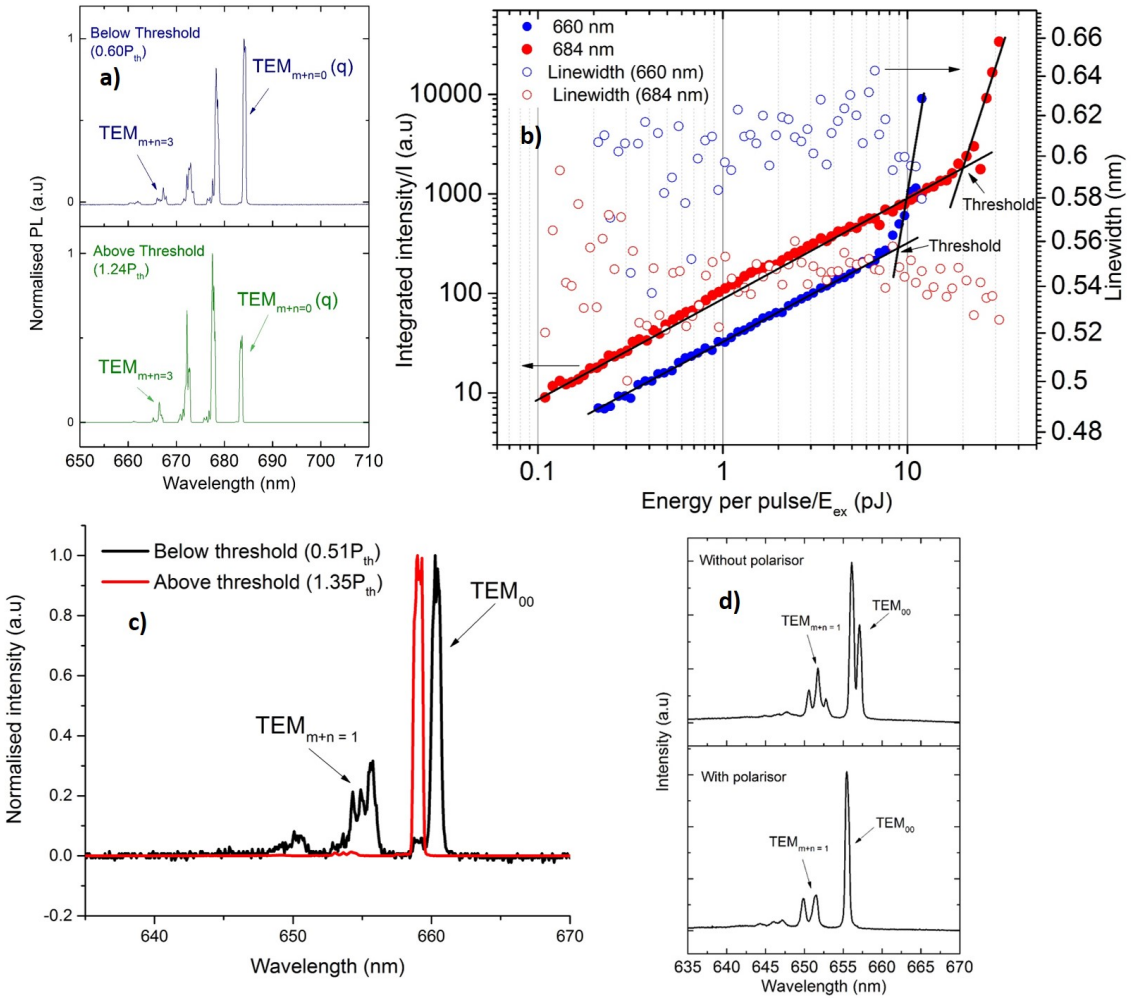

FIGURE 6.2: NP lasing. (a) Spectra below and above threshold at pump energies of $0.60P_{th}$ and $1.24P_{th}$ (450 nm excitation), respectively, and where P_{th} is the threshold energy per pulse. Multi-mode laser emission (from $TEM_{m+\,n\,=\,0}$ to $TEM_{m+\,n\,=\,3}$) can be seen above threshold. b) Threshold behaviour from the fundamental cavity mode at two different spectral positions (660 nm and 684 nm), along with the linewidths. c) Normalised spectra below ($0.51P_{th}$, black) and above ($1.35P_{th}$, red) threshold showing a non-linear increasing in the emission intensity of the $TEM_{m+\,n\,=\,0}$ mode due to stimulated emission. d) Spectra with (top) and without (bottom) using a circular polariser to block one of the polarisation components for the $TEM_{m+\,n\,=\,0}$ mode.

PL and absorbance spectra are shown in figure 6.3b. As seen there is a minimum lasing threshold at $\sim$ 664.9 nm with the value of 8.84 ($\pm$ 3) pJ per pulse and which is red-shifted by 25 nm with respect to the ensemble PL peak position. The position of the lasing minimum coincides with a maximum in the differential gain, $\zeta = \frac{dI}{dE_{ex}}$, indicating a spectral position were the lasing process is the most efficient.

The differential gain is extracted simply by performing a linear least square fit of the power dependence curve above threshold on a linear-linear scale. This is in contrast to the NCs where the integrated intensity was initially normalised and was then plotted as a function of the average exciton number and the differential gain then extracted. The

reason for this can be found by comparing power dependence curve of the NCs in figure 6.3c (same as in figure 5.4a in chapter 5) to the one for NPs in figure 6.3d for the TEM_{00} located at 660 nm. For the NCs clear saturation behaviour is observed below threshold which is the result of the multiexcitonic Auger process. This is in contrast to the NPs where the integrated intensity increases linearly until the onset of lasing. This strongly suggests that, unlike NCs, there is efficient emission from multiexcitons (assuming that for NCs lasing occurs from multiexcitons) indicating a marked suppression of the Auger process. However, for this reason a calibration of the energy axis in terms $\langle N_{th} \rangle$ was not possible.

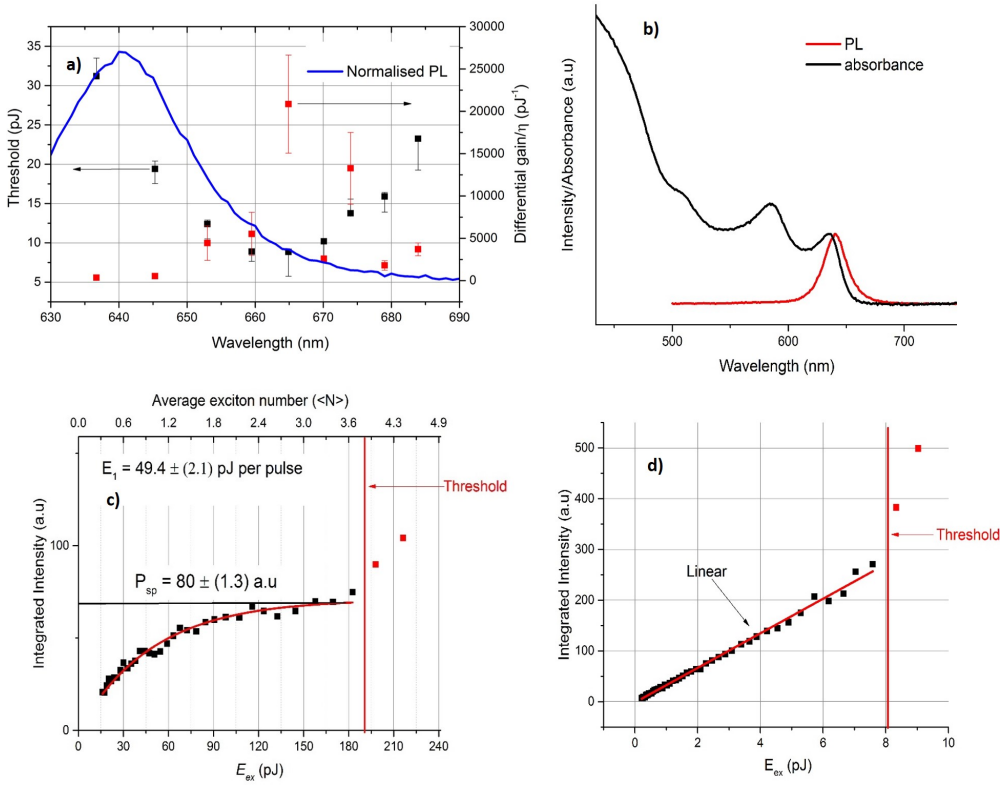

FIGURE 6.3: NP gain spectroscopy. (a) A plot of the lasing threshold and differential gain as a function of spectral position for the TEM_{00} mode along with the ensemble PL spectrum. b) Extended ground state absorbance (normalised at the first absorbance peak) and the normalised PL spectrum. c) Evolution of the integrated emission intensity for the NCs below threshold. d) Evolution of the integrated emission intensity for the NPs below threshold.

6.2.3 Tunable Lasing and Laser Stability Measurements

Tunable laser emission from the NPs was demonstrated by changing the cavity length. Figure 6.4 shows emission spectra above threshold with the cavity modes tuned by as much as 47 nm. Between 636-674 nm we were able select the pumping power at which lasing occurs predominantly in the TEM_{00} mode (highlighted in red). For these spectra

the percentages show fraction of the peak intensity of the $TEM_{m+\ n\ =\ 1}$ mode compared to the TEM_{00} mode. As with the NCs, once the TEM_{00} goes past the positon of the lasing minimum (664.9 nm) the transverse modes begin to dominate as their lasing minimum is also expected to be at the same spectral position. This places a limit for which single mode lasing is achieved at higher wavelengths.

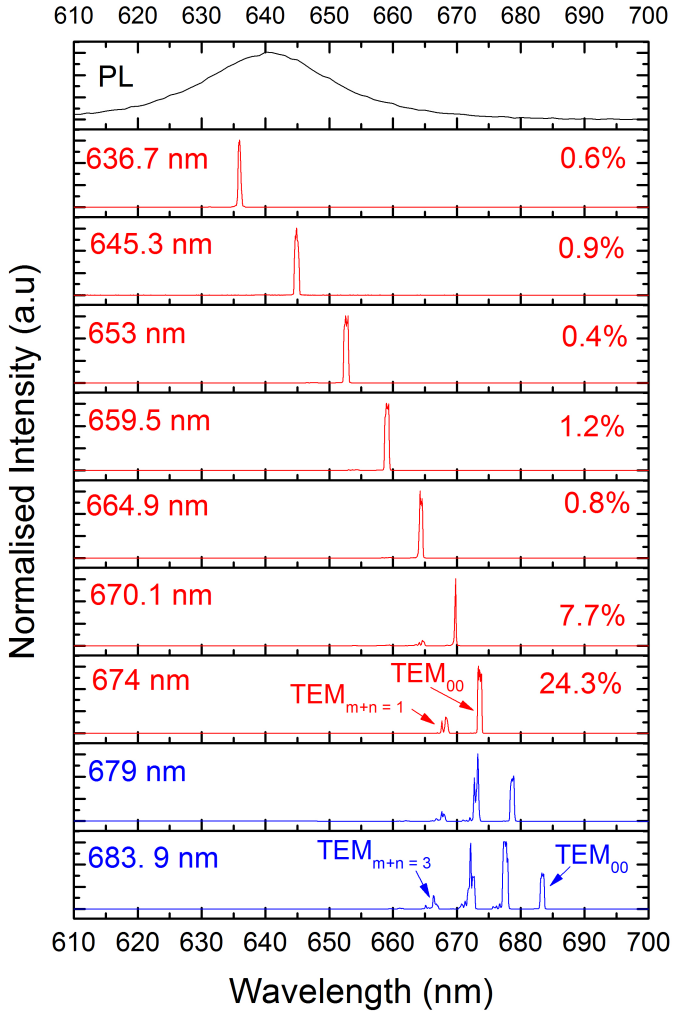

FIGURE 6.4: Tunable laser emission using the NPs. Tunable laser emission is demonstrated by changing the cavity length. The percentage on the right shows the fractional peak intensity of the next dominant mode ($TEM_{\ m\ +\ n\ =\ 1}$) compared to the peak intensity of the TEM_{00} for the spectra where the TEM_{00} is dominant (red). The normalised PL spectrum is also plotted for comparison.

We further investigated the period of time lasing can be sustained by monitoring the intensity of the TEM_{00} as a function of time. Figure 6.5a shows a plot of the integrated intensity of the TEM_{00} mode located at 662.5 nm as a function of time above threshold (pump power of $5P_{th}$ at 450 nm with the repetition rate of 5 MHz). The integrated intensity of the mode remains stable for almost $\sim$ 354 seconds ($\sim$ 6 mins or almost 1.8

$\times 10^9$ consecutive laser pulses) before gradually decreasing until it reaches below 20 % of the initial value ($\sim$ 6000), at which point the data acquisition was stopped. The decrease in the emission intensity can be caused by charging and/or photo-bleaching of the NPs. Further insight can be obtained by looking at figure 6.5b which displays a 2-D plot of intensity of the mode as a function of time. It can be seen that there is no spectral drift of the cavity mode even after the point in time when the lasing intensity starts to decrease at around 354 seconds (the mechanical drift in this experiment was found to be minimal hence there was no need to adjust the cavity length using the actuator). This indicates that the decrease in the intensity is most likely caused by charging of the NPs over time, as photo-bleaching is usually accompanied by a blue-shift of the emission wavelength[156]. Thus, the lasing performance could be improved further by adding more shells to the NPs, which is known to reduce charging of the cores. Using a camera (Canon 6d DSLR) the laser emission (multimode) can also be seen with a 30 second exposure. This is shown in figure 6.5b where the image of the laser emission is located at the spectrometer entrance slit.

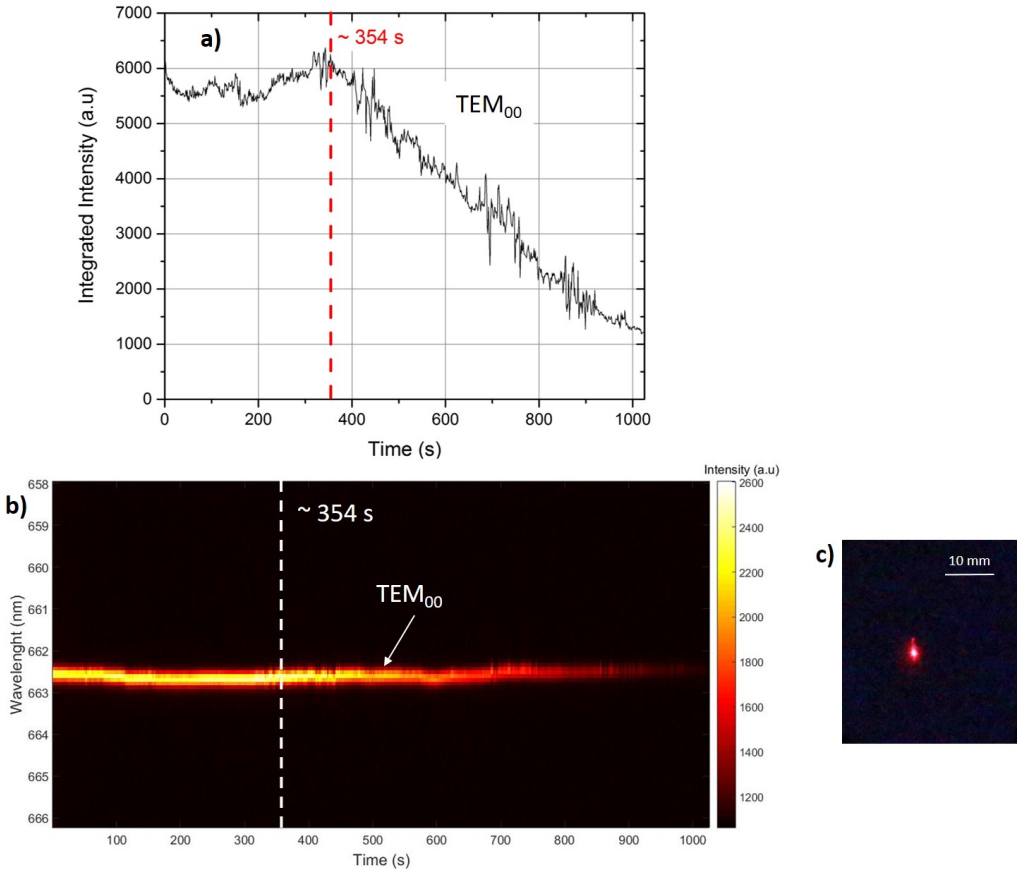

FIGURE 6.5: Laser stability experiment. a) A plot of the integrated emission intensity of the TEM_{00} at 662.5 nm as a function of time. b) 2-D plot of the TEM_{00} as a function of time. c) Visible laser emission (in the multimode regime) located at the spectrometer slit (30 second exposer).

6.3 Rate Equation Model

In this section a rate equation model is proposed in order to reproduce the lasing behaviour of the NPs presented in section 6.2.2. In the previous chapter it was highlighted that using a rate equation model in the case of NCs has its limitation due to the sample inhomogeneity. However, NPs can be synthesised with the thickness that is controlled to atomic precision. Since their emission energy is dictated by their thickness (the quantization of energy levels is only in this dimension) spectral broadening due to sample inhomogeneity can be greatly reduced such that their ensemble emission linewidth can be equal to the single NP linewidth within the ensemble at room temperature[167]. In the same way the ensemble absorption spectra can be treated as if it was due to a single NP. These features make these variables (PL and absorption) a lot easier to be integrated into the rate equation model.

Following the rate equation treatment described in section 3.7, we describe our NP ensemble system by two sets of coupled differential equations governing the total number excitons (N_{exc}) and photons (ϕ) in the physical cavity mode volume (V_c):

$$\frac{dN_{exc}}{dt} = P(t) + \underbrace{\frac{v_g \Gamma \sigma_{abs}(\lambda) \phi N_{tot}}{V_c}}_{\text{re-absorption of laser photons}} - \overbrace{\frac{v_g \Gamma \sigma_{stm} \phi N_{exc}}{V_c}}^{\text{stimulated emission}} - \underbrace{\frac{N_{exc}({F_p}^{eff} + 1)}{\tau_{rad}}}_{\text{spontaneous emission}} \tag{6.1}$$

$$\frac{d\phi}{dt} = \underbrace{\frac{N_{exc}\Gamma({F_p}^{eff} + 1)}{\tau_{rad}}\beta}_{\text{spontaneous emission}} + \overbrace{\frac{v_g \Gamma \sigma_{stm} \phi N_{exc}}{V_c}}^{\text{stimulated emission}} - \underbrace{\frac{v_g \Gamma \sigma_{abs}(\lambda) \phi N_{tot}}{V_c}}_{\text{re-absorption}} - \overbrace{\frac{\phi}{\tau_{cav}}}^{\text{cavity decay}} \tag{6.2}$$

where N_{tot} is the total number of NPs within the cavity mode volume and σ_{abs} is the absorption cross-section. Note that above we have used the effective Purcell factor ${F_p}^{eff}$ as the single NP linewidth (also equal to the ensemble linewidth) at room temperature is much larger than the intrinsic cavity linewidth. Furthermore, we have assumed unsaturable absorption of the photons at the emission wavelength such that the probability of a photon absorption event is independent of the number of excitons already inside the NP. This is consistent with the fact that several excitons of the same emission energy can occupy a single NP[69, 135]. The temporal profile of the pulsed excitation laser can be described using a Gaussian function of the form quoted by equation 3.56.

Moreover, it is assumed that the Auger process is suppressed such that it does not strongly compete with multiexcitonic radiative emission and is thus not included in the rate equations. This is consistent with the linear evolution of the emission intensity of the modes below threshold (figure 6.3). In this case, the QY (which is included in the pumping term) will be governed by the trapping of the carriers at surface defects.

Finally, the total exciton number can be related to the average exciton number, $\langle N \rangle$, using the relation $N_{exc}/N_{tot} = \langle N \rangle$ such that equation 6.1 can now be written in terms of $\langle N \rangle$. The latter makes solving the rate equations computationally less intensive. Equations 6.1 and 6.2 then become:

$$\frac{d\langle N \rangle}{dt} = \overbrace{\frac{\varsigma T G(t) spat(\omega_0)\left(1 - e^{-\frac{\sigma_{450nm} N_{conc} L_c}{T}}\right)}{N_{tot}}}^{\text{pumping term}} + \underbrace{\frac{v_g \Gamma \sigma_{abs}(\lambda)\phi}{V_c}}_{\text{re-absorption}} - \overbrace{\frac{\Gamma\phi\langle N \rangle {F_p}^{eff}\eta(\lambda)}{\tau_{rad}}}^{\text{stimulated emission}} - \underbrace{\frac{\langle N \rangle({F_p}^{eff}\eta(\lambda) + 1)}{\tau_{rad}}}_{\text{spontaneous emission}} \tag{6.3}$$

$$\frac{d\phi}{dt} = \underbrace{\frac{N_{exc}\Gamma {F_p}^{eff}\eta(\lambda)}{\tau_{rad}}}_{\text{spontaneous emission}} + \overbrace{\frac{\Gamma\phi N_{exc} {F_p}^{eff}\eta(\lambda)}{\tau_{rad}}}^{\text{stimulated emission}} - \underbrace{\frac{v_g \Gamma \sigma_{abs}(\lambda)\phi N_{tot}}{V_c}}_{\text{re-absorption}} - \overbrace{\frac{\phi}{\tau_{cav}}}^{\text{cavity decay}} \tag{6.4}$$

In the above equations we have assumed that excitons are strongly bound at room temperature resulting in a linear dependence of the radiative and stimulated emission terms with respect to $\langle N \rangle$. This is consistent with the fact that the exciton binding energy in NPs is predicted to be an order of magnitude larger than their thermal energy at room temperature[18]. If the carriers were treated as free (as in the case of spherical CQDs where quantum confinement dominates), then the radiative and stimulated emission terms would scale quadratically with respect to the average exciton number per NP (i.e. $\langle N^2 \rangle$). Also notice that the effective Purcell factor has been multiplied by $\eta(\lambda)$, which is the same as the normalised ensemble NP PL spectrum. This takes into account the detuning between the cavity mode and the homogenously broadened NP spectrum (see section 3.6.2) and forms one of the variables in the rate equations, as illustrated in figure 6.6a. The other variable is the absorption cross-section, $\sigma_{abs}(\lambda)$, which is set by initially taking value at 400 nm from literature and the scaling according to the absorbance curve to calculate the values at the desired spectral position. However, since

both the PL and absorbance get smaller as a function of wavelength these values can be distorted by noise.

For this reason in order to accurately extract the PL it is initially fitted with a pseudo-Voigt function, which is a linear combination of a Lorentzian and a Gaussian function. The Lorentzian part comes from the lifetime effects (Fourier transform of an exponential decay) and the Gaussian part comes from some sort of a broadening mechanism. Since in NPs there is absence of inhomogeneous broadening, it will be most likely due to electron-phonon coupling (homogenous broadening):

$$\eta(\lambda) = y_0 + A\left(\rho\frac{2}{\pi}\frac{w_L}{4(\lambda-\lambda_c)^2 + {w_L}^2} + (1-\rho)\frac{\sqrt{4ln2}}{\sqrt{\pi}w_G}e^{-\frac{4ln2(\lambda-\lambda_c)^2}{{w_G}^2}}\right) \tag{6.5}$$

where y_0 is the y-offset A is the area, λ_c is the centre wavelength, w_L and w_G are the Lorentzian and the Gaussian FWHM, respectively and ρ and $(1-\rho)$ are the relative contributions of the Lorentzian and the Gaussian curves, respectively. Similarly the first absorbance peak is fitted with a Gaussian function of the form:

$$\eta(\lambda) = y_0 + \frac{A}{\gamma_G\sqrt{2\pi}}e^{-\frac{(\lambda-\lambda_c)^2}{2{\gamma_G}^2}} \tag{6.6}$$

where $\gamma_G = \text{FWHM}/2\sqrt{(2ln2)}$ and A is the area. By extracting the parameters the PL and the absorbance can be accurately reproduced to match the experimental values as seen in figures 6.6b and 6.6c.

Table 6.1 lists the values all of the parameters used in equations 6.3 and 6.4. The QY was measured using an integrating sphere (by our collaborators) and the transmission was calculated using the transfer matrix model (at 450 nm for 20 pairs). The absorption cross-section was set to $\sim 1.5 \times 10^{-17}$ m^2 at 450 nm, which is consistent with CdSe/CdS NPs with similar core and shell dimension[16]. The effective Purcell factor was calculated by first measuring the effective Q-factor (using equation 3.49) and then using 3.50. For this the refractive index was calculated using equation 5.25. The confinement factor is calculated by taking the ratio of the physical mode volume and the total mode volume i.e $\Gamma = V_c V^{-1}$, for which V is calculate using the total length L (equation 3.22).

The radiative lifetime was measured using the method detailed in section 4.2.1. The TRPL spectrum is shown in figure 6.7 and is well described by fitting a tri-exponential function of the form given by equation 5.24:

The fitting reveals the values of the three lifetime components which are $\tau_1 = 3$ ns, $\tau_2 = 18$ ns and $\tau_3 = 114$ ns with amplitudes $A_1 = 7386$, $A_2 = 2258$ and $A_3 = 265$, respectively.

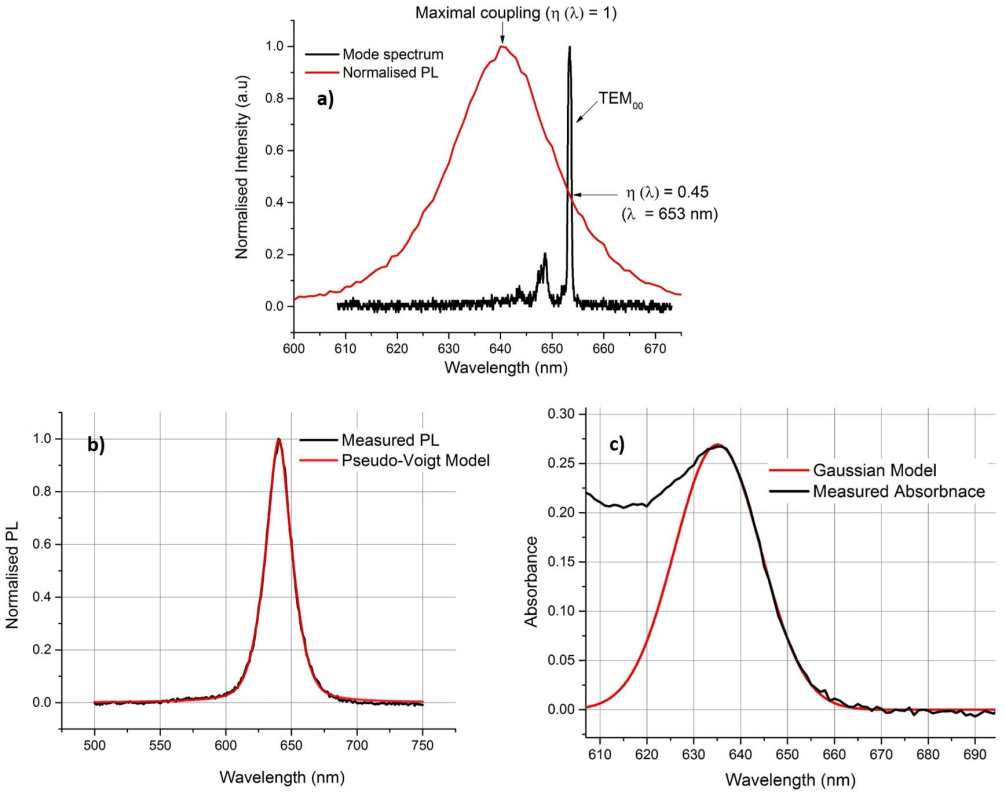

FIGURE 6.6: Extracting the variables. a) Variation of the function $\eta(\lambda)$ as a function of wavelength. b) A plot of the ensemble PL and the pseudo-Voigt model (both normalised). c) A plot to the ensemble absorbance curve and the Gaussian model (both normalised to measure absorbance at 450 nm).

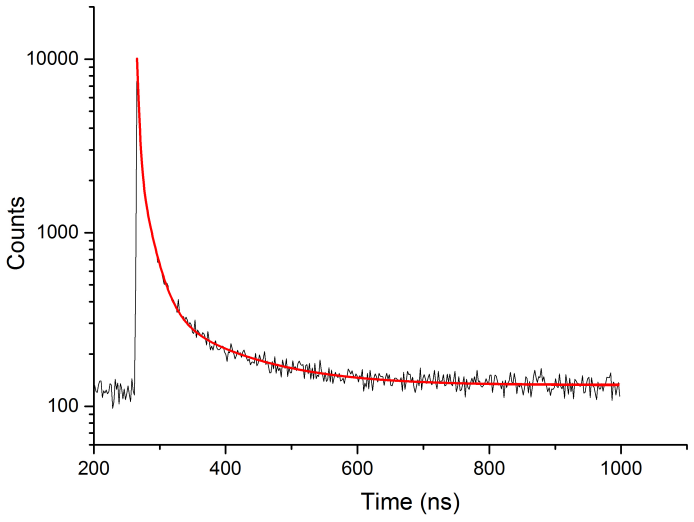

FIGURE 6.7: NP radiative lifetime. The ensemble TRPL spectrum of the NPs fitted to a tri-exponential (log-linear scale).

These components are a result of different emitting states in the NPs[167, 168], however, it is then sensible to use the shortest of the lifetime of 3 ns in our equations. This is because stimulated emission is initially triggered by photons emitted by spontaneous emission. These spontaneously emitted photons will predominantly be from those NPs with the shortest lifetime (i.e. 3 ns). Since the process of stimulated emission occurs very quickly, it is expected that those NPs with emission lifetimes longer than 3 ns will subsequently undergo stimulated emission, instead of emitting photons by spontaneous emission.

The cavity decay time can be calculated by measuring the cavity Q-factor (Q_{cav}) and using the equation[120]:

$$\tau_{cav} = \frac{Q_{cav}\lambda}{2\pi c} \tag{6.7}$$

Q_{cav} will be governed by the self-absorption and scattering of the lasing photons. However, as was seen in section 5.2.2 the Q_{cav} in our system is dominated by the self-absorption, of the lasing photons, but which is already included in equations 6.3 and 6.4. Hence, τ_{cav} in our equations then should only depend on the scattering of the photons, which is difficult to experimentally measure. Furthermore, the concentration of the NPs inside the cavity could not be experimentally measured (the method proposed in section 4.6 was only realised after this experiment). Therefore, the cavity decay time and concentration are the two free parameters in our theory. We initially start with setting the cavity decay time value equal to the intrinsic (empty cavity) value. This can done by measuring the Q-factor on the empty cavity which was $\sim$ 180000 (measurements performed by Aurelien Trichet within the group) for the cavity length of 5.8 μm and so we calculate the intrinsic $\tau_{cav} \sim 61$ ps (λ taken to be 640 nm).

These parameters and others (as described in section 3.7) are summarised in table 6.1. Furthermore, by varying the values of $\eta(\lambda)$ and $\sigma_{abs}(\lambda)$ in equations 6.3 and 6.4 the threshold can be extracted as a function of spectral position. It was found that whilst the theoretical threshold values at longer wavelengths (values beyond the wavelength of 664.9 nm) were sensitive to both the cavity decay time (for example, see figure 6.8c) and the concentration of the NPs, the values below 664.9 nm were only dependent on the concentration, although not significantly. This is because in equation 6.4 the spontaneous, stimulated and re-absorption terms at shorter wavelengths will dominate over the cavity decay term (due to the larger $\eta(\lambda)$ and $\sigma_{abs}(\lambda)$ values at these wavelengths). Thus, the here idea was to change the concentration of the NPs until a good match is found with the measured threshold value at the shortest wavelength (636.7 nm), where

the cavity decay time has little influence. Once this is achieved the cavity decay time can then be adjusted (from the intrinsic value) to get a good match to the overall dataset.

By varying the concentration over a range 0.2-20 $\times$ 10^{21} m^{-3} it was found that the theoretical threshold attained a minimum value of $\sim$ 52 pJ at (636.7 nm) at around 2 $\times$ 10^{21} m^{-3}, as shown in figure 6.8a (note the refractive index does not vary considerably over this range). The reason for this could be as follows. Below the concentration of 2 $\times$ 10^{21} m^{-3} the cavity decay term in equation 6.4 will start dominate over all the other terms (in particular the spontaneous and stimulated emission terms), due to the lower N_{tot} value, which therefore increases the threshold. At higher concentrations the pumping term in equation 6.3 is be lower (more NPs in the mode volume means $\langle N \rangle$ will be lower for the same number of photons entering the system). Since the stimulated and spontaneous emission both contain $\langle N \rangle$, these terms will decrease in comparison to the re-absorption term (which in independent of $\langle N \rangle$) and causing the threshold to rise again. A plot of threshold vs concentration for the three different concentrations, and at three different wavelengths is also shown in figure 6.8b (log-log scale). These wavelength are at 636.7 nm and 683.9 nm, which are the lowest and the highest wavelengths, respectively, for which the threshold was measured and at 664.9 nm, where the lasing minimum was measured. It can be seen clearly that whilst at 636.7 nm a minimum in the lasing threshold (52 pJ) exists at the concentration of 2 $\times$ 10^{21} m^{-3} for the reason explained above, the thresholds at 664.9 nm and 683.9 nm show a monotonic decrease with concentration. The reason for this is that an increase the in concentration also increases $\langle N \rangle$ in equation 6.4, allowing the spontaneous and stimulated emission terms to dominate over the cavity decay term (here the absorption cross-section is lower than below 665 nm).

However, as can be seen the theoretical threshold values are well above the measured value of $\sim$ 31.2 pJ (636.7 nm) for all concentrations. For this reason, the spot-size was reduced from a measured value of 3.5 μm to 2.35 μm until the theoretical value matched the experimental value, for a fixed concentration of 2 $\times$ 10^{21} m^{-3} (where the minimum threshold exists). This can be justified by the fact that measured spot size will be scattering limited, and thus the real spot size will lower that the measured value. Using this reduced spot size, figure 6.8c compares the full the set of experimental and the theoretical values.

Scattering, however, is also expected to decrease the value of τ_{cav} from the intrinsic value of 61 ps. To find the lower limit of this the concentration was initially increased to the point where the theoretical threshold value at shortest wavelength (636.7 nm), matched the highest possible measured value (within error), as can be seen in figure 6.8d (red circles). It can be seen that whilst the thresholds at lower wavelengths increase (for

the reasons mentioned previously), the thresholds at longer wavelengths decrease. The reason for this could be because at longer wavelengths the cavity decay term begins to dominate and so the increase in the concentration favours the spontaneous and stimulated emission terms and, thus, decreases the threshold. However, in this case a better fit (within error) can be made by decreasing the value of τ_{cav} from 61 ps (intrinsic) to 26 ps (blue circles), providing a lower limit for this value. The mismatch between the experimental and theoretical values in some data points (e.g. at 674 nm) is most likely attributed to some degree of misalignment between the cavity and the excitation laser.

QY, ς	21%
Transmission, T	0.94
Absorption cross-section, σ_{450nm}	1.5×10^{-17} m^2
Radiative lifetime, τ_{rad}	3 ns
Purcell factor, $F_p{}^{eff}$	5.7×10^{-3}
Confinement factor, Γ	0.7
Refractive index, n	1.4
Temporal FWHM, L_t	68 ps
Mode volume, V_c	6.2×10^{-18} m^3
Spot size (FWHM), L_{spa}	2.35 μm

TABLE 6.1: Summary of the parameters used in the NP rate equation model.

By using the value of the spot size of 2.35 μm, we calculate a minimum lasing threshold intensity of $\sim$ 204 μJ/cm^2 at 664.9 nm (threshold of 8.84 pJ per pulse). This is comparable to the lasing thresholds observed in films of NPs with similar core and shell thicknesses[169]. The average initial exciton number at threshold, $\langle N_{th} \rangle$, for the NPs can be calculated using the following equation[135]:

$$\langle N_{th} \rangle = \frac{\left(\frac{I_{th}}{\hbar\omega}\right)\sigma_{450nm}}{1 + \frac{I_{th}}{I_{sat}}} \tag{6.8}$$

where I_{th} and I_{sat} are the threshold and saturation intensities, respectively and $\hbar\omega$ is the energy of the excitation photons (450 nm). Taking I_{sat} = 90 μJ/cm^2 [135] then $\langle N_{th} \rangle$ $\sim$ 21 at I_{th} = $\sim$ 204 μJ/cm^2. This value perhaps should not be too surprising since many excitons of the same emission energy can occupy a single NP and so population inversion would require many excitons to be present inside a NP. On the other hand, the threshold intensity (and thus $\langle N_{th} \rangle$) can also be strongly influenced by the QY and the concentration/packing density of the NPs. The QY was measured to be only 21% and can be as a result of two different factors. Whilst the Auger rate is expected to be very low, the thin 2 ML shell may simply does not provide adequate passivation for the carrier so trapping at the surface states may be very high. The other could be due to the efficient collinear stacking (clustering) typically observed for the NPs in solution

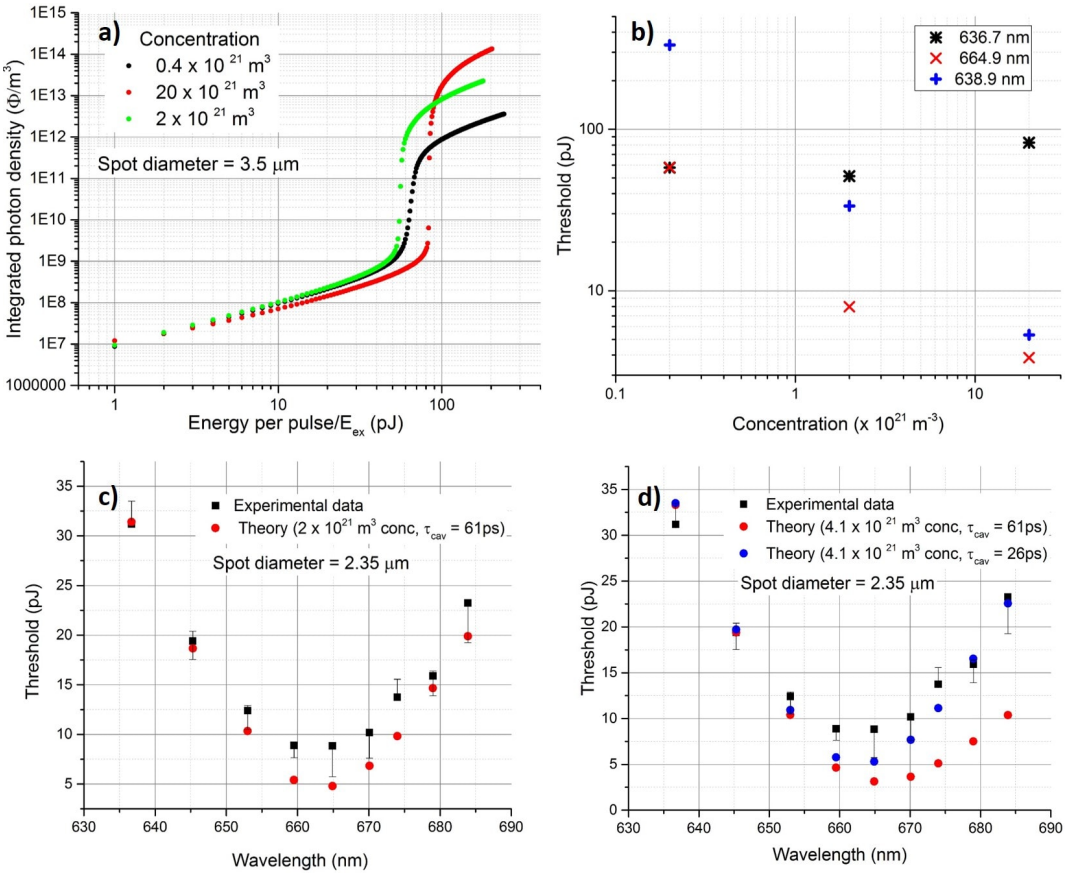

FIGURE 6.8: Theoretical fits to experimental data for NPs. a) Power dependence plots (log-log scale) for various NP concentrations at 636.7 nm with a spot diameter of 3.5 μm. b) A plot of threshold vs concentration for three different concentrations (0.2, 2 and 20 $\times$ 10^{21} m^{-3}) and at three different wavelengths (636.7 nm, 664.9 nm and 683.9 nm) on a log-log scale. The spot size of 3.5 μm was used. c) A plot of experimentally measured threshold values and theoretical values for a spot diameter of 2.35 μm and a concentration of 2 $\times$ 10^{21} m^{-3}. d) A plot of experimentally measured threshold values and theoretical values with the same spot size as in b) but with a concentration of 4.1 $\times$ 10^{21} m^{-3} and with two different cavity decay times.

induced via strong long range van der Waals forces between the NP surfaces[170–172]. Formation of such stacks have been shown to significantly decrease the QY through Förster resonance energy transfer (FRET)[171], in which the exciton energy hops non-radiatively from one NP to another within the stack. Such migration allows trapping of the excitons by non-emissive NPs within the stack which then undergo non-radiative recombination, decreasing the QY.

Another consequence of stacking could be to reduce packing density of the NPs within the cavity. The rate equations suggests a maximum packing density of only $\sim 0.5\%$ (for a concentration of 4.1 $\times$ 10^{21} m^{-3}). Whilst the initial NP concentration may be high, the stacking of the NPs can collect them in certain region of the solution. When a cavity is formed around the solution and the cavity length decreased it could push away large clusters of the NPs from the cavity mode volume, thus decreasing their concentration.

6.4 Conclusion

The results of gain spectroscopy using solution based CdSe/CdS NPs was presented. The lasing threshold and the differential gain were measured as a function of the spectral position for a range spanning $\sim$ 42 nm. The lasing threshold was found to have a minimum red-shifted by $\sim$ 25 nm with respect to the ensemble PL peak position. This spectral position also coincided with a maximum in the differential gain indicating a spectral position where the lasing process is the most efficient. Tunable laser emission from the fundamental cavity mode was demonstrated over a range of $\sim$ 42 nm with single mode laser emission for a range of over 37 nm. In addition, it was found that laser emission from the NPs can be sustained at a constant intensity for almost 6 minutes before deteriorating, which was attributed to charging of the NP cores. A rate equation model was proposed to describe the results of the gain spectroscopy. From this modelling, like in the case of NCs, it was found that the governing process that determines the shape of the gain profile is the competition between the stimulated emission and the self-absorption of the lasing photons.

The minimum lasing intensity was measured to be $\sim$ 204 μJ/cm^2, giving an average exciton number of $\sim$ 21 per NP. Although this is comparable to the lasing thresholds observed in films of NPs with similar core and shell thicknesses[169], it can be significantly influenced by the QY and the packing density (concentration) of the NPs. The QY was measured to be only 21% and this value low QY could be as a result of the thin CdS shell (2 ML) such that carrier trapping efficiency increases significantly. Additionally, NPs have been observed to stack in columns which can significantly reduce their QY due to FRET[170–172]. The rate equation model also suggests a packing density on NPs in our cavities of $\sim$ 0.5%. This could be as a result of the clusters of NPs being pushed away from the cavity when the cavity length is decreased.

Thus, the lasing NP lasing threshold may be significantly improved by increasing the QY and the packing density of the NPs. One way the QY can be improved is to increase the shell thickness to provide better passivation. Another is to prevent the stacking of the NPs in solution, which as well as significantly improving the QY will also aid in maintaining a high NPs concertation within the cavity. One way this can be done is to coat the NPs with a carboxylic acid-terminated polystyrene[172] which prevents the clustering of the NPs by inducing longer-range repulsion forces.

Chapter 7

Conclusion and Future Work

7.1 Conclusion

This thesis describes the result of gain spectroscopy of CQDs using an open access cavity. By using such a cavity the lasing threshold as a function of the cavity length was extracted over a spectral range dictated by the CQD ensemble PL spectrum. The in-situ tuning method does not modify the CQDs and so the observed lasing behaviour was attributed unambiguously to the change in the feedback wavelength alone. Two different type of CQDs were investigated: NCs and NPs. In both cases, lasing was obtained from a highly concentrated solution of CQDs immersed in a non-volatile solvent (octadecane). This produced a solution with reduced scattering, but more importantly, produced the required packing density to overcome the multiexcitonic Auger process, especially in the case of NCs.

Chapter 5 presented the results of gain spectroscopy of CdSe/CdS NCs. The minimum lasing threshold was found to be red-shifted with respect to the ensemble PL peak and also the first absorbance peak. At the position of this minimum the average exciton number was measured to around ~ 1.4, which is consistent with the biexction lasing mechanism expected in CdSe/CdSe NCs (quasi-type I system). The minimum lasing threshold was measured to be ~ 23 ($\pm$ 5) μJ cm^{-2}, which was almost two order of magnitude smaller than those reported for other type-I systems[159, 163] and even lower than those reported for lasing in single exciton regime[113]. The low lasing threshold measured here is, in fact, comparable to ASE threshold of 30 μJ cm^{-2} as demosntarted by Guzelturk *et al*[95] (with a comparable pump pulse width of 120 fs) using CdSe/CdS NCs with a smooth confining barrier to reduce the Auger recombination rate, and also comparable to lasing threshold of 13.5 μJ/cm^2 from CdSe/ZnS NCs reported by McLellan *et al*[101] from a DFB laser. The lasing in the latter paper was, however, achieved

with a 5 ns pump pulse width, and this was made possible by the use of alloyed core-shell CdSe/ZnS NCs to mitigate the effects of multiexcitonic Auger recombination and also by integrating a layer on top of the NC film made from polyvinyl alcohol (PVA) for better mode confinement. The low threshold in our experiment was attributed to the high packing density of the CQDs (21 %) and also the large absorption cross-section due to the thick 7 ML CdS shell. Furthermore, single mode lasing (from the fundamental cavity mode) was demonstrated for a range of $\sim$ 25 nm. An important realisation made was that the Q-factor of the modes were limited by the self-absorption of the lasing photons not by the mirror reflectivity. In this regard, using cavities with higher reflectivities will not improve on the measured lasing thresholds, and any influence on the lasing behaviour as a result of the change in the cavity reflectivity across the stop-band was, thus, also ruled out. Finally, an analytical theory was presented to describe the results of gain spectroscopy, and from this was concluded that governing process that determined the measured lasing profile was the interplay between the stimulated emission and self-absorption of the lasing photons.

Chapter 6 presented the results of gain spectroscopy using CdSe/CdS core-shell NPs. Compared to NCs the NPs are expected to have reduced Auger rates as well as large gain and absorption cross-sections, thus should help in reducing the lasing thresholds. Similar to the NCs, a minimum lasing threshold was found to be red-shifted respect to the ensemble PL peak and the first absorbance peak. Moreover, tunable single mode laser emission was demonstrated for a range of over 37 nm. It was also found that the lasing mode maintained a stable intensity for $\sim$ 354 seconds ($\sim$ 6 mins or almost 1.8×10^9 consecutive laser pulses), before photo-charging began to quench the emission. A rate equation model was used to describe the results of gain spectroscopy, and like in the case of NCs, it was found that lasing behaviour was primarily governed by the competition between stimulated emission and self-absorption. The minimum lasing threshold was measured to be $\sim$ 204 μJ/cm^2, with an average exciton number $\sim$ 21 per NP. Although the threshold value is comparable to those reported for similar NPs[169] it is almost an order or magnitude larger than for NCs. This was unexpected, as the lasing process should be more efficient in NPs for the reasons mentioned above. One reason for this could be that the QY was measured to be only 21% (as opposed to $\sim$ 60 % for NCs), mostly likely due the thin CdS shell (2 ML), thus increasing the carrier trapping rate. In addition, due to the tendency of the NPs to cluster FRET can occur, which will also reduce the QY further. Moreover, the maximum packing density extracted from rate the equation analysis was only 0.5%, which is around 40 times lower than the NCs (21%). This could be as a result of the clusters of NPs being pushed away from the cavity when the cavity length is decreased, and thus reducing the NPs concentration inside the cavity compared to the original solution.

7.2 Future work

The work in this thesis has shown that the lasing thresholds are primarily governed by the competition between stimulated emission and self-absorption of the lasing photons. However, the theory in the case of both NCs and NPs suggests that the lasing thresholds are strongly influenced by the concentration. The next step therefore would be to perform a systematic study of the dependence of the lasing thresholds as a function of the concentration. A higher concentrations, however, an additional factor that must be considered is the inter-dot energy transfer (FRET) between CQDs of different sizes can occur (or in the case of NPs between NPs of the same size within a cluster), which is also expected to have a strong influence on the lasing behaviour. Furthermore, achieving high Purcell factors can benefit the lasing process in two different ways. Firstly, it will increase the rate of spontaneous and stimulated emission in order to overcome the multiexciton Auger process. Secondly, a higher Purcell factor can also increase the β factor, meaning that a greater fraction of the emitted photons enter the desired cavity mode, lowering the lasing threshold. However, due to large homogenous linewidths (at room temperature) the Purcell factors for CQDs were found to be very small. One solution to this would be to lower the temperature of the CQDs to decrease their linewidth, however, this would pose a major hindrance to the commercial realisation of lasing devices using CQDs as gain media. Thus, another solution would be to use a small mode volume cavity i.e. with a lower RoC than already used in the experiments (25 μm) to increase the Purcell factor. In addition, a smaller RoC will also have a larger FSR, which means less modes are accommodated within the stop-band of the cavity and this would help in producing lasing in the single mode regime (i.e with less transverse modes than a compared to cavity of the same length but with a bigger RoC).

The work done here can be expanded to study the effects of the exciton-exciton interaction energies on the lasing behaviour of the CQDs. For example, by physically modifying the size of the core and shell CdSe/CdS NCs and thus the distribution of the carrier wavefunctions, Gollner et al[162] showed that the exciton-exciton interaction can be altered significantly. By conducting ASE experiments on such structures the peak of the ASE can be shifted above, at or below the energy of the single exciton emission depending on the interaction energy, as shown in 7.1. Such behaviour can be correlated with the gain spectroscopy results to provide further information role of Coulomb interactions in the lasing process.

Furthermore, core-shell CQDs soft confining potentials have been known to modifying the electronic DOS and extend the Auger lifetimes[94], and will reduce the lasing thresholds compared to CQDs with an abrupt heterointerface likes the ones used in this thesis. Another strategy would be to use type-II core-shell structures, such as CdTe/CdSe or

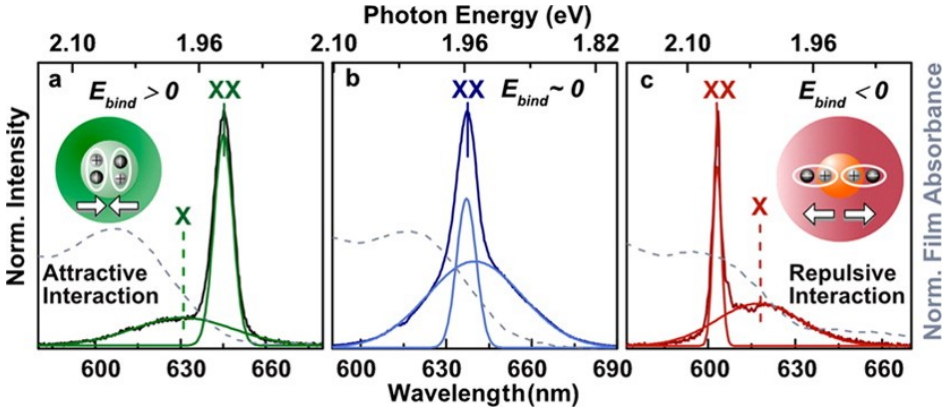

FIGURE 7.1: ASE from biexciton (xx) in CdSe/CdS films NCs with a positive (a) and a negative (c) biexciton binding energy (E_{bind}). In b) E_{bind} is almost negligible. The ASE spectra are overlaid on top of the PL emission produced by single excitons (x) and also the normalised absorbance curves (grey dashed lined). Reproduced from ref [162] with permission.

ZnTe/ZnSe, where the exciton-exciton interactions can exceed the ensemble emission linewidth enabling lasing in the lasing exciton regime to occur[38]. In such structures, however, a decrease in the oscillator strength is expected due to the reduction the electron and hole wavefunction overlap, and greater packing density may be required to compensate for this, and where FRET may become large enough significant role in the lasing process.

Bibliography

[1] Chia-Hao M Chuang, Patrick R Brown, Vladimir Bulović, and Moungi G Bawendi. Improved performance and stability in quantum dot solar cells through band alignment engineering. *Nature Materials*, 13(8):796, 2014.

[2] Gerasimos Konstantatos, Ian Howard, Armin Fischer, Sjoerd Hoogland, Jason Clifford, Ethan Klem, Larissa Levina, and Edward H Sargent. Ultrasensitive solution-cast quantum dot photodetectors. *Nature*, 442(7099):180–183, 2006.

[3] Lei Qian, Ying Zheng, Jiangeng Xue, and Paul H Holloway. Stable and efficient quantum-dot light-emitting diodes based on solution-processed multilayer structures. *Nature Photonics*, 5(9):543–548, 2011.

[4] C B Murray, David J Norris, and Moungi G Bawendi. Synthesis and characterization of nearly monodisperse CdE (E= sulfur, selenium, tellurium) semiconductor nanocrystallites. *Journal of the American Chemical Society*, 115(19):8706–8715, 1993.

[5] Hojun Chang, Kyungtaek Min, Myungjae Lee, Minsu Kang, Yeonsang Park, Kyung-Sang Cho, Young-Geun Roh, Sung Woo Hwang, and Heonsu Jeon. Colloidal quantum dot lasers built on a passive two-dimensional photonic crystal backbone. *Nanoscale*, 8(12):6571–6576, 2016.

[6] Seth Coe, Wing-Keung Woo, Moungi Bawendi, and Vladimir Bulović. Electroluminescence from single monolayers of nanocrystals in molecular organic devices. *Nature*, 420(6917):800–803, 2002.

[7] Emine Tekin, Patrick J Smith, Stephanie Hoeppener, Antje MJ van den Berg, Andrei S Susha, Andrey L Rogach, Jochen Feldmann, and Ulrich S Schubert. Inkjet printing of luminescent CdTe nanocrystal–polymer composites. *Advanced Functional Materials*, 17(1):23–28, 2007.

[8] LeeAnn Kim, Polina O Anikeeva, Seth A Coe-Sullivan, Jonathan S Steckel, Moungi G Bawendi, and Vladimir Bulovic. Contact printing of quantum dot light-emitting devices. *Nano Letters*, 8(12):4513–4517, 2008.

[9] Victor I Klimov, AA Mikhailovsky, DW McBranch, CA Leatherdale, and Moungi G Bawendi. Quantization of multiparticle Auger rates in semiconductor quantum dots. *Science*, 287(5455):1011–1013, 2000.

[10] Z Adam Peng and Xiaogang Peng. Mechanisms of the shape evolution of CdSe nanocrystals. *Journal of the American Chemical Society*, 123(7):1389–1395, 2001.

[11] Liberato Manna, Delia J Milliron, Andreas Meisel, Erik C Scher, and A Paul Alivisatos. Controlled growth of tetrapod-branched inorganic nanocrystals. *Nature Materials*, 2(6):382–385, 2003.

[12] Sandrine Ithurria and Benoit Dubertret. Quasi 2D colloidal CdSe platelets with thicknesses controlled at the atomic level. *Journal of the American Chemical Society*, 130(49):16504–16505, 2008.

[13] X Michalet, FF Pinaud, LA Bentolila, JM Tsay, SJJL Doose, JJ Li, G Sundaresan, AM Wu, SS Gambhir, and S Weiss. Quantum dots for live cells, in vivo imaging, and diagnostics. *science*, 307(5709):538–544, 2005.

[14] S Brovelli, RD Schaller, SA Crooker, F García-Santamaría, Y Chen, R Viswanatha, JA Hollingsworth, H Htoon, and VI Klimov. Nano-engineered electron–hole exchange interaction controls exciton dynamics in core–shell semiconductor nanocrystals. *Nature Communications*, 2:280, 2011.

[15] Jin Joo, Jae Sung Son, Soon Gu Kwon, Jung Ho Yu, and Taeghwan Hyeon. Low-temperature solution-phase synthesis of quantum well structured CdSe nanoribbons. *Journal of the American Chemical Society*, 128(17):5632–5633, 2006.

[16] Lucas T Kunneman, Mickael D Tessier, Hadrien Heuclin, Benoit Dubertret, Yaroslav V Aulin, Ferdinand C Grozema, Juleon M Schins, and Laurens DA Siebbeles. Bimolecular Auger recombination of electron-hole pairs in two-dimensional CdSe and CdSe/CdZnS core/shell nanoplatelets. *The Journal of Physical Chemistry Letters*, 4(21):3574–3578, 2013.

[17] Ali Naeem, Francesco Masia, Sotirios Christodoulou, Iwan Moreels, Paola Borri, and Wolfgang Langbein. Evidence of giant oscillator strength in the exciton dephasing of CdSe nanoplatelets measured by resonant four-wave mixing. *arXiv preprint arXiv:1403.7798*, 2014.

[18] Alexander W Achtstein, Andrei Schliwa, Anatol Prudnikau, Marya Hardzei, Mikhail V Artemyev, Christian Thomsen, and Ulrike Woggon. Electronic structure and exciton-phonon interaction in two-dimensional colloidal CdSe nanosheets. *Nano Letters*, 12(6):3151–3157, 2012.

[19] Aydan Yeltik, Savas Delikanli, Murat Olutas, Yusuf Kelestemur, Burak Guzelturk, and Hilmi Volkan Demir. Experimental Determination of the Absorption Cross-Section and Molar Extinction Coefficient of Colloidal CdSe Nanoplatelets. *The Journal of Physical Chemistry C*, 119(47):26768–26775, 2015.

[20] AL Rogach. Semiconductor nanocrystal quantum dots: synthesis, assembly, spectroscopy and applications, 2008.

[21] Andrew M Smith, Aaron M Mohs, and Shuming Nie. Tuning the optical and electronic properties of colloidal nanocrystals by lattice strain. *Nature Nanotechnology*, 4(1):56–63, 2009.

[22] Margaret A. Hines and Philippe Guyot-Sionnest. Synthesis and Characterization of Strongly Luminescing ZnS-Capped CdSe Nanocrystals. *The Journal of Physical Chemistry*, 100(2):468–471, 1996. doi: 10.1021/jp9530562.

[23] Xiaogang Peng, Michael C. Schlamp, Andreas V. Kadavanic, and A. P. Alivisatos. Epitaxial Growth of Highly Luminescent CdSe/CdS Core/Shell Nanocrystals with Photostability and Electronic Accessibility. *Journal of the American Chemical Society*, 119(30):7019–7029, 1997. doi: 10.1021/ja970754m.

[24] B. O. Dabbousi, J. Rodriguez-Viejo, F. V. Mikulec, J. R. Heine, K. F. Jensen H. Mattoussi, R. Ober, and M. G. Bawendi. (CdSe)ZnS CoreShell Quantum Dots: Synthesis and Characterization of a Size Series of Highly Luminescent Nanocrystallites. *The Journal of Physical Chemistry B*, 101(46):9463–9475, 1997. doi: 10.1021/jp971091y.

[25] Peter Reiss, Joël Bleuse, and Adam Pron. Highly luminescent CdSe/ZnSe core/shell nanocrystals of low size dispersion. *Nano Letters*, 2(7):781–784, 2002.

[26] Jonathan S Steckel, John P Zimmer, Seth Coe-Sullivan, Nathan E Stott, Vladimir Bulović, and Moungi G Bawendi. Blue luminescence from (CdS) ZnS core–shell nanocrystals. *Angewandte Chemie International Edition*, 43(16):2154–2158, 2004.

[27] Hsueh-Shih Chen, Bertrand Lo, Jen-Yu Hwang, Gwo-Yang Chang, Chien-Ming Chen, Shih-Jung Tasi, and Shian-Jy Jassy Wang. Colloidal ZnSe, ZnSe/ZnS, and ZnSe/ZnSeS quantum dots synthesized from ZnO. *The Journal of Physical Chemistry B*, 108(44):17119–17123, 2004.

[28] Huaibin Shen, Hongzhe Wang, Xiaomin Li, Jin Zhong Niu, Hua Wang, Xia Chen, and Lin Song Li. Phosphine-free synthesis of high quality ZnSe, ZnSe/ZnS, and Cu-, Mn-doped ZnSe nanocrystals. *Dalton Transactions*, (47):10534–10540, 2009.

[29] Dingan Chen, Fei Zhao, Hang Qi, Michael Rutherford, and Xiaogang Peng. Bright and stable purple/blue emitting CdS/ZnS core/shell nanocrystals grown by thermal cycling using a single-source precursor. *Chemistry of Materials*, 22(4):1437–1444, 2010.

[30] Marco Cirillo, Tangi Aubert, Raquel Gomes, Rik Van Deun, Philippe Emplit, Amelie Biermann, Holger Lange, Christian Thomsen, Edouard Brainis, and Zeger Hens. Flash Synthesis of CdSe/CdS CoreShell Quantum Dots. *Chemistry of Materials*, 26(2):1154–1160, 2014. doi: 10.1021/cm403518a.

[31] Renguo Xie, Ute Kolb, Jixue Li, Thomas Basché, and Alf Mews. Synthesis and characterization of highly luminescent CdSe-core CdS/Zn0. 5Cd0. 5S/ZnS multishell nanocrystals. *Journal of the American Chemical Society*, 127(20):7480–7488, 2005.

[32] Sergei A Ivanov, Jagjit Nanda, Andrei Piryatinski, Marc Achermann, Laurent P Balet, Ilia V Bezel, Polina O Anikeeva, Sergei Tretiak, and Victor I Klimov. Light amplification using inverted core/shell nanocrystals: towards lasing in the single-exciton regime. *The Journal of Physical Chemistry B*, 108(30):10625–10630, 2004.

[33] LP Balet, SA Ivanov, A Piryatinski, M Achermann, and VI Klimov. Inverted core/shell nanocrystals continuously tunable between type-I and type-II localization regimes. *Nano Letters*, 4(8):1485–1488, 2004.

[34] Xinhua Zhong, Renguo Xie, Ying Zhang, Thomas Basche, and Wolfgang Knoll. High-quality violet-to red-emitting ZnSe/CdSe core/shell nanocrystals. *Chemistry of Materials*, 17(16):4038–4042, 2005.

[35] Zhenxiao Pan, Hua Zhang, Kan Cheng, Yumei Hou, Jianli Hua, and Xinhua Zhong. Highly efficient inverted type-I CdS/CdSe core/shell structure QD-sensitized solar cells. *ACS Nano*, 6(5):3982–3991, 2012.

[36] Sungjee Kim, Brent Fisher, Hans-Jrgen Eisler, , and Moungi Bawendi*. Type-II Quantum Dots: CdTe/CdSe(Core/Shell) and CdSe/ZnTe(Core/Shell) Heterostructures. *Journal of the American Chemical Society*, 125(38):11466–11467, 2003. doi: 10.1021/ja0361749. PMID: 13129327.

[37] Renguo Xie, Xinhua Zhong, and Thomas Basché. Synthesis, characterization, and spectroscopy of type-II core/shell semiconductor nanocrystals with ZnTe cores. *Advanced Materials*, 17(22):2741–2745, 2005.

[38] Victor I Klimov, Sergei A Ivanov, Jagjit Nanda, Marc Achermann, Ilya Bezel, John A McGuire, and Andrei Piryatinski. Single-exciton optical gain in semiconductor nanocrystals. *Nature*, 447(7143):441–446, 2007.

[39] J Nanda, SA Ivanov, H Htoon, I Bezel, A Piryatinski, S Tretiak, and VI Klimov. Absorption cross sections and Auger recombination lifetimes in inverted core-shell nanocrystals: Implications for lasing performance. *Journal of Applied Physics*, 99 (3):034309, 2006.

[40] Peter Reiss, Myriam Protire, and Liang Li. Core/Shell Semiconductor Nanocrystals. *Small*, 5(2):154–168, 2009. ISSN 1613-6829.

[41] Bashir O Dabbousi, Javier Rodriguez-Viejo, Frederic V Mikulec, Jason R Heine, Hedi Mattoussi, Raymond Ober, Klavs F Jensen, and Moungi G Bawendi. (CdSe) ZnS core- shell quantum dots: synthesis and characterization of a size series of highly luminescent nanocrystallites. *The Journal of Physical Chemistry B*, 101 (46):9463–9475, 1997.

[42] Peter Reiss, Sophie Carayon, Joël Bleuse, and Adam Pron. Low polydispersity core/shell nanocrystals of CdSe/ZnSe and CdSe/ZnSe/ZnS type: preparation and optical studies. *Synthetic Metals*, 139(3):649–652, 2003.

[43] Joël Bleuse, Sophie Carayon, and Peter Reiss. Optical properties of core/multishell CdSe/Zn (S, Se) nanocrystals. *Physica E: Low-dimensional Systems and Nanostructures*, 21(2):331–335, 2004.

[44] Dmitri V Talapin, Ivo Mekis, Stephan Götzinger, Andreas Kornowski, Oliver Benson, and Horst Weller. CdSe/CdS/ZnS and CdSe/ZnSe/ZnS core-shell-shell nanocrystals. *The Journal of Physical Chemistry B*, 108(49):18826–18831, 2004.

[45] Sergei A Ivanov, Andrei Piryatinski, Jagjit Nanda, Sergei Tretiak, Kevin R Zavadil, William O Wallace, Don Werder, and Victor I Klimov. Type-II core/shell CdS/ZnSe nanocrystals: synthesis, electronic structures, and spectroscopic properties. *Journal of the American Chemical Society*, 129(38):11708–11719, 2007.

[46] Dmitri V Talapin, Andrey L Rogach, Andreas Kornowski, Markus Haase, and Horst Weller. Highly luminescent monodisperse CdSe and CdSe/ZnS nanocrystals synthesized in a hexadecylamine- trioctylphosphine oxide- trioctylphospine mixture. *Nano Letters*, 1(4):207–211, 2001.

[47] Jongnam Park, Kwangjin An, Yosun Hwang, Je-Geun Park, Han-Jin Noh, Jae-Young Kim, Jae-Hoon Park, Nong-Moon Hwang, and Taeghwan Hyeon. Ultra-large-scale syntheses of monodisperse nanocrystals. *Nature Materials*, 3(12):891–895, 2004.

[48] Victor K LaMer and Robert H Dinegar. Theory, production and mechanism of formation of monodispersed hydrosols. *Journal of the American Chemical Society*, 72(11):4847–4854, 1950.

[49] Z Adam Peng and Xiaogang Peng. Nearly monodisperse and shape-controlled CdSe nanocrystals via alternative routes: nucleation and growth. *Journal of the American Chemical Society*, 124(13):3343–3353, 2002.

[50] Jongnam Park, Jin Joo, Soon Gu Kwon, Youngjin Jang, and Taeghwan Hyeon. Synthesis of monodisperse spherical nanocrystals. *Angewandte Chemie International Edition*, 46(25):4630–4660, 2007.

[51] Jiwon Bang, Juwon Park, Ji Hwang Lee, Nayoun Won, Jutaek Nam, Jongwoo Lim, Byoung Yong Chang, Hyo Joong Lee, Bonghwan Chon, Junghan Shin, et al. ZnTe/ZnSe (core/shell) type-II quantum dots: their optical and photovoltaic properties. *Chemistry of Materials*, 22(1):233–240, 2009.

[52] J Jack Li, Y Andrew Wang, Wenzhuo Guo, Joel C Keay, Tetsuya D Mishima, Matthew B Johnson, and Xiaogang Peng. Large-scale synthesis of nearly monodisperse CdSe/CdS core/shell nanocrystals using air-stable reagents via successive ion layer adsorption and reaction. *Journal of the American Chemical Society*, 125(41): 12567–12575, 2003.

[53] Yongfen Chen, Javier Vela, Han Htoon, Joanna L Casson, Donald J Werder, David A Bussian, Victor I Klimov, and Jennifer A Hollingsworth. Giant multishell CdSe nanocrystal quantum dots with suppressed blinking. *Journal of the American Chemical Society*, 130(15):5026–5027, 2008.

[54] SS Prabhu, AS Vengurlekar, SK Roy, and Jagdeep Shah. Nonequilibrium dynamics of hot carriers and hot phonons in CdSe and GaAs. *Physical Review B*, 51(20): 14233, 1995.

[55] V Klimov, P Haring Bolivar, and H Kurz. Hot-phonon effects in femtosecond luminescence spectra of electron-hole plasmas in CdS. *Physical Review B*, 52(7): 4728, 1995.

[56] U Bockelmann and G Bastard. Phonon scattering and energy relaxation in two-, one-, and zero-dimensional electron gases. *Physical Review B*, 42(14):8947, 1990.

[57] H Benisty, CM Sotomayor-Torres, and C Weisbuch. Intrinsic mechanism for the poor luminescence properties of quantum-box systems. *Physical Review B*, 44(19): 10945, 1991.

[58] Takeshi Inoshita and Hiroyuki Sakaki. Electron relaxation in a quantum dot: Significance of multiphonon processes. *Physical Review B*, 46(11):7260, 1992.

[59] S Xu, AA Mikhailovsky, JA Hollingsworth, and VI Klimov. Hole intraband relaxation in strongly confined quantum dots: Revisiting the phonon bottleneck problem. *Physical Review B*, 65(4):045319, 2002.

[60] Kai Shum, WB Wang, RR Alfano, and Kim M Jones. Observation of the 1P excitonic states in Cd (S, Se)-glass quantum dots. *Physical Review Letters*, 68 (26):3904, 1992.

[61] V Klimov, S Hunsche, and H Kurz. Biexciton effects in femtosecond nonlinear transmission of semiconductor quantum dots. *Physical Review B*, 50(11):8110, 1994.

[62] U Woggon, H Giessen, F Gindele, O Wind, B Fluegel, and N Peyghambarian. Ultrafast energy relaxation in quantum dots. *Physical Review B*, 54(24):17681, 1996.

[63] Victor I Klimov and Duncan W McBranch. Femtosecond 1 P-to-1 S electron relaxation in strongly confined semiconductor nanocrystals. *Physical Review Letters*, 80(18):4028, 1998.

[64] Philippe Guyot-Sionnest, Moonsub Shim, Chris Matranga, and Margaret Hines. Intraband relaxation in CdSe quantum dots. *Physical Review B*, 60(4):R2181, 1999.

[65] Al L Efros, VA Kharchenko, and M Rosen. Breaking the phonon bottleneck in nanometer quantum dots: Role of auger-like processes. *Solid State Communications*, 93(4):281–284, 1995.

[66] Philippe Guyot-Sionnest, Brian Wehrenberg, and Dong Yu. Intraband relaxation in CdSe nanocrystals and the strong influence of the surface ligands. *The Journal of Chemical Physics*, 123(7):074709–074709, 2005.

[67] Darrell F Schroeter, David J Griffiths, and Peter C Sercel. Defect-assisted relaxation in quantum dots at low temperature. *Physical Review B*, 54(3):1486, 1996.

[68] Marc Achermann, Andrew P Bartko, Jennifer A Hollingsworth, and Victor I Klimov. The effect of Auger heating on intraband carrier relaxation in semiconductor quantum rods. *Nature Physics*, 2(8):557–561, 2006.

[69] Matthew Pelton, Sandrine Ithurria, Richard D Schaller, Dmitriy S Dolzhnikov, and Dmitri V Talapin. Carrier cooling in colloidal quantum wells. *Nano Letters*, 12(12):6158–6163, 2012.

[70] M Nirmal, BO Dabbousi, MG Bawendi, JJ Macklin, JK Trautman, TD Harris, and LE Brus. Fluorescence intermittency in single cadmium selenide nanocrystals. *Nature*, 383(6603):802–804, 1996.

[71] Amy A Cordones and Stephen R Leone. Mechanisms for charge trapping in single semiconductor nanocrystals probed by fluorescence blinking. *Chemical Society Reviews*, 42(8):3209–3221, 2013.

[72] Shu Li, Michael L Steigerwald, and Louis E Brus. Surface states in the photoionization of high-quality CdSe core/shell nanocrystals. *ACS Nano*, 3(5):1267–1273, 2009.

[73] John A McGuire, Milan Sykora, István Robel, Lazaro A Padilha, Jin Joo, Jeffrey M Pietryga, and Victor I Klimov. Spectroscopic signatures of photocharging due to hot-carrier transfer in solutions of semiconductor nanocrystals under low-intensity ultraviolet excitation. *ACS Nano*, 4(10):6087–6097, 2010.

[74] Christophe Galland, Yagnaseni Ghosh, Andrea Steinbrück, Milan Sykora, Jennifer A Hollingsworth, Victor I Klimov, and Han Htoon. Two types of luminescence blinking revealed by spectroelectrochemistry of single quantum dots. *Nature*, 479(7372):203–207, 2011.

[75] VI Klimov, Ch J Schwarz, DW McBranch, CA Leatherdale, and MG Bawendi. Ultrafast dynamics of inter-and intraband transitions in semiconductor nanocrystals: Implications for quantum-dot lasers. *Physical Review B*, 60(4):R2177, 1999.

[76] Victor I Klimov. Optical nonlinearities and ultrafast carrier dynamics in semiconductor nanocrystals. *The Journal of Physical Chemistry B*, 104(26):6112–6123, 2000.

[77] A. V. Malko, A. A. Mikhailovsky, M. A. Petruska, J. A. Hollingsworth, , and V. I. Klimov*. Interplay between Optical Gain and Photoinduced Absorption in CdSe Nanocrystals. *The Journal of Physical Chemistry B*, 108(17):5250–5255, 2004. doi: 10.1021/jp037699q.

[78] Vikram C Sundar, H-J Eisler, and Moungi G Bawendi. Room-Temperature, Tunable Gain Media from Novel II–VI Nanocrystal–Titania Composite Matrices. *Advanced Materials*, 14(10):739–743, 2002.

[79] Melissa A Petruska, Anton V Malko, Paul M Voyles, and Victor I Klimov. High-Performance, Quantum Dot Nanocomposites for Nonlinear Optical and Optical Gain Applications. *Advanced Materials*, 15(7-8):610–613, 2003.

[80] VI Klimov, AA Mikhailovsky, JA Hollingsworth, A Malko, CA Leatherdale, HJ Eisler, and MG Bawendi. Stimulated emission and lasing in nanocrystal quantum dots. *Quantum Confinement: Nanostructured Materials and Devices. Proceedings of the Electrochemical Society*, 19:321, 2001.

[81] F Gindele, R Westphäling, U Woggon, L Spanhel, and V Ptatschek. Optical gain and high quantum efficiency of matrix-free, closely packed CdSe quantum dots. *Applied Physics Letters*, 71(15):2181–2183, 1997.

[82] VI Klimov, AA Mikhailovsky, Su Xu, A Malko, JA Hollingsworth, CA Leatherdale, H-J Eisler, and MG Bawendi. Optical gain and stimulated emission in nanocrystal quantum dots. *Science*, 290(5490):314–317, 2000.

[83] AA Mikhailovsky, AV Malko, JA Hollingsworth, MG Bawendi, and VI Klimov. Multiparticle interactions and stimulated emission in chemically synthesized quantum dots. *Applied Physics Letters*, 80(13):2380–2382, 2002.

[84] Lin-Wang Wang, Marco Califano, Alex Zunger, and Alberto Franceschetti. Pseudopotential theory of Auger processes in CdSe quantum dots. *Physical Review Letters*, 91(5):056404, 2003.

[85] Dipankar Chattarji. *The theory of Auger transitions*. Elsevier, 2012.

[86] DI Chepic, Al L Efros, AI Ekimov, MG Ivanov, VA Kharchenko, IA Kudriavtsev, and TV Yazeva. Auger ionization of semiconductor quantum drops in a glass matrix. *Journal of Luminescence*, 47(3):113–127, 1990.

[87] VA Kharchenko and M Rosen. Auger relaxation processes in semiconductor nanocrystals and quantum wells. *Journal of Luminescence*, 70(1):158–169, 1996.

[88] Praket P Jha and Philippe Guyot-Sionnest. Trion decay in colloidal quantum dots. *ACS Nano*, 3(4):1011–1015, 2009.

[89] Marco Marceddu, Michele Saba, Francesco Quochi, Adriano Lai, Jing Huang, Dmitri V Talapin, Andrea Mura, and Giovanni Bongiovanni. Charged excitons, Auger recombination and optical gain in CdSe/CdS nanocrystals. *Nanotechnology*, 23(1):015201, 2011.

[90] Richard D Schaller and Victor I Klimov. High efficiency carrier multiplication in PbSe nanocrystals: implications for solar energy conversion. *Physical Review Letters*, 92(18):186601, 2004.

[91] Han Htoon, Anton V Malko, D Bussian, Javier Vela, Yongfen Chen, Jennifer A Hollingsworth, and Victor I Klimov. Highly emissive multiexcitons in steady-state photoluminescence of individual giant CdSe/CdS core/shell nanocrystals. *Nano Letters*, 10(7):2401–2407, 2010.

[92] Andrei Piryatinski, Sergei A Ivanov, Sergei Tretiak, and Victor I Klimov. Effect of quantum and dielectric confinement on the exciton-exciton interaction energy in type ii core/shell semiconductor nanocrystals. *Nano Letters*, 7(1):108–115, 2007.

[93] Xiaoyong Wang, Xiaofan Ren, Keith Kahen, Megan A Hahn, Manju Rajeswaran, Sara Maccagnano-Zacher, John Silcox, George E Cragg, Alexander L Efros, and Todd D Krauss. Non-blinking semiconductor nanocrystals. *Nature*, 459(7247): 686–689, 2009.

[94] Florencio García-Santamaría, Yongfen Chen, Javier Vela, Richard D Schaller, Jennifer A Hollingsworth, and Victor I Klimov. Suppressed Auger recombination in giant nanocrystals boosts optical gain performance. *Nano Letters*, 9(10):3482–3488, 2009.

[95] Burak Guzelturk, Yusuf Kelestemur, Kivanc Gungor, Aydan Yeltik, Mehmet Zafer Akgul, Yue Wang, Rui Chen, Cuong Dang, Handong Sun, and Hilmi Volkan Demir. Stable and Low-Threshold Optical Gain in CdSe/CdS Quantum Dots: An All-Colloidal Frequency Up-Converted Laser. *Advanced Materials*, 27(17):2741–2746, 2015.

[96] Chunxing She, Igor Fedin, Dmitriy S Dolzhnikov, Arnaud Demortière, Richard D Schaller, Matthew Pelton, and Dmitri V Talapin. Low-threshold stimulated emission using colloidal quantum wells. *Nano Letters*, 14(5):2772–2777, 2014.

[97] Joel Q Grim, Sotirios Christodoulou, Francesco Di Stasio, Roman Krahne, Roberto Cingolani, Liberato Manna, and Iwan Moreels. Continuous-wave biexciton lasing at room temperature using solution-processed quantum wells. *Nature Nanotechnology*, 9(11):891–895, 2014.

[98] Lucio Claudio Andreani and Alfredo Pasquarello. Accurate theory of excitons in gaas-ga 1- x al x as quantum wells. *Physical Review B*, 42(14):8928, 1990.

[99] J Feldmann, G Peter, EO Göbel, P Dawson, K Moore, C Foxon, and RJ Elliott. Linewidth dependence of radiative exciton lifetimes in quantum wells. *Physical Review Letters*, 59(20):2337, 1987.

[100] B Guilhabert, Caroline Foucher, Anne-Marie Haughey, E Mutlugun, Y Gao, Johannes Herrnsdorf, HD Sun, HV Demir, MD Dawson, and Nicolas Laurand. Nanosecond colloidal quantum dot lasers for sensing. *Optics Express*, 22(6):7308–7319, 2014.

[101] Luke Jonathan McLellan, Benoit Guilhabert, Nicolas Laurand, and Martin D Dawson. CdS x Se 1-x/ZnS semiconductor nanocrystal laser with sub 10kW/cm 2 threshold and 40nJ emission output at 600 nm. *Optics Express*, 24(2):A146–A153, 2016.

[102] Cuong Dang and Arto Nurmikko. Beyond quantum dot LEDs: optical gain and laser action in red, green, and blue colors. *MRS Bulletin*, 38(09):737–742, 2013.

[103] Hans-Jürgen Eisler, Vikram C Sundar, Moungi G Bawendi, Michael Walsh, Henry I Smith, and Victor Klimov. Color-selective semiconductor nanocrystal laser. *Applied Physics Letters*, 80(24):4614–4616, 2002.

[104] C Foucher, B Guilhabert, N Laurand, and MD Dawson. Wavelength-tunable colloidal quantum dot laser on ultra-thin flexible glass. *Applied Physics Letters*, 104(14):141108, 2014.

[105] Rebecca C Somers, Moungi G Bawendi, and Daniel G Nocera. CdSe nanocrystal based chem-/bio-sensors. *Chemical Society Reviews*, 36(4):579–591, 2007.

[106] SM Spillane, TJ Kippenberg, and KJ Vahala. Ultralow-threshold Raman laser using a spherical dielectric microcavity. *Nature*, 415(6872):621–623, 2002.

[107] DK Armani, TJ Kippenberg, SM Spillane, and KJ Vahala. Ultra-high-Q toroid microcavity on a chip. *Nature*, 421(6926):925–928, 2003.

[108] Preston T Snee, Yinthai Chan, Daniel G Nocera, and Moungi G Bawendi. Whispering-Gallery-Mode Lasing from a Semiconductor Nanocrystal/Microsphere Resonator Composite. *Advanced Materials*, 17(9):1131–1136, 2005.

[109] Yinthai Chan, Jonathan S Steckel, Preston T Snee, J Caruge, Justin M Hodgkiss, Daniel G Nocera, Moungi G Bawendi, et al. Blue semiconductor nanocrystal laser. *Applied Physics Letters*, 86(7):3102, 2005.

[110] Bumki Min, Sungjee Kim, Koichi Okamoto, Lan Yang, Axel Scherer, Harry Atwater, and Kerry Vahala. Ultralow threshold on-chip microcavity nanocrystal quantum dot lasers. *Applied Physics Letters*, 89(19):191124, 2006.

[111] Deniz Armani, Bumki Min, Andrea Martin, and Kerry J Vahala. Electrical thermo-optic tuning of ultrahigh-Q microtoroid resonators. *Applied Physics Letters*, 85(22):5439–5441, 2004.

[112] VM Menon, M Luberto, NV Valappil, and S Chatterjee. Lasing from InGaP quantum dots in a spin-coated flexible microcavity. *Optics Express*, 16(24):19535–19540, 2008.

[113] Cuong Dang, Joonhee Lee, Craig Breen, Jonathan S Steckel, Seth Coe-Sullivan, and Arto Nurmikko. Red, green and blue lasing enabled by single-exciton gain in colloidal quantum dot films. *Nature Nanotechnology*, 7(5):335–339, 2012.

[114] Aetna W Wun, Preston T Snee, YinThai Chan, Moungi G Bawendi, and Daniel G Nocera. Non-linear transduction strategies for chemo/biosensing on small length scales. *Journal of Materials Chemistry*, 15(27-28):2697–2706, 2005.

[115] Christos Grivas, Chunyong Li, Peristera Andreakou, Pengfei Wang, Ming Ding, Gilberto Brambilla, Liberato Manna, and Pavlos Lagoudakis. Single-mode tunable laser emission in the single-exciton regime from colloidal nanocrystals. *Nature Communications*, 4, 2013.

[116] Akito Chiba, Hideki Fujiwara, Jun-ichi Hotta, Shigeki Takeuchi, and Keiji Sasaki. Resonant frequency control of a microspherical cavity by temperature adjustment. *Japanese Journal of Applied Physics*, 43(9R):6138, 2004.

[117] Wolf Von Klitzing, Romain Long, Vladimir S Ilchenko, Jean Hare, and Valérie Lefèvre-Seguin. Frequency tuning of the whispering-gallery modes of silica microspheres for cavity quantum electrodynamics and spectroscopy. *Optics Letters*, 26 (3):166–168, 2001.

[118] Matjaz Humar, Miha Ravnik, Stane Pajk, and I Muševič. Electrically tunable liquid crystal optical microresonators. *Nature Photonics*, 3(10):595–600, 2009.

[119] Rico Henze, Tom Seifert, Jonathan Ward, and Oliver Benson. Tuning whispering gallery modes using internal aerostatic pressure. *Optics Letters*, 36(23):4536–4538, 2011.

[120] Mark Fox. *Quantum Optics: An Introduction: An Introduction*. OUP Oxford, 2006.

[121] Chun Hsiung Wang, Tzung Te Chen, Yang Fang Chen, Mei Lin Ho, Chih Wei Lai, and Pi Tai Chou. Recombination dynamics in CdTe/CdSe type-II quantum dots. *Nanotechnology*, 19(11):115702, 2008.

[122] Jian-Bai Xia. Electronic structures of zero-dimensional quantum wells. *Physical Review B*, 40(12):8500, 1989.

[123] AI Ekimov, IA Kudryavtsev, Al L Efros, TV Yazeva, F Hache, MC Schanne-Klein, AV Rodina, D Ricard, and C Flytzanis. Absorption and intensity-dependent photoluminescence measurements on CdSe quantum dots: assignment of the first electronic transitions. *JOSA B*, 10(1):100–107, 1993.

[124] Victor I Klimov. Spectral and dynamical properties of multiexcitons in semiconductor nanocrystals. *Annu. Rev. Phys. Chem.*, 58:635–673, 2007.

[125] Al L Efros. Luminescence polarization of CdSe microcrystals. *Physical Review B*, 46(12):7448, 1992.

[126] Al L Efros and AV Rodina. Band-edge absorption and luminescence of nonspherical nanometer-size crystals. *Physical Review B*, 47(15):10005, 1993.

[127] Maria Chamarro, Catherine Gourdon, Philippe Lavallard, and Alexei I Ekimov. Enhancement of exciton exchange interaction by quantum confinement in CdSe nanocrystals. *Japanese Journal of Applied Physics*, 34(S1):12, 1995.

[128] M Nirmal, DJ Norris, M Kuno, MG Bawendi, Al L Efros, and M Rosen. Observation of the" dark exciton" in CdSe quantum dots. *Physical Review Letters*, 75 (20):3728, 1995.

[129] Al L Efros, M Rosen, M Kuno, M Nirmal, DJ Norris, and M Bawendi. Band-edge exciton in quantum dots of semiconductors with a degenerate valence band: Dark and bright exciton states. *Physical Review B*, 54(7):4843, 1996.

[130] SA Crooker, T Barrick, JA Hollingsworth, and VI Klimov. Multiple temperature regimes of radiative decay in CdSe nanocrystal quantum dots: Intrinsic limits to the dark-exciton lifetime. *Applied Physics Letters*, 82(17):2793–2795, 2003.

[131] S Ithurria, MD Tessier, B Mahler, RPSM Lobo, B Dubertret, and Al L Efros. Colloidal nanoplatelets with two-dimensional electronic structure. *Nature Materials*, 10(12):936–941, 2011.

[132] Louis Biadala, Feng Liu, Mickael D Tessier, Dmitri R Yakovlev, Benoit Dubertret, and Manfred Bayer. Recombination Dynamics of Band Edge Excitons in Quasi-Two-Dimensional CdSe Nanoplatelets. *Nano Letters*, 14(3):1134–1139, 2014.

[133] Jagjit Nanda, Sergei A Ivanov, Marc Achermann, Ilya Bezel, Andrei Piryatinski, and Victor I Klimov. Light amplification in the single-exciton regime using exciton-exciton repulsion in type-ii nanocrystal quantum dots. *The Journal of Physical Chemistry C*, 111(42):15382–15390, 2007.

[134] Victor I Klimov. *Semiconductor and metal nanocrystals: synthesis and electronic and optical properties*. CRC Press, 2003.

[135] Erfan Baghani, Stephen K OLeary, Igor Fedin, Dmitri V Talapin, and Matthew Pelton. Auger-Limited Carrier Recombination and Relaxation in CdSe Colloidal Quantum Wells. *The Journal of Physical Chemistry Letters*, 6(6):1032–1036, 2015.

[136] Peter S Zory. *Quantum well lasers*. Academic Press, 1993.

[137] Mingjie Li, Min Zhi, Hai Zhu, Wen-Ya Wu, Qing-Hua Xu, Mark Hyunpong Jhon, and Yinthai Chan. Ultralow-threshold multiphoton-pumped lasing from colloidal nanoplatelets in solution. *Nature Communications*, 6, 2015.

[138] S. Hooker and C. Webb. *Laser Physics*. Oxford Master Series in Atomic, Optical and Laser Physics. ISBN 9780198506928.

[139] Hiram W Edwards and Robert P Petersen. Reflectivity of evaporated silver films. *Physical Review*, 50(9):871, 1936.

[140] Eugene Hecht. Optics 4th edition. *Optics, 4th Edition, Addison Wesley Longman Inc, 1998*, 1998.

[141] LR Brovelli and U Keller. Simple analytical expressions for the reflectivity and the penetration depth of a Bragg mirror between arbitrary media. *Optics Communications*, 116(4):343–350, 1995.

[142] Bahaa EA Saleh, Malvin Carl Teich, and Bahaa E Saleh. *Fundamentals of photonics*, volume 22. Wiley New York, 1991.

[143] Geoffrey Brooker. *Modern classical optics*, volume 8. Oxford University Press, 2003.

[144] David Hunger, Tilo Steinmetz, Yves Colombe, Christian Deutsch, Theodor W Hänsch, and Jakob Reichel. A fiber Fabry-Perot cavity with high finesse. *New Journal of Physics*, 12(6):065038, 2010.

[145] William T Silfvast. *Laser fundamentals*. Cambridge University Press, 2004.

[146] Ziyun Di, Helene V Jones, Philip R Dolan, Simon M Fairclough, Matthew B Wincott, Johnny Fill, Gareth M Hughes, and Jason M Smith. Controlling the emission from semiconductor quantum dots using ultra-small tunable optical microcavities. *New Journal of Physics*, 14(10):103048, 2012.

[147] Hanno Kaupp, Christian Deutsch, Huan-Cheng Chang, Jakob Reichel, Theodor W Hänsch, and David Hunger. Scaling laws of the cavity enhancement for nitrogen-vacancy centers in diamond. *Physical Review A*, 88(5):053812, 2013.

[148] Gunnar Bjork and Yoshihisa Yamamoto. Analysis of semiconductor microcavity lasers using rate equations. *IEEE Journal of Quantum Electronics*, 27(11):2386–2396, 1991.

[149] John A McGuire, Jin Joo, Jeffrey M Pietryga, Richard D Schaller, and Victor I Klimov. New aspects of carrier multiplication in semiconductor nanocrystals. *Accounts of Chemical Research*, 41(12):1810–1819, 2008.

[150] John A McGuire, Milan Sykora, Jin Joo, Jeffrey M Pietryga, and Victor I Klimov. Apparent versus true carrier multiplication yields in semiconductor nanocrystals. *Nano Letters*, 10(6):2049–2057, 2010.

[151] Aaron G Midgett, Hugh W Hillhouse, Barbara K Hughes, Arthur J Nozik, and Matthew C Beard. Flowing versus static conditions for measuring multiple exciton

generation in PbSe quantum dots. *The Journal of Physical Chemistry C*, 114(41): 17486–17500, 2010.

[152] Concetta Nobile, Luigi Carbone, Angela Fiore, Roberto Cingolani, Liberato Manna, and Roman Krahne. Self-assembly of highly fluorescent semiconductor nanorods into large scale smectic liquid crystal structures by coffee stain evaporation dynamics. *Journal of Physics: Condensed Matter*, 21(26):264013, 2009.

[153] Margherita Zavelani-Rossi, Maria Grazia Lupo, Roman Krahne, Liberato Manna, and Guglielmo Lanzani. Lasing in self-assembled microcavities of CdSe/CdS core/shell colloidal quantum rods. *Nanoscale*, 2(6):931–935, 2010.

[154] Y-S Park, Anton V Malko, Javier Vela, Yongfen Chen, Yagnaseni Ghosh, Florencio García-Santamaría, Jennifer A Hollingsworth, Victor I Klimov, and Han Htoon. Near-unity quantum yields of biexciton emission from CdSe/CdS nanocrystals measured using single-particle spectroscopy. *Physical Review Letters*, 106(18): 187401, 2011.

[155] Robin K Patel, Aurélien AP Trichet, David M Coles, Philip R Dolan, Simon M Fairclough, Marina A Leontiadou, SC Tsang, David J Binks, Eunjoo Jang, Hyosook Jang, et al. Gain Spectroscopy of Solution-Based Semiconductor Nanocrystals in Tunable Optical Microcavities. *Advanced Optical Materials*, 4(2): 285–290, 2016.

[156] Wilfried G. J. H. M. van Sark, Patrick L. T. M. Frederix, Dave J. Van den Heuvel, Hans C. Gerritsen, Ageeth A. Bol, Joost N. J. van Lingen, Celso de Mello Doneg, and Andries Meijerink. Photooxidation and Photobleaching of Single CdSe/ZnS Quantum Dots Probed by Room-Temperature Time-Resolved Spectroscopy. *The Journal of Physical Chemistry B*, 105(35):8281–8284, 2001. doi: 10.1021/jp012018h.

[157] Wilfried G. J. H. M. van Sark, Patrick L. T. M. Frederix, Ageeth A. Bol, Hans C. Gerritsen, and Andries Meijerink. Blueing, Bleaching, and Blinking of Single CdSe/ZnS Quantum Dots. *ChemPhysChem*, 3(10). ISSN 1439-7641.

[158] Virginia W. Manner, Alexey Y. Koposov, Paul Szymanski, Victor I. Klimov, and Milan Sykora. Role of SolventOxygen Ion Pairs in Photooxidation of CdSe Nanocrystal Quantum Dots. *ACS Nano*, 6(3):2371–2377, 2012. doi: 10.1021/nn2046289. PMID: 22381115.

[159] Shuai Gao, Chunfeng Zhang, Yanjun Liu, Huaipeng Su, Lai Wei, Tony Huang, Nicholas Dellas, Shuzhen Shang, Suzanne E Mohney, Jingkang Wang, et al. Lasing from colloidal InP/ZnS quantum dots. *Optics Express*, 19(6):5528–5535, 2011.

[160] AV Malko, AA Mikhailovsky, MA Petruska, JA Hollingsworth, H Htoon, MG Bawendi, and Victor I Klimov. From amplified spontaneous emission to microring lasing using nanocrystal quantum dot solids. *Applied Physics Letters*, 81 (7):1303–1305, 2002.

[161] Wu Lu, Bo Zhong, and Dongge Ma. Amplified spontaneous emission and gain from optically pumped films of dye-doped polymers. *Applied Optics*, 43(26):5074–5078, 2004.

[162] Claudia Gollner, Johannes Ziegler, Loredana Protesescu, Dmitry N Dirin, Rainer T Lechner, Gerhard Fritz-Popovski, Mykhailo Sytnyk, Sergii Yakunin, Stefan Rotter, Amir Abbas Yousefi Amin, et al. Random Lasing with Systematic Threshold Behavior in Films of CdSe/CdS Core/Thick-Shell Colloidal Quantum Dots. *ACS Nano*, 9(10):9792–9801, 2015.

[163] Yujie Chen, Benoit Guilhabert, Johannes Herrnsdorf, Yanfeng Zhang, Allan R Mackintosh, Richard A Pethrick, Erdan Gu, Nicolas Laurand, and Martin D Dawson. Flexible distributed-feedback colloidal quantum dot laser. *Applied Physics Letters*, 99(24):241103, 2011.

[164] B Jensen and A Torabi. Refractive index of hexagonal II–VI compounds CdSe, CdS, and CdSeXS 1–X. *JOSA B*, 3(6):857–863, 1986.

[165] J Schafer, Jessica P Mondia, Rachit Sharma, ZH Lu, AS Susha, AL Rogach, and LJ Wang. Quantum dot microdrop laser. *Nano Letters*, 8(6):1709–1712, 2008.

[166] Manuel Uphoff, Manuel Brekenfeld, Gerhard Rempe, and Stephan Ritter. Frequency splitting of polarization eigenmodes in microscopic Fabry-Perot cavities. *New Journal of Physics*, 17(1):013053, 2015.

[167] Mickael D Tessier, Clementine Javaux, Ivan Maksimovic, Vincent Loriette, and Benoit Dubertret. Spectroscopy of single CdSe nanoplatelets. *ACS Nano*, 6(8): 6751–6758, 2012.

[168] Murat Olutas, Burak Guzelturk, Yusuf Kelestemur, Aydan Yeltik, Savas Delikanli, and Hilmi Volkan Demir. Lateral Size-Dependent Spontaneous and Stimulated Emission Properties in Colloidal CdSe Nanoplatelets. *ACS Nano*, 9(5):5041–5050, 2015.

[169] Chunxing She, Igor Fedin, Dmitriy S Dolzhnikov, Peter D Dahlberg, Gregory S Engel, Richard D Schaller, and Dmitri V Talapin. Red, Yellow, Green, and Blue Amplified Spontaneous Emission and Lasing Using Colloidal CdSe Nanoplatelets. *ACS Nano*, 9(10):9475–9485, 2015.

[170] Benjamin Abecassis, Mickael D Tessier, Patrick Davidson, and Benoit Dubertret. Self-assembly of CdSe nanoplatelets into giant micrometer-scale needles emitting polarized light. *Nano Letters*, 14(2):710–715, 2014.

[171] Burak Guzelturk, Onur Erdem, Murat Olutas, Yusuf Kelestemur, and Hilmi Volkan Demir. Stacking in Colloidal Nanoplatelets: Tuning Excitonic Properties. *ACS Nano*, 8(12):12524–12533, 2014.

[172] Santanu Jana, Trang NT Phan, Cécile Bouet, Mickael D Tessier, Patrick Davidson, Benoit Dubertret, and Benjamin Abécassis. Stacking and Colloidal Stability of CdSe Nanoplatelets. *Langmuir*, 31(38):10532–10539, 2015.